Low-Loss Electron Energy Loss Spectroscopy in a Scanning Transmission Electron Microscope of GaInNAs

by

Mhairi Hope Gass

Thesis submitted for the degree of Doctor of Philosophy (PhD) in accordance with the requirements of the University of Liverpool.

September 2004

Abstract

This thesis presents new methodologies for obtaining the composition and distribution of elements, and determining electronic properties such as the effective electron mass within GaInNAs quantum wells (QWs) using electron energy loss spectroscopy. The aim of this investigation was to explore new techniques in a scanning transmission electron microscope for studying the elemental composition and elemental distribution of dilute nitride semiconductors. To improve the understanding of the dilute nitride materials such as GaInNAs QWs, knowledge of the distribution and composition of nitrogen is very important. However it has not been possible to determine nitrogen distribution using conventional methods. The determination of composition of a GaInNAs QW using techniques such as photoluminescence relies on a reference GaInAs QW, assuming the same In concentration in both wells. The composition of GaInNAs QWs has previously been investigated using energy dispersive X-ray analysis in a scanning transmission electron microscope. However, as nitrogen is a light element the X-rays produced are generally too weak to be detected, and unless it is present in high concentrations there is no possibility of mapping the N signal.

The current work exploits the high energy resolution and fast acquisition times associated with modern low-loss electron energy loss spectroscopy, combined with the spectrum imaging capabilities on a scanning transmission electron microscope. Using this technique, high spatial and energy resolution elemental maps from valence and semi-core states can be produced. Further, by applying the *Kramers-Kronig* transformations, the imaginary part of the dielectric function can be

obtained, which represents the absorption of the material and does not exhibit the bulk plasmon. As the bulk plasmon is the major feature in the low-loss it obscures many of the weaker transitions. By analysing the imaginary part of the dielectric function instead of the loss spectrum the quantification of the semi-core states is improved. This technique produces high spatial resolution maps that for certain elements are quantifiable.

The effect of composition on plasmon energy has been investigated and it is shown that through the effective number of electrons obtained from the *Kramers-Kronig* transformations and the plasmon energy, the effective electron mass can be determined. High spatial resolution maps can be produced, and the change in effective electron mass can be directly compared with the composition. By combining the techniques of elemental composition mapping and effective electron mass mapping, a greater understanding of the distribution of nitrogen on the electronic properties has been achieved.

This thesis describes an account of the research that was undertaken with the supervision of Dr T.J. Bullough and Prof. P.R. Chalker in the Department of Engineering, University of Liverpool between the period of October 2001 and September 2004. The research is original and has not been submitted for degree from this or any university. Where necessary, the research and results of other authors have been included and due acknowledgement has been made. Lists of references are presented at the end of each chapter.

Mhairi Hope Gass.

Publications

Some of the results and discussions of this research presented in chapters 4 and 5 have been published in the following scientific literature.

Journal

1. M.H. Gass, A.J. Papworth, T.J. Bullough, and P.R. Chalker. (2004) *Elemental mapping using the Ga 3d and In 4d transitions in the ε2 absorption spectra derived from EELS,* Ultramicroscopy, **101**, 257

2. AM Sánchez, M Gass, AJ Papworth, PJ Goodhew and P Ruterana (2004) Nanoscale *EELS analysis of InGaN/GaN heterostructure,*. Phys. Review B, **70**, 035325

3. S Davies, TS Huang, MH Gass, AJ Papworth, TB Joyce and PR Chalker, (2004) *Fabrication of epitaxial III - nitride cantilevers on silicon (111) substrates, Journal of electronic Materials* (accepted)

4. PR Chalker, TJ Bullough, M Gass, TB Joyce and S Thomas (2004) *The microstructural influence of nitrogen incorporation in dilute nitride semiconductors*, J. Condensed Matt. Phys., **16**, S3161

5. M.H. Gass, A.J. Papworth, T.B. Joyce, T.J. Bullough, P.R. Chalker, (2004) *Measurement of the effective electron mass in GaInNAs by energy-loss spectroscopy*, Applied Physics Letters, **84**, 1453

6. S Davies, TS Huang, MH Gass, AJ Papworth, TB Joyce and PR Chalker, (2004) *Fabrication of GaN cantilevers on silicon substrates for microelectromechanical devices*, Applied Physics Letters, **84**, 2566

Conference

7. M.H. Gass, A.M. Sanchez, A.J. Papworth, T.J. Bullough and P.R. Chalker, (2004) *High Spatial Resolution Mapping Of The Effective Mass In GaInNAs*, Microscopy and Microanalysis 2004

8. M.H. Gass, A.M. Sanchez, A.J. Papworth, T.J. Bullough and P.R. Chalker, (2004) *Quantitative Elemental Mapping Using Valence-Band Transitions In* ε_2*, Using Electron Energy Loss Spectroscopy*, Microscopy and Microanalysis 2004

9. A.M. Sánchez, M. Gass, A.J. Papworth and P.J. Goodhew, (2004) *EELS analysis of InGaN/GaN heterostructures using the Ga 3d transitions in Epsilon 2*, Microscopy and Microanalysis 2004

10. A.M. Sánchez, M. Gass, A.J. Papworth and P.J. Goodhew, (2004) *Defect analysis in InGaN/GaN heterostructures by combined EDX and CTEM studies*, Microscopy and Microanalysis 2004

11. MH Gass, TJ Bullough, AJ Papworth, S Thomas, TB Joyce, PR Chalker, S Mazzucato, C Hepburn and N Balkan, (2003) *Compositional non-uniformity in CBE grown GaInNAs/GaAs quantum wells,* MSM 2003, IoP Conference, 180, 225

12. AM Sanchez, MH Gass, AJ Papworth, P. Ruterana, HK Cho and PJ Goodhew, (2003) *Indium fluctuation analysis inside the InGaN quantum wells by Scanning Transmission Electron Microscopy*, EMAG 2003, IoP Conference, 179, 131

Acknowledgements

I would like to take this opportunity to thank my supervisors Paul Chalker and Tim Bullough who have guided me throughout this work. Also Tim Joyce from the University of Liverpool, Chantel Fontaine from LAAS-CNRS and Virginie Drouot from Bookham Technology Inc. for growing the samples investigated. I am especially grateful for the time and patience given by Adam Papworth who trained me on the scanning transmission electron microscope.

I would also like to thank my friends and family, especially Youcef, who has supported me all the way through. Finally I would like to acknowledge the financial support provided by EPSRC.

Contents

Page

Nomenclature……………………………………………………………………xii

1 Introduction to GaInNAs and the electronic properties of III-V semiconductors ………………………………………………………1

1.1 Introduction……………………………………………………………..2

1.2 Semiconductor Laser diodes…………………………………………....3

1.3 GaInNAs…………………………………………………………….….9

1.3.1 The development of GaInNAs……………………………9

1.3.2 Growth of GaInNAs and Thermal Annealing……………13

1.4 Band structure and electronic properties of semiconductors……..14

1.4.1 Electronic band structure of GaAs………………………..14

1.4.2 Band gap of III-V semiconductor materials………………18

1.4.3 Photoluminescence studies of GaInNAs materials………..21

1.4.4 Effective mass (m_e*)……………………………………22

1.4.5 *Kramers-Kronig* transformation…………………………..23

1.5 TEM studies of GaInNAs……………………………………………....24

1.5.1 Transmission electron microscopy studies of GaInNAs and related materials……………………………………………24

1.5.2 Electron energy loss spectroscopy of Ga(In)(N)As and GaN……………………………………………25

References (chapter 1)…………………………………………………………30

2 Electron-Sample interactions……………………………………………...35

2.1 Elastic Scattering…………………………………………………………36

2.1.1 Introduction..36

2.1.2 Differential cross-section for elastic scattering..............38

2.2 Inelastic scattering...38

2.2.1 Differential cross section for inelastic scattering...........39

2.2.2 Dielectric formulation..41

2.3 The Energy Loss Spectrum..43

2.4 Outer-Shell Excitation...45

2.4.1 Volume plasmons..45

2.4.1.1 The *Drude-Lorentz* theory............................45

2.4.1.2 Shift of plasmon peaks.................................48

2.4.2 Surface plasmons...49

2.5 Inner-shell excitations...50

2.6 Single scattering of electrons..51

References (chapter 2)...54

3 Experimental Techniques..55

3.1 CBE and MBE growth of samples....................................56

3.2 Sample preparation for transmission electron microscopy...........58

3.2.1 Mechanical grinding..58

3.2.2 Dual Beam FIB..59

3.3 Scanning Transmission Electron Microscopy (STEM)..............63

3.4 Electron Energy Loss Spectroscopy (EELS).........................65

3.4.1 Introduction to core-loss analysis............................67

3.4.2 Core-loss analysis in the STEM...............................68

3.4.3 Introduction to low-loss analysis.............................69

3.4.4 Low-loss analysis in the STEM...............................70

3.4.4.1 Aligning the spectrum and removal of plural scattering...70

3.4.4.2 Determination of the plasmon energy...............72

3.4.5 *Kramers-Kronig* Analysis......................................74

3.4.5.1 Epsilon 1 (ε_1)..75

3.4.5.2 Epsilon 2 (ε_2)..76

3.4.5.3 Effective number of electrons.........................78

3.4.5.4 Absolute sample thickness............................79

3.4.5.5 Optical absorption coefficient.........................80

3.4.5.6 Effective mass (m_e^*)..................................80

3.5 Energy dispersive X-ray (EDX) analysis.............................81

3.6 Photoluminescence..82

References (chapter 3)..84

4 **Results: Elemental quantification using semi-core states**...............85

4.1 Quantum well and full laser structure specimens analysed in this study...86

4.2 Factors affecting the energy loss spectrum...........................88

4.2.1 Thickness effects on the energy loss spectrum..............88

4.2.2 Carbon contamination during energy loss acquisition......91

4.3 Quantification of sample composition using semi-core states in energy loss spectra..92

4.3.1 Quantification of the composition of group III elements in GaInNAs...92

4.3.2 Quantification of the composition of the group III elements in InAs QDs……104
4.3.3 Quantification of the composition of the group III elements in GaN/AlGaN……105
4.3.4 Quantification of the composition of the group V elements in GaInNAs……106
4.4 Discussion……110
References (chapter 4)……111

5. Results: Plasmon energy and the effective electron mass…… 112
5.1 Determination of the plasmon energy……115
5.1.1 Centre of plasmon peak……115
5.1.1.1 GaIn(N)As……117
5.1.1.2 InAs QDs……121
5.1.1.3 AlGaN/GaN……122
5.1.2 Calculation of the plasmon energy from the condition Epsilon 1 equals zero……124
5.1.3 Free electron calculations……127
5.2 Effective electron mass mapping……130
5.2.1 GaInNAs QWs……130
5.2.2 InAs QDs……132
5.2.3 AlGaN/GaN……134
5.2.4 Modification of m_e*……135
5.3 Discussion……138
References (chapter 5)……140

6. Conclusions……143

6.1 Conclusions……144

6.2 Suggestions for future work……147

References (chapter 6)……149

Appendix A……151

Appendix B……152

Nomenclature

θ	scattering angle
γ	relativistic factor
a_0	Bohr radius
b	impact parameter
CB	conduction band
CBE	chemical beam epitaxy
DMHy	dimethylhydrazine
DOS	density of states
E	energy
EDR	energy derivative reflectance
EDX	energy dispersive X-ray
EELS	electron energy loss spectroscopy
EFTEM	energy filtered TEM
ELNES	energy loss near edge structure
ELS	energy loss spectroscopy
ER	electroreflectance
f(q)	complex scattering angle
FEG	field emission gun
FIB	Focused ion beam
$f_n(q)$ / *GOS*	generalised oscillator strength
$f_x(q)$	X-ray atomic scattering factor
GS-MB	gas source molecular beam epitaxy
HREELS	high-resolution electron energy loss spectroscopy
$\mathbf{k_0}$	wave vector before scattering
$\mathbf{k_1}$	wave vector after scattering
KK	*Kramers-Kronig*
LDA	local-density approximation
MBE	molecular beam epitaxy

m_e*	effective electron mass
MOCVD	metalorganic chemical vapour deposition
MOVPE	metal organic vapour phase epitaxy
PEELS	parallel electron energy loss spectroscopy
PL	photoluminescence
q	scattering vector
QD	quantum dot
QW	quantum well
REELS	reflected electron energy loss spectroscopy
RT	room temperature
STEM	scanning transmission electron microscopy
T_0	characteristic temperature
TEGa	triethylgallium
TEM	transmission electron microscopy
TGA	tertiarybutylarsine
TMGa	trimethylgallium
TMIn	trimethylindium
v	velocity of incident electron
VB	valence band
Z	atomic number
ZLP	zero loss peak
$\varepsilon(q,\omega)$	dielectric response function
θ_E	characteristic angle
ψ_0	wave function (initial state)
ψ_n	wave function (final state)

Chapter 1

Introduction to GaInNAs and the electronic properties of III-V semiconductors

Section		Page
1.1	Introduction	2
1.2	Semiconductor Laser diodes	3
1.3	GaInNAs	9
1.4	Band structure and electronic properties of semiconductors	14
1.5	TEM studies of GaInNAs	24

1 Introduction to GaInNAs and the electronic properties of III-V semiconductors

1.1 Introduction

The laser diodes currently used in fibre optic communications generally consist of a GaInPAs based device grown on InP substrates. These devices are designed to operate at emission wavelengths of 1.3μm or 1.55μm in order to minimise transmission loss in the optical fibres[i]. Unfortunately, these laser diodes have poor temperature characteristics (T_0) and require thermoelectric coolers to keep them below 60K to operate efficiently. This low T_0 is mainly caused by poor electron confinement due to a small band gap discontinuity in the conduction band[1]. However, laser diodes based on alternative materials such as GaInAs grown on GaAs substrates have a T_0 of over 150K[2], but can only emit at wavelengths of up to 0.98μm. It is clearly desirable to develop a long wavelength (1.3μm - 1.55μm) laser diode that can operate at ambient temperatures, and this is a primary motive for the development of the GaInNAs alloy system.

The quaternary semiconductor alloy GaInNAs was first proposed and demonstrated as a material having a band gap energy suitable for long-wavelength emitting diodes (1.3μm - 1.55μm) by *Kondow et al*[3] in 1995. Since then it has been developed by many groups internationally, using several techniques such as molecular beam epitaxy (MBE)[4,5] gas source MBE[6], plasma-assisted MBE[7], metalorganic vapour

[i] These wavelengths are measured in a vacuum, the wavelengths attained within the glass fibre will be shorter.

phase epitaxy (MOVPE) [8] and chemical beam epitaxy (CBE) [9,10]. Other potential device applications for the GaInNAs alloy include photodetectors[11], solar cells[12,13] and transistors[14].

This literature review examines the development of GaInNAs growth techniques followed by a discussion of previous work investigating the electronic structure, band gap and effective mass of III-V semiconductors, from materials such as GaAs through to the quaternary GaInNAs alloy. The literature covering scanning transmission electron microscopy (STEM) studies of GaInNAs microstructure, energy dispersive X-ray (EDX) analysis and electron energy loss spectroscopy (EELS) relevant to this study is discussed. The concept of the *Kramers-Kronig* transformations will also be introduced. The technique of photoluminescence spectroscopy will be covered briefly, as although it is an experimental technique only indirectly utilised during this research, it is an important characterisation technique for opto-electronic materials, and was used to determine the band gap of the materials studied.

1.2 Semiconductor Laser diodes

Producing highly directional beams of light in the infrared (IR) region of the spectrum, semiconductor lasers are one of the most important light sources for optical-fibre communication. They are small and easily modulated at high frequencies by adjusting the biasing current. Generally, lasing semiconductors have direct band gaps, as for electrons and holes to recombine in indirect band gaps, it is necessary that a phonon with the correct momentum is also available, making the

emission of a photon much less likely. Within the laser heterostructure, it is desirable that the lattices between the different semiconductor materials are closely matched so as to avoid interface traps. It is therefore necessary to know the lattice mismatch between the semiconductor materials that will share an interface. Other characteristics that determine the lasing ability of a heterostructure are the operating temperature, threshold current of emission and the emission sensitivity to electrical stimulation.

The use of GaInNAs as the active layer in a laser diode is feasible as it has a direct band gap which, on altering the In and N concentrations can be tailored to emit over a range of high frequencies. GaInNAs can also be lattice matched to GaAs. Further, it can be operated at ambient temperatures, eliminating the need for thermoelectric coolers.

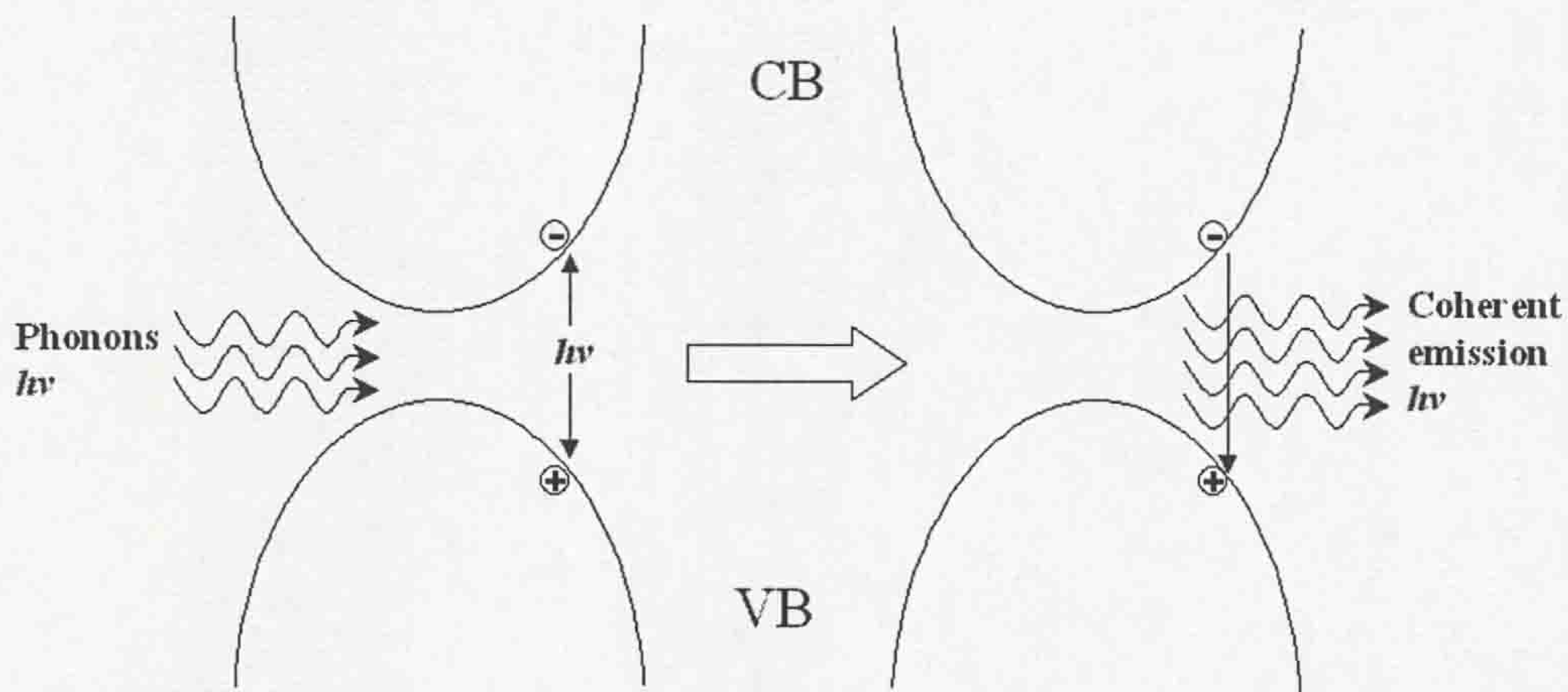

Figure 1-1 Stimulated emission in a semiconductor laser (direct band gap).

As for a light emitting diode (LED), the semiconductor laser diode is a forward bias p-n junction. However, unlike the LED, where the electrons and holes recombine

radiatively via the spontaneous emission process emitting incoherent phonons, the laser structure is designed so that the emission process only occurs by the stimulated emission process. The stimulated emission process shown in Figure 1-1 requires the presence of a photon of exact energy hv for electron hole recombination. On recombination, coherent photons are emitted with the same energy and wave vector (in phase) as the incident photons. These coherent photons are confined within the laser structure by an optical cavity, which can guide the photons; they will in turn stimulate further electron hole recombination resulting in more photons that are coherent. This causes a cascade effect and the photon density increases. The optical cavity is achieved primarily by using a highly polished surface, which produces a mirror effect causing internal reflection. A typical simple heterojunction semiconductor laser is shown in Figure 1-2.

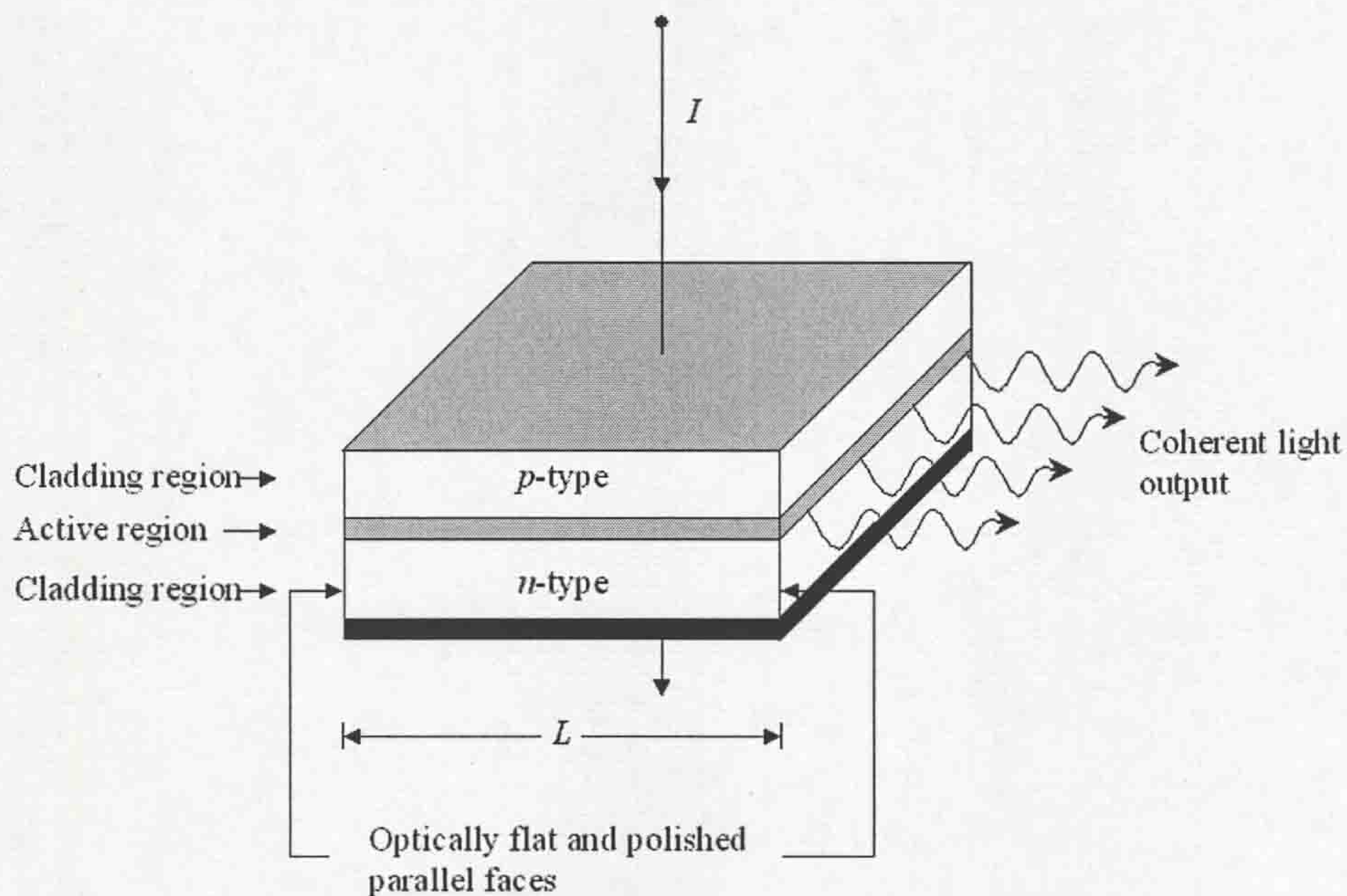

Figure 1-2 A typical simple heterojunction semiconductor laser.

There are several designs of laser diode, each with its own advantages and disadvantages. The simplest design is the edge-emitting laser shown in Figure 1-3. As the name suggests, the laser emits light from the edge of the chip. It is the simplest laser diode to create as it can be produced by cleaving the face of an as-grown structure.

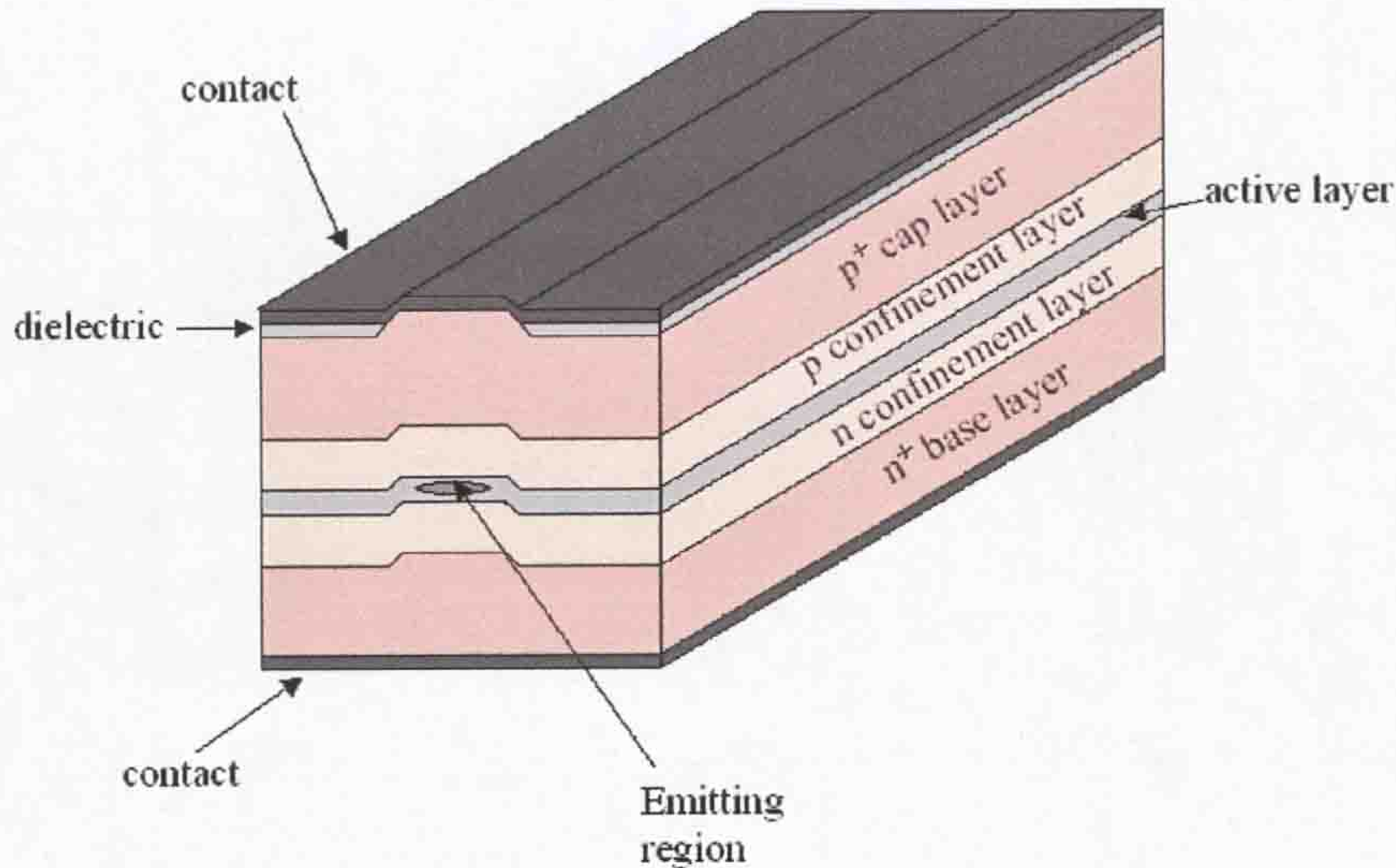

Figure 1-3 Typical design of an edge-emitting semiconductor laser diode.

A vertical cavity surface-emitting laser (VCSEL), shown in Figure 1-4 emits light from the top surface. This allows large quantities of chips to be produced and tested on a single wafer, which is not possible for the edge-emitting laser. The VCSEL uses a circular contact electrode, which confines the light emission. The use of a circular electrode in conjunction with reflective surfaces, so that the photons experience multiple passes, allows the cavity length of a VCSEL to be very short (1-3 wavelengths of the emitted light). Most VCSEL devices employ quantum well structures within the cavity and the use of multiple quantum wells increases the power obtained. A further advantage that VCSELs have over the edge-emitting

laser diode is the ease of coupling them to optical fibres, making them very desirable for the telecommunications industry.

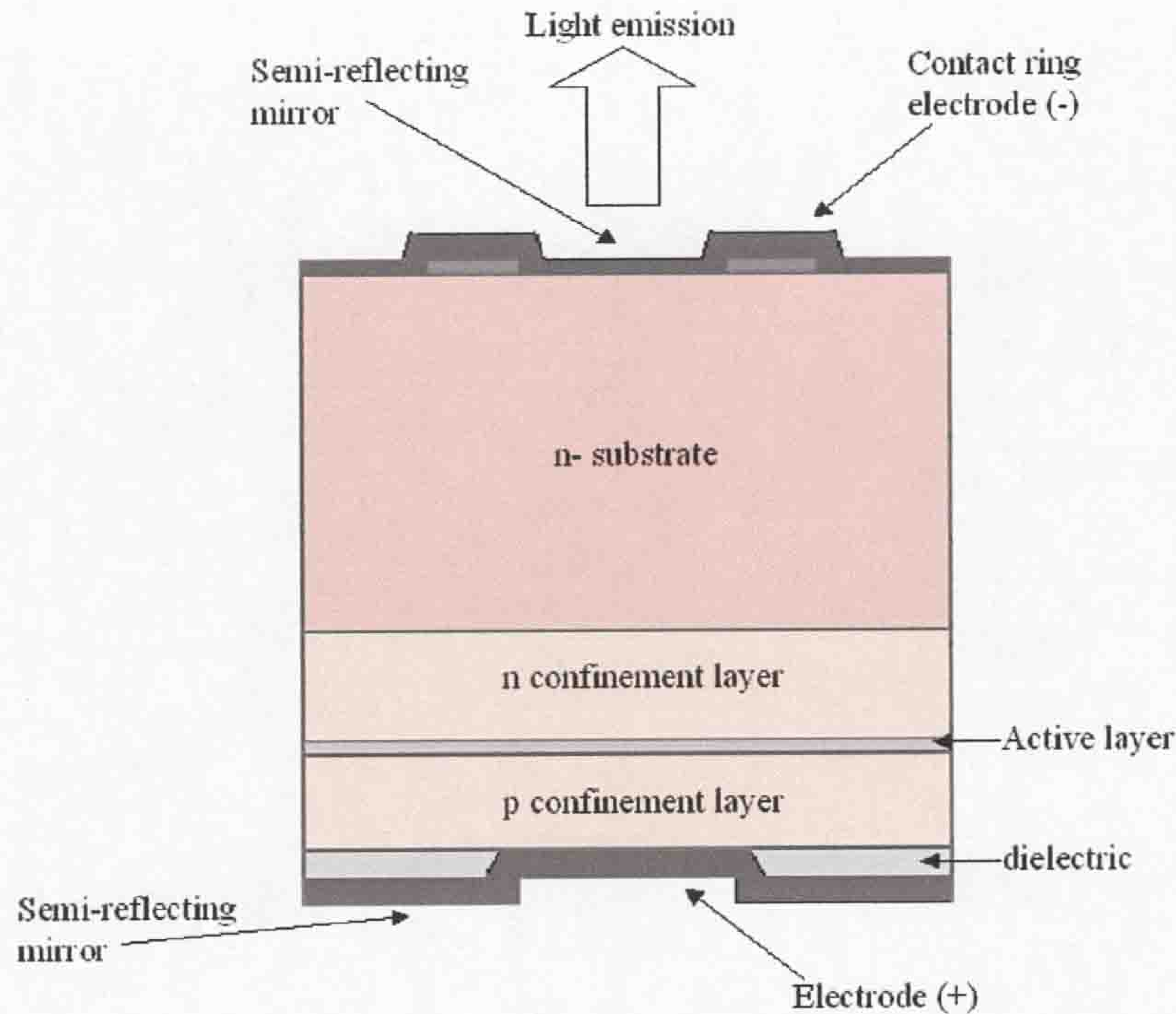

Figure 1-4 A typical vertical cavity surface emitting laser (VCSEL).

The driving force to find semiconductor materials with emission wavelengths at 1.3μm and 1.55μm lies with the fibre optic cables that carry the signal transmitted from the laser diode. The fibre optic cables are generally made from a variety of glasses, which have very high chemical stability. They consist of an inner core with a refractive index *n*, and a cladding layer on the outside with a lower refractive index. The cladding layer confines the optical waves that propagate through the core with minimal loss. However, to achieve the minimal loss the wavelength of the signal must be carefully chosen. Figure 1-5 shows the typical loss for different photon wavelengths in silica fibres. The fibre attenuation gradually decreases with increasing wavelength, following the Raleigh scattering, up to a value of 1.55μm.

On the attenuation curve, there is an intense peak at 1.4μm; this is due to the second harmonic vibration of the H and O atoms from impurity water molecules in the fibres, and results in the strong absorption of light. There are further weaker harmonics from the O-H vibration at lower wavelengths, indicated in Figure 1-5. At wavelengths above 1.55μm, there is a dramatic increase in the fibre attenuation due to vibrations between the Si and O atoms in the glassy molecules. This results in the loss of light at these wavelengths to be above an acceptable limit.

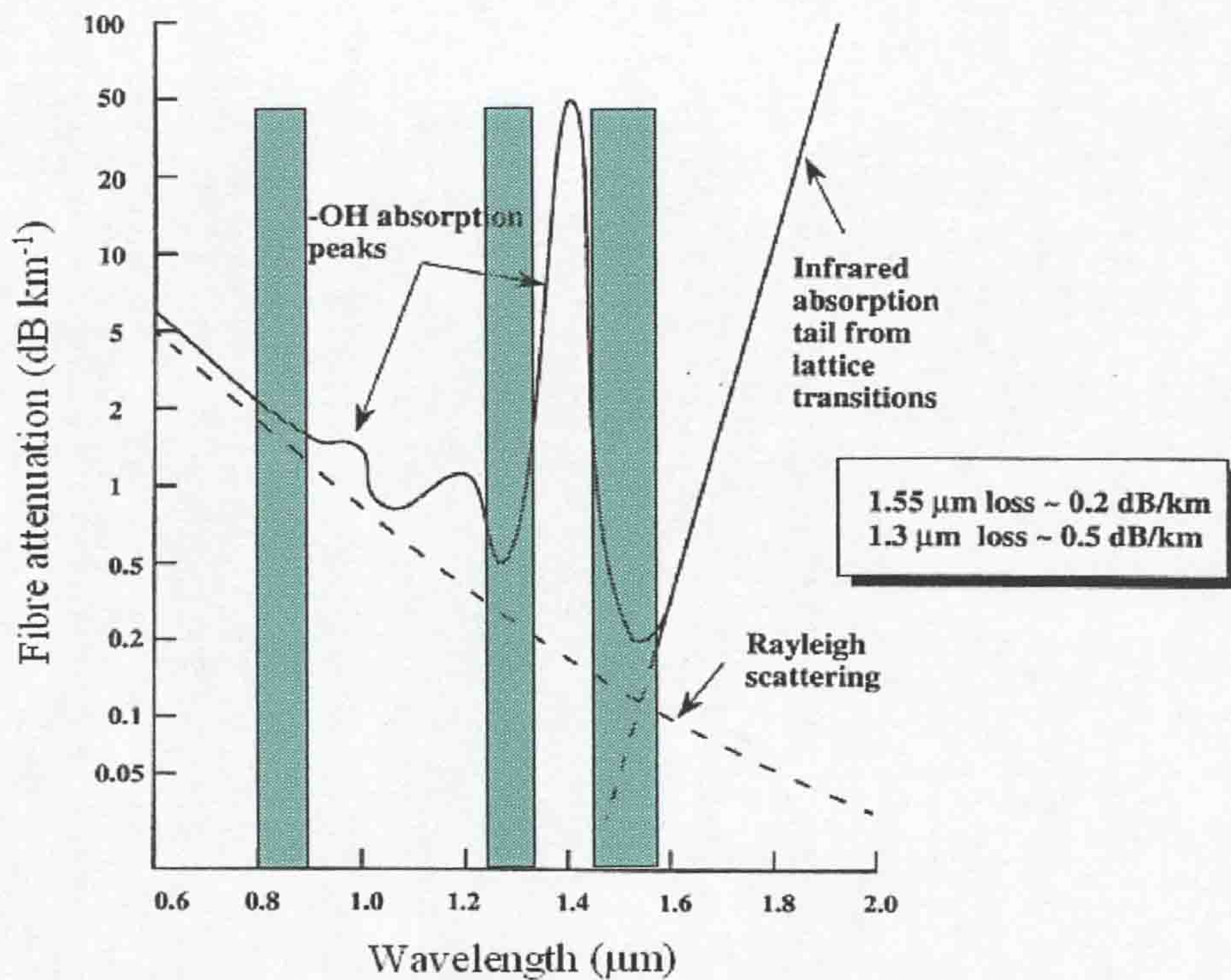

Figure 1-5 Attenuation in silica optical fibres as a function of wavelength. Taken from *Singh*[15].

To achieve the minimum transmission loss possible through a fibre optic cable, it follows from the above discussion that the light must be at a wavelength where there is low fibre attenuation. There are three transmission windows, indicated in green on Figure 1-5, and the sources (e.g. laser diodes) are designed to emit at these wavelengths. The *first transmission window* is between 0.8μm – 0.9μm and

although attenuation is high, many sources are produced to emit in this window, as the cost of production is lower due to easier manufacturing processes. The *second* and *third transmission windows* are at 1.26 μm – 1.36μm and 1.43 μm – 1.58μm respectively, and although the *third transmission window* displays the lowest attenuation at 1.55μm, the *second transmission window* is coupled with zero material dispersion and is therefore very attractive as a transmission window. The interest in GaInNAs as an active region in a laser diode based on GaAs, transmitting at 1.3 or 1.55μm is driven by the low attenuation that could be achieved at these wavelengths and the capacity to transmit at ambient temperature. Interest is also driven by the manufacturing advantages of the well-established GaAs technology in comparison with the InP technology currently used with the GaInAsP active regions emitting at similar wavelengths.

1.3 GaInNAs

1.3.1 The development of GaInNAs

Previously, laser diodes developed for ambient temperature operation have been developed which employed GaInAs quantum wells (QWs) on a GaAs substrate. By altering the indium concentration, the band-gap of and hence wavelength from the quantum well could be changed[16], and lasing wavelengths approaching 1μm were achieved with excellent electrical and optical properties[2]. However, to minimise both fibre attenuation and pulse dispersion, ideally data must be transmitted at 1.3μm or 1.55μm. To achieve wavelengths approaching 1.3μm, one approach is to build in further quantum confinement. This can be realized by exploiting the use of quantum dots (QDs). GaInAs QDs embedded within a laser structure have shown

good electrical characteristics[17], nevertheless the control of QD size and distribution leads to a more complicated fabrication processes, not to mention the introduction of materials problems such as localised strain concentrations or rough overgrowth. To attain the higher emission wavelengths without the complication of QD growth an alternative approach is to incorporate additional elements into the system to modify the material band gap. *Kondow et al*[18] recognised that the introduction of a small amount of N to GaInAs would have dramatic effects on the material's properties.

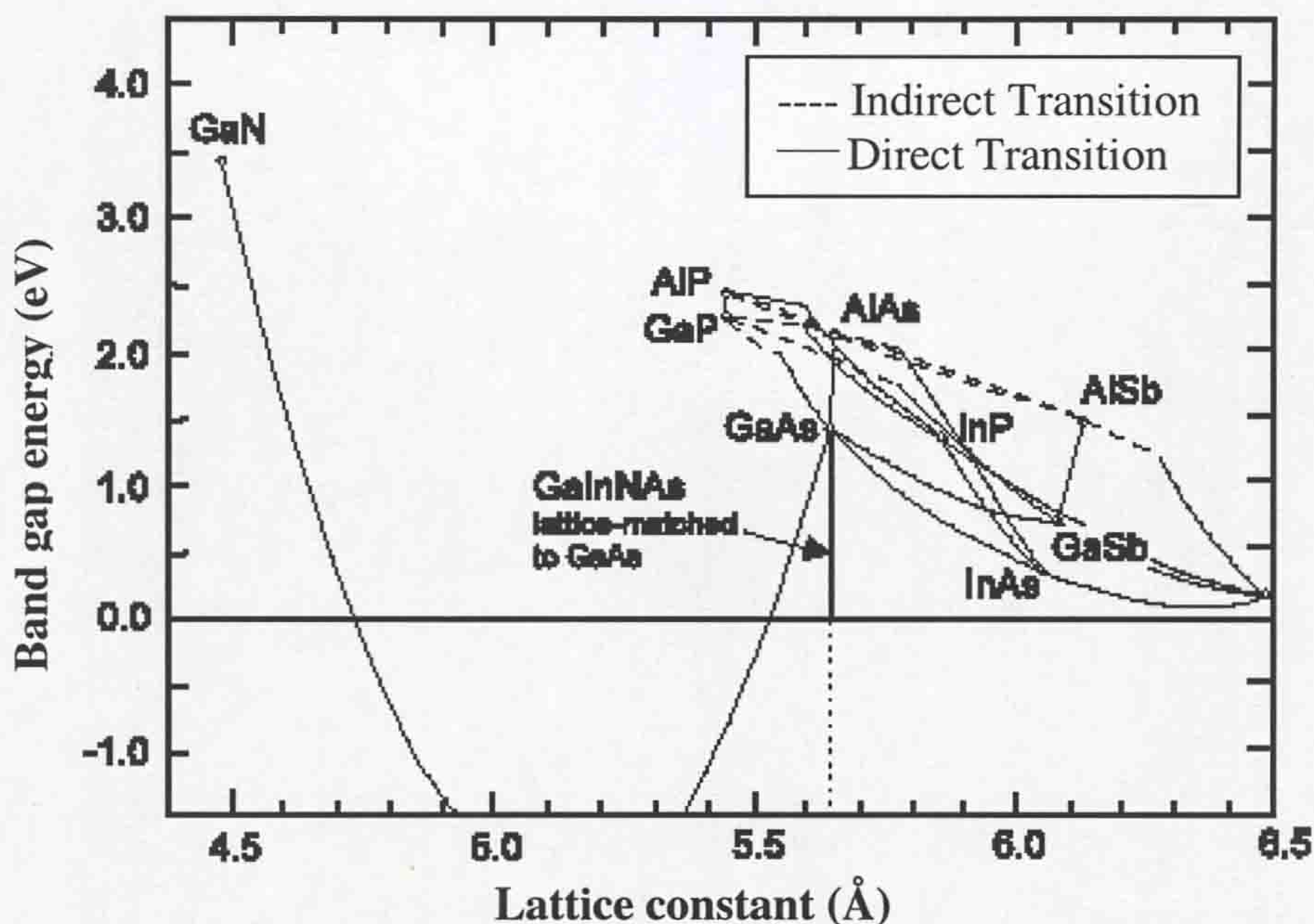

Figure 1-6. The relationship between the lattice constant and band gap energy in III-V alloy semiconductors. Taken from *Kondow et al*[3].

Figure 1-6 demonstrates the relationship between the lattice constant and band gap energy in III-V alloy semiconductors. It can be seen that the introduction of In to GaAs reduces the band gap, and increases the lattice constant. However, the addition of N to GaAs reduces the lattice constant as well as reducing the band gap, therefore allowing the composition of the $Ga_{1-x}In_xN_yAs_{1-y}$ quaternary alloy to be controlled, and remain near-lattice matched to GaAs. It has been demonstrated that

with a low N content, GaInNAs can be lattice matched to both GaAs and InP with its band gap anywhere in the region of 0.6eV to 1.42eV. These GaInNAs materials are part of a group of III-V semiconductors known as *dilute nitrides*. GaInAs and GaNAs are direct band gap materials; GaInNAs is also a direct transition type compound, which is a pre-requisite for an efficient light emitting material.

The band line-up of a GaInNAs QW with the cladding material is an important factor in determining carrier distributions. It is essential that both electrons and holes are confined within the QW layer. There are three types of band line-up as shown in Figure 1-7a. Type I shows a higher valence but lower conduction band for material 1 (QW) compared to material 2 (cladding), allowing material 1 to be the preferred state for both the electrons and holes. Types II and III both allow carrier overflow and are undesirable for QW lasers. In Figure 1-7b a schematic of a QW is illustrated, clad by a larger band gap material; it demonstrates a type I band line-up, which is required for a QW laser allowing the electrons and holes to be confined in the QW.

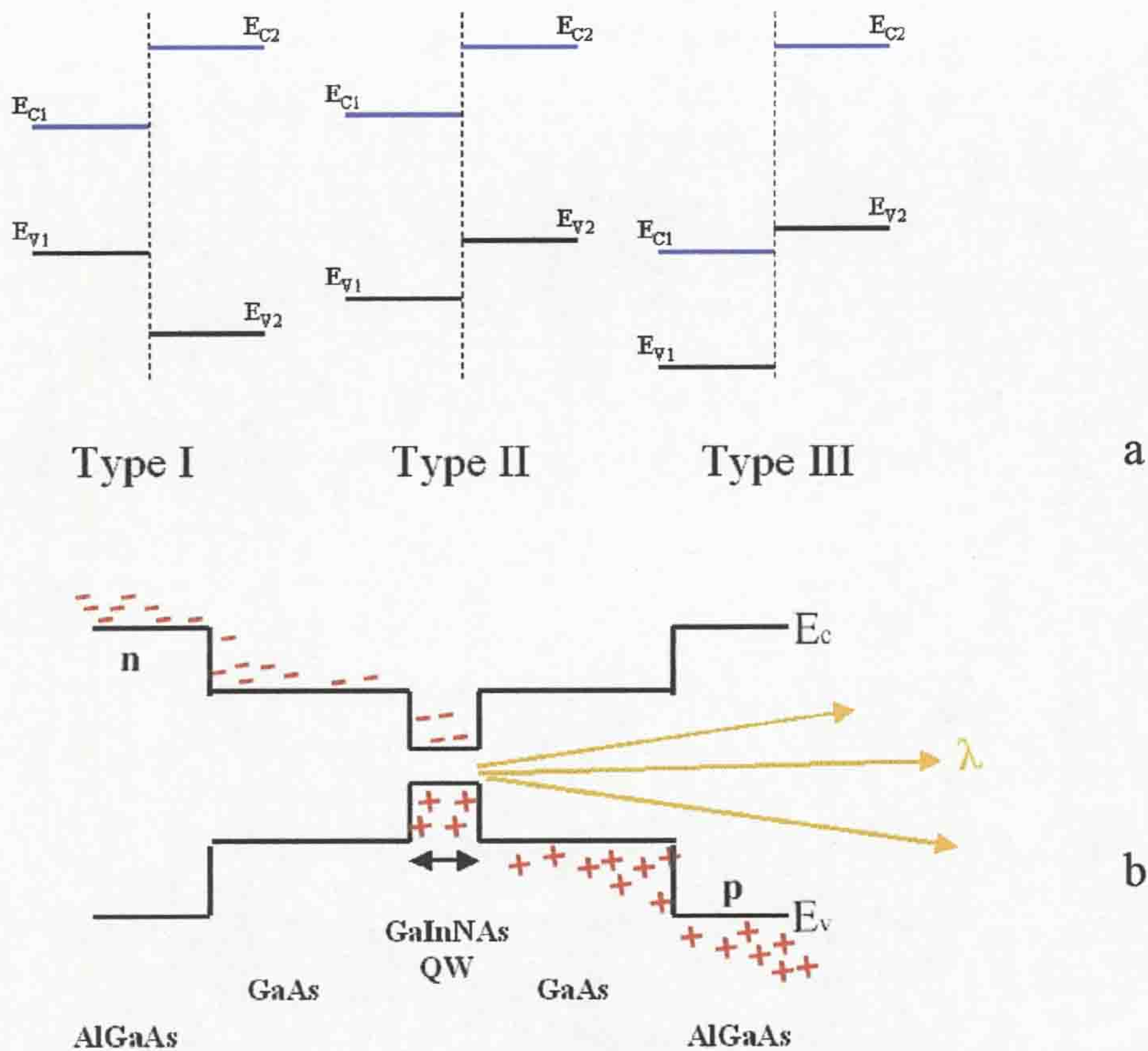

Figure 1-7. a) Demonstrates the three types of band line-up possible; for QW laser design, type I is necessary so that electrons and holes can be confined within the QW as illustrated in b).

In Figure 1-8, the band line-up and strain are shown as In and N are added to GaAs. The right hand side of the diagram illustrates that as In is added to GaAs, the compressive strain increases, increasing the valence band and lowering the conduction band. However, the tensile strain increases as N, with a smaller ionic radius, is added to GaAs (left hand side of figure), resulting in the lowering of both the valence and conduction band energies. The diagram demonstrates that a compressively strained GaInNAs QW is desirable with a band gap of BE as it allows for the type I band line-up when GaAs cladding is used.

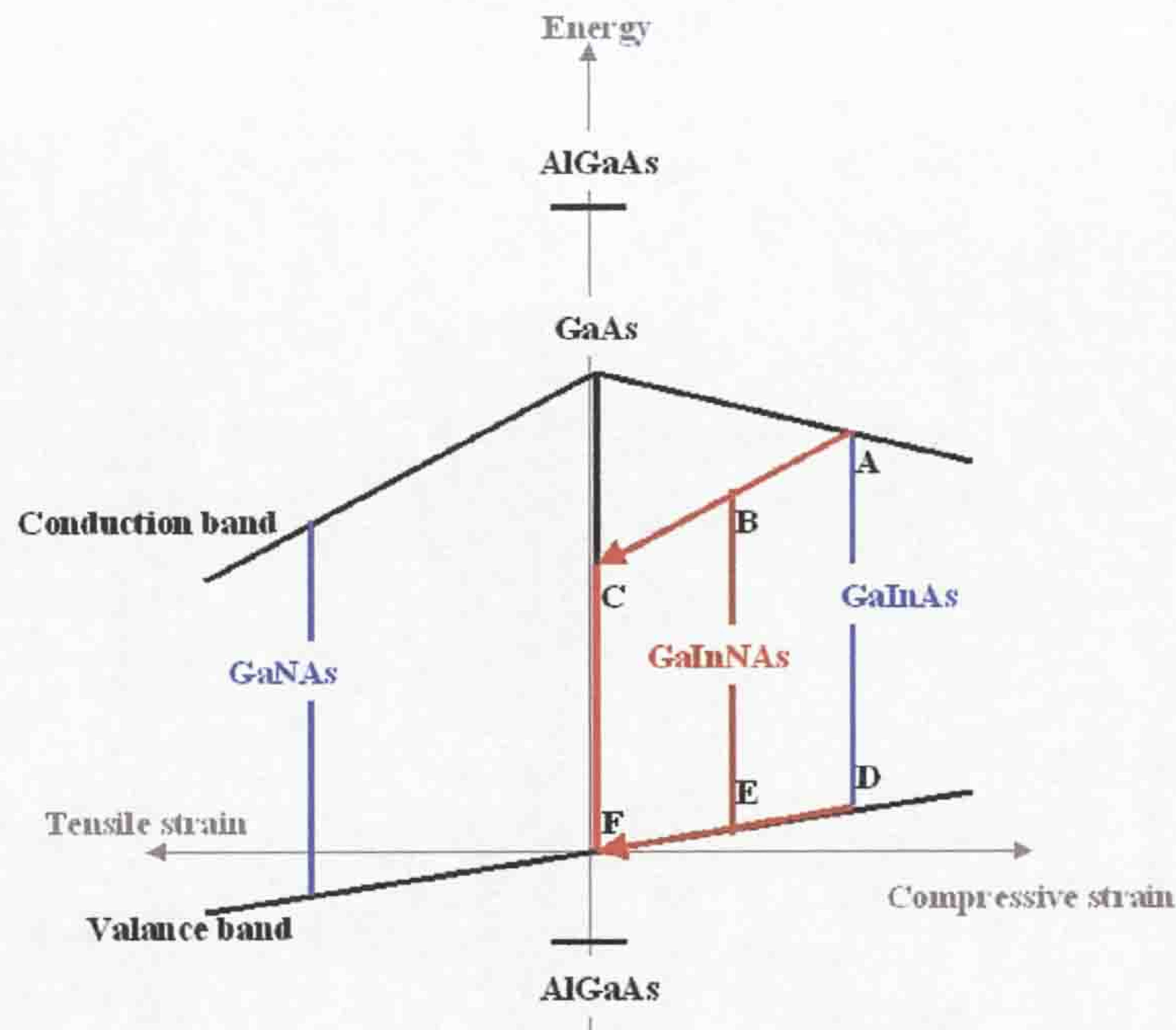

Figure 1-8. A schematic diagram of the band line-up for GaInAs, GaNAs and GaInNAs with reference to GaAs. Taken from *Kondow et al*[3].

1.3.2 Growth of GaInNAs and Thermal Annealing

Kondow et al[1,3] successfully grew the first GaInNAs material using gas-source molecular beam epitaxy (GS-MBE); metallic Ga, metallic In, arsine gas and nitrogen gas were used as precursors, and growth temperatures between 350 and 550 °C were employed. A 7nm $Ga_{0.7}In_{0.3}N_{0.004}As_{0.996}$ single QW was grown on a GaAs substrate, which achieved a photoluminescence peak of 1.17µm at room temperature, they recognised that by increasing the N content of the active GaInNAs layer, emission wavelengths of 1.3µm at RT could be achieved. Various research groups have since used a range of different and successful growth techniques, for example:

- Metal organic vapour phase epitaxy (MOVPE)[19] and Metalorganic chemical vapour deposition (MOCVD) using trimethylgallium (TMGa), trimethylindium (TMIn), dimethylhydrazine (DMHy) and arsine sources,
- Molecular beam epitaxy (MBE)[20,4] where metal Ga, metal In and various As and N sources were used and,
- Chemical beam epitaxy (CBE)[9,10] using triethylgallium (TEGa), TMIn, AsH_3 and N_2 gas plasma sources.

The luminescent efficiency of the active layer of as-grown GaInNAs can often be poor, with the material exhibiting elemental segregation, and it has been reported that a post-growth thermal anneal can improve the luminescence (discussed further in section 1.4.3)[9]. Different temperature regimes have been used for the thermal anneals by various groups. As an example, *Volovik et al*[20] performed anneals at 700ºC in an As_4 environment for 30 minutes, whilst *Kageyama et al*[9] investigated a rapid anneal of 30 seconds between 600 and 900 ºC under a N_2 flux. Both annealing regimes resulted in a blue shift (reduction in wavelength) and an increase in intensity of the photoluminescence (PL) peak, which has been attributed to various affects associated with In-Ga interdiffusion.

1.4 Band structure and electronic properties of semiconductors

1.4.1 Electronic band structure of GaAs

To enable a discussion of the electronic transitions in III-V semiconductor materials, the electronic band structure must first be reviewed; this will cover the different interband transitions that occur around the band gap region to higher energy

interband transitions from semi-core electrons situated below the valence band. The study of optical transitions between the valence and conduction bands in semiconductors dates back to the 1950s[21], and in 1966, *Phillips*[22] detailed the electronic structure of many III-V compounds in the energy range below 7eV. Early experimental work for absorption and reflection spectroscopy of interband transitions for III-V semiconductors above 7eV used gas-discharge sources such as He, Ne and Ar. These sources produced line radiation from electronic transitions between different energy levels within an atom, molecule or ion. The width or sharpness of these lines was typically in the region of 0.1Å (or 0.6eV)[23,24,25]. However, this line width was similar to the expected spin-orbit splitting of the Ga 3d core levels[26] in GaAs (0.53eV), thus the splitting of the Ga 3d levels could not be resolved and detailed information could not be acquired. Soon after, *Cardona et al*[27] used continuous synchrotron radiation to study the 10 – 30eV region of the band structure from crystalline and amorphous materials such as GaAs, InAs, InP, GaP and GaSb. Table 1-1 shows the different transitions related to the energy difference between the outermost *d*-levels and the conduction band as described by *Cardona et al*[27] and Figure 1-9 illustrates each transition from the absorption spectrum of InAs (polycrystalline, single crystal and amorphous). The authors' notation is used in Table 1-1 and Figure 1-9, where D_{III} indicates the transition is from the *3d* level, the Δ_d denotes the spin-orbit splitting of the *3d* level and the superscripts 1 and 2 describe different levels in the conduction band to which the electrons are promoted. A table of experimental and theoretical values for the various transitions between the *d*-levels and the valence/conduction bands for relevant III-V compounds can be found in Appendix A.

Table 1-1. The energies (in eV) of the peaks observed in III-V compounds, related to the transitions from the outermost *d* levels of the cation core to the conduction band. From *Cardona et al*[27].

	GaP	GaAs	GaSb	InP	InAs	InSb
D_{III}^{1} ($3d^{5/2}$)	20.6[a] 20.9[b] 21.3[c]	20.9[a] 20.6[b] 21.0[c]	20.8[a] 20.45[b] 20.8[c]	18.8[a] 18.8[b]	18.5[a] 18.5[b]	18.3[a]
$D_{III}^{1}+\Delta_d$ ($3d^{3/2}$)	21.2[a]			19.75[a] 19.75[b]	19.5[a] 19.4[b] 19.6[c]	19.2[a] 18.9[b] 19.1[c]
D_{III}^{2}	23.1[a] 23.2[b] 23.3[c]	23.0[a] 22.9[b] 23.2[c]	22.4[a] 22.2[b] 22.5[c]	21.6[a] 21.6[b]	21.55[a] 21.3[b] 21.6[c]	20.8[a] 20.9[b] 21.0[c]
$D_{III}^{2}+\Delta_d$				22.4[a] 22.5[b]	22.3[a] 22.1[b]	21.5[a]
D_{III}^{3}	25[b]		24.4[b]	24.4[b]	26.0[a] 24.7[b]	25[c]
D_{III}^{4}			28.4[a] 28.3[b] 28.2[c]	28.5[a] 29.8[b]	29.2[a] 27.5[b] 27.5[c]	

[a] Results are from transmission of thin polycrystalline films.
[b] Results are from reflection of single crystals.
[c] Results are from electron energy loss data.

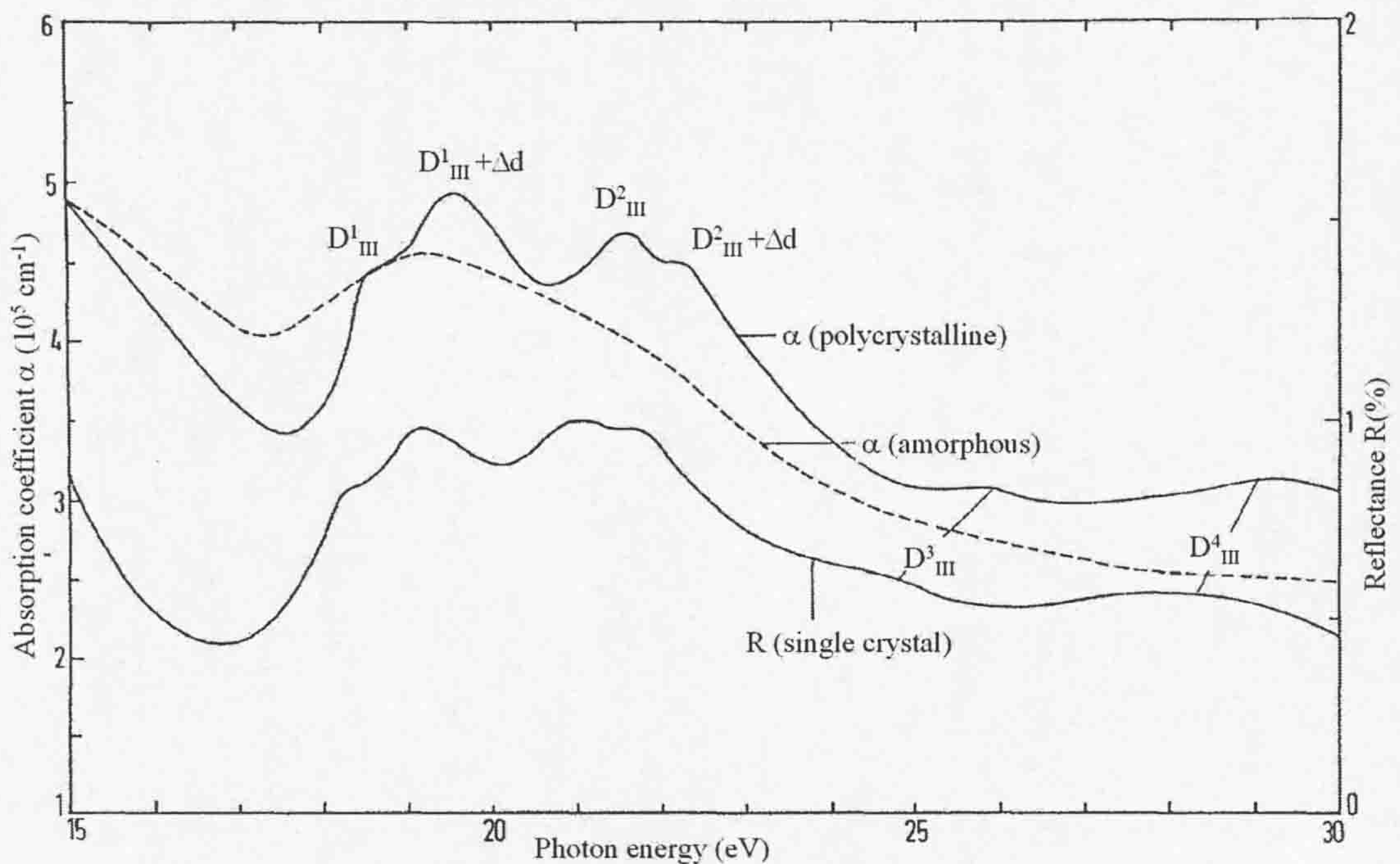

Figure 1-9. Absorption (crystalline, amorphous) and reflection spectra (single crystal) of InAs illustrating the different transitions between the outermost *d* levels and the conduction band. From *Cardona et al*[27].

By the mid 1970s, many groups were trying to understand the valence band structure and spin-orbit splitting of III-V and II-VI binary and ternary compounds. Methods such as X-ray photoemission spectroscopy[28], synchrotron-radiation Schottky-barrier electroreflectance (ER)[29,30,31,32] and energy derivative reflectance (EDR)[33] were used. Tables were published detailing all the transitions from the d levels with the spin orbit splitting j=3/2 and j=5/2, to the conduction band minima (see Appendix A for examples). However, inconsistencies existed within the ordering of the Γ-L-X conduction band minima in GaAs. In 1960, *Ehrenreich*[34] observed that if the L minimum was above the X minimum in energy, then all existing data could be explained, giving an ordering of Γ-X-L of the conduction band minima. This model had become generally accepted by the 1970's, until in 1976, *Aspnes*[32] found that without exception, all the existing experimental data could be reinterpreted to give the Γ-L-X ordering of the conduction band minima, and also the ordering of the VB to CB energy gaps, with the band gap E_0 at the zone centre, Γ. This has since been verified and the Γ-L-X ordering of the conduction band can be seen in Figure 1-10, the band structure diagram of GaAs. The band diagram of GaAs will be referred to when discussing the results.

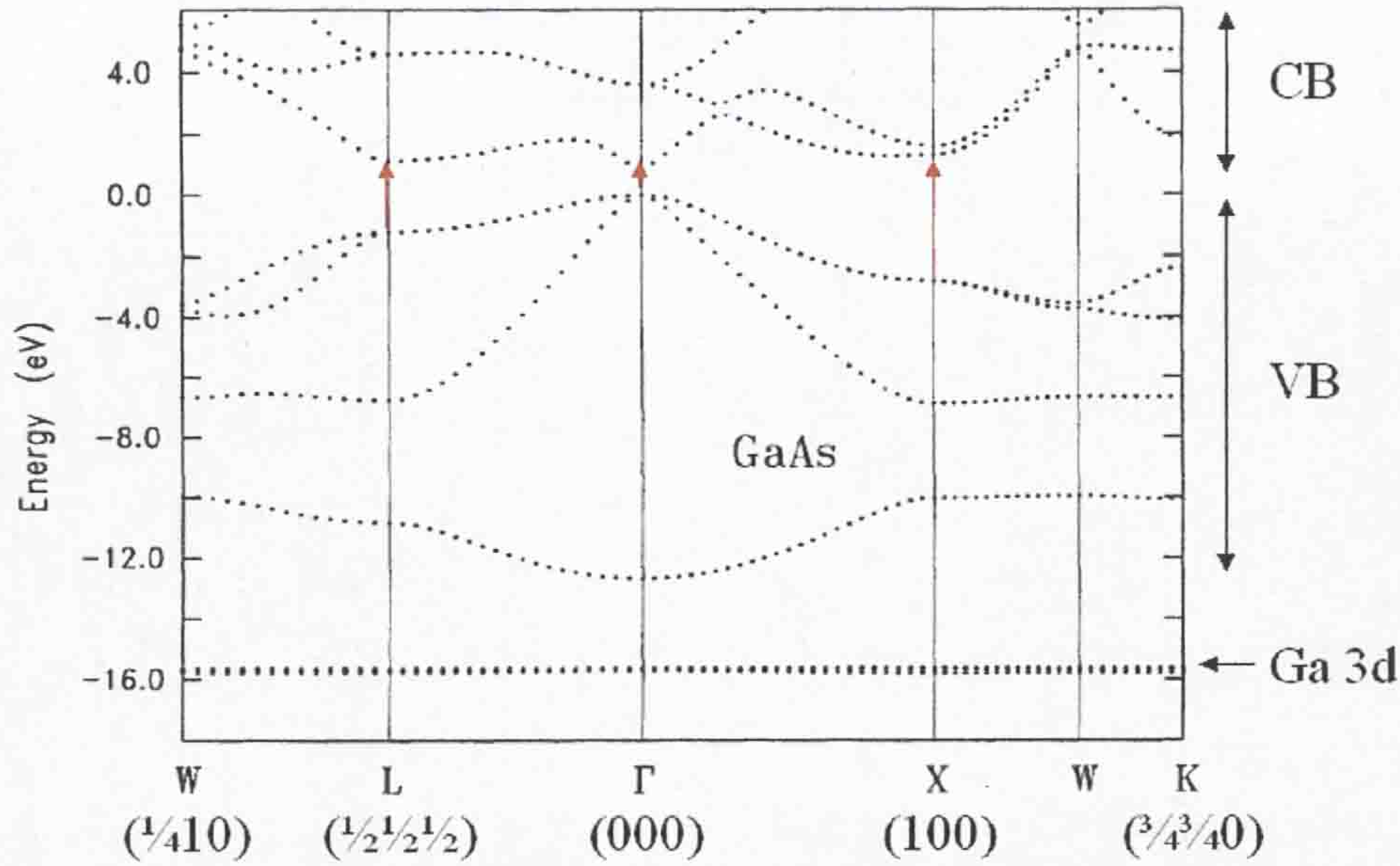

Figure 1-10. The band structure diagram of GaAs demonstration the Γ-L-X ordering of the conduction band minima and the proximity of the Ga 3d bands to the valence bands.

1.4.2 Band gap of III-V semiconductor materials

The band gaps of most conventional ternary III-V semiconductor alloys (non N-containing), such as AlGaAs, GaInAs and GaInP, can be approximated reasonably well by a weighted linear average of the band gaps of the parental binary compounds using the following relationship,

$$\Delta E_g(x) = bx(x-1) \tag{1.1}$$

Where, ΔE_g is the change in band-gap from the binary system, x is the fraction of the dominant group III element, and b, the bowing coefficient is typically a fraction of an eV. However, the III-V alloys containing N display substantial bowing in the band gap energy as a function of composition[35], thus Equation 1.1 cannot be applied, and alternative methods of fitting the band gap – composition relationship have been

investigated. Moreover, the bowing coefficient is also dependant on the strain in the Ga(In)NAs epilayer, created due to the mismatch with the substrate material[36].

Several explanations for the strong reduction in the band gap energy of III-V-N alloys with increased N incorporation have been proposed:

1) The *Van Vechten* model[37] proposes that the large electronegativity of N atoms causes bowing in the conduction band (CB) of GaNAs alloys, with a bowing coefficient of 20eV. For low nitrogen contents (x<0.02), this dielectric model proves to be in good agreement with experimental results. However, as this model uses a constant bowing coefficient, it predicts a negative band gap for large parts of the composition range as is demonstrated in Figure 1-11. This model was subsequently disproved when other groups demonstrated that there is a reduction of the bowing coefficient with the increase of N content[38,39].

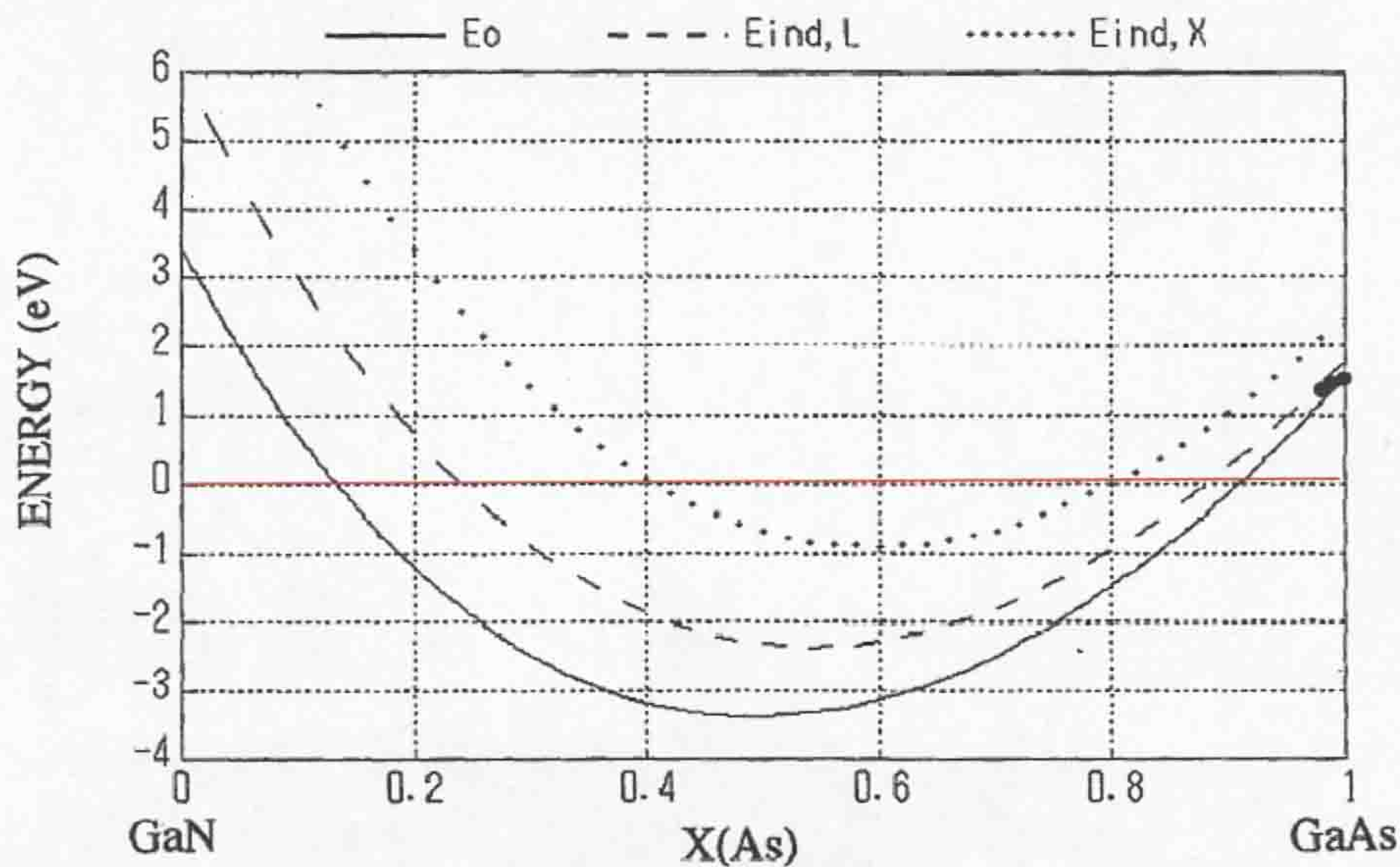

Figure 1-11. The band-gap of $GaAs_xN_{1-x}$ alloys determined by the *Van Vechten* model predicts negative band gaps for large parts of the composition range. From *Sakai et al*[37]

2) The band anticrossing model has been widely applied to dilute nitrides. Two main spectral features occur in most direct band gap zinc-blende III-V semiconductors without nitrogen. The first is the transition between the top of the valence band to the bottom of the conduction band, i.e. the band gap, denoted as the E_0 (or E_-) transition. The second is a transition from the top of the spin-orbit split-off valence band (VB) to the bottom of the conduction band (CB), known as the $E_0 + \Delta_0$ (or $E_- + \Delta_0$) transition. Using photomodulation spectroscopy, *Shan et al*[40,8] proposed that there is a strong interaction between the conduction band and a narrow resonant band formed by nitrogen states in the GaInNAs alloys, giving an additional transition E_+. Whilst the E_- and $E_- + \Delta_0$ transitions both decrease with the increase of In and N (thus reducing the band gap), the E_+ transition increases, demonstrating that the splitting between E_- and E_+ also increases with the increase in nitrogen. The band anticrossing model regards the E_- and E_+ energy levels as the splitting of the CB due to the interaction of the Γ CB minimum and the nitrogen related level E_N, where the nitrogen level has an energy of $E_N = E_v + 1.65$ eV.

3) The first principle local-density approximation (LDA) calculations of the band structure[41,42] of dilute nitrides, makes use of the highly localised perturbation due to the addition of N atoms with a large chemical and size difference compared to As, leading to a reduction in crystal symmetry. The reduction in crystal symmetry is responsible for the splitting of the conduction band minima (L and X in GaAs), creating the a_1L and a_1X states in Ga(In)NAs. The delocalised conduction band minimum $a_1\Gamma$, and the introduction of the nitrogen-localised a_1N-state, also have an effect on the

band structure. In LDA calculations, mixing between the $a_1\Gamma$ and a_1L states is responsible for the E_- sub-band formation and this interaction increases with the increase in N concentration. However, the interaction with the X-states is only of significance under pressure[42]. The E_+ state is a consequence of an interaction between the a_1N resonant state and the a_1L state, and increases with N composition.

1.4.3 Photoluminescence studies of GaInNAs materials

Photoluminescence (PL) spectroscopy is a characterisation technique that is carried out on semiconductors to obtain important material properties such as band gap energies. Unlike many other methods, it is a non-contact, non-destructive method of probing the electronic structure. A light of specific frequency ν ($h\nu > E_g$) is focussed onto the specimen, which then absorbs the light and imparts excess energy into the material, a process known as photo-excitation. Upon photo-excitation, the electrons in the material are excited into allowed states. When the electrons relax to their equilibrium states, the excess energy is released, some of which may be as the emission of light at specific energies, or photoluminescence. In semiconductors, the most common radiative transition is between the conduction and valence bands, or band gap, hence the band gap energy, or wavelength of the material can be easily measured.

The material's optical quality may also be determined through PL. To make device performance material, most semiconductors must be defect free (such as

dislocations)[ii]. As dislocations tend to undergo a non-radiative process on photo-excitation, the material's quality may be determined by quantifying the extent of radiative recombination.

Many different sources such as Ar^+ lasers (λ = 514.1nm[43] and λ = 488nm[4]), He-Ne lasers (λ = 633nm)[44, 45] and K^+ lasers (λ = 647nm)[10] have been used to determine the wavelength and band gap of GaInNAs quantum well structures. A range of temperatures are employed for the PL measurements from T = 2 to 300 K, to determine the temperature dependence, since GaInNAs is a material proposed for high T operation.

1.4.4 Effective mass (m_e^*)

Effective mass is a very important parameter for semiconductor materials as it allows electrons and holes to be treated as classically charged particles. Its value is related to the mobility of charge carriers in semiconductors as well as the density of states and can be determined from the parabola of the conduction band:

$$m_e^* = \left[\frac{d^2E}{dp^2} \right]^{-1} \qquad 1.2$$

where E is the electron energy and p is the momentum.

A number of groups have investigated the influence of composition upon m_e^* in dilute nitrides[46,47,48,49,50,51,52,53]. These studies generally indicate that the incorporation of nitrogen into Ga(In)As increases m_e^*, although incorporation of

[ii] There is an exception of GaN based semiconductor materials, which, although they contain many defects, appear to perform well as devices. The understanding of this phenomenon is at the centre of many current research projects.

nitrogen in GaAs has been reported to both decrease and increase m_e* [53]. In the case of GaInNAs, the magnitude of the reported increase varies significantly between studies and most experimental values of m_e* have been obtained using indirect methods such as the analysis of the carrier confinement energies[46,47,49]. It has also been previously established[54] that the direct measurement of the effective electron mass m_e* in bulk GaAs and Si can be calculated using a *Kramers-Kronig* analysis of optical reflectivity measurements. To date, direct measurements of m_e* using cyclotron resonance have been limited to GaNAs with very low nitrogen concentrations[48].

1.4.5 *Kramers-Kronig* transformation

The *Kramers-Kronig* (KK) relationship was first introduced in 1927[55], by Kramer, who drew on earlier remarks from Kronig on the subject (although he mentions that he derived the equations in 1925 when he presented them to the Danish Academy). The relationship allows the imaginary part of a susceptibility, permeability or permittivity to be found as a function of the frequency once the real part is known, and consists of two parts, generally accepted to be written as:

$$\chi_r(\omega) = \frac{1}{\pi} P \int_{-\infty}^{\infty} \frac{\chi_i(\omega')}{\omega' - \omega} d\omega' \qquad 1.3$$

and

$$\chi_i(\omega) = -\frac{1}{\pi} P \int_{-\infty}^{\infty} \frac{\chi_r(\omega')}{\omega' - \omega} d\omega' \qquad 1.4$$

Where $\chi(\omega)$ is the electric susceptibility, real (r) and imaginary (i) respectively, ω and ω' are real and independent values of the angular frequency, and P denotes the Cauchy principal value of the integral.

These transformations have become widely used as a method for the determination of the optical properties of materials, such as the absorption coefficient and reflectivity. They have also been used to calculate the density of states for materials and in formulating band structures[56]. Many materials have been studied using the KK analysis ranging from black fluorinated rubber[57] through to diamond[58]. Semiconductor materials have also been investigated using this approach. Their optical properties are implicitly related to their semi-conducting behaviour, and consequently a significant effort has been spent in understanding them, a full review of the KK transformation will be covered in Chapter 2.

1.5 TEM studies of GaInNAs

1.5.1 Transmission electron microscopy studies of GaInNAs and related materials

(Scanning) transmission electron microscopy or (S)TEM can produce images of the microstructure of materials with better than a nanometer resolution. (S)TEM is particularly useful when looking at the distribution of elements in different layers of a cross-section from device structures, such as QWs and laser structures. Chemical analysis can be carried out using energy dispersive X-ray (EDX) analysis and, with electron energy loss spectroscopy (EELS) in a (S)TEM, both chemical and elemental information can be acquired from the material. STEM has the advantage

over TEM for EELS analysis as point analysis, line scans and maps can be acquired with the energy loss data obtained in a parallel manner.

The distribution of indium and nitrogen within the GaInNAs QW has a significant effect on the emission characteristics[10]. Previously, TEM has been used to reveal the formation of quantum dot-like features in GaInNAs QWs via atomic number contrast[9]. The model used to describe these dot structures envisaged the GaInNAs / GaAs QWs in terms of non-uniform N and In compositions. Comparison of $Ga_{0.7}In_{0.3}As$/GaAs and $Ga_{0.7}In_{0.3}N_{0.02}As_{0.98}$/GaAs wells showed undulating structures in both wells, which were attributed to lateral variations in strain. This effect was more pronounced in the N-containing quantum wells due to non-uniform In and N concentrations. S. Thomas[59] carried out the characterization of the elemental distribution of GaInNAs QWs and thin films through EDX analysis in a STEM and through strain analysis in high-resolution electron microscopy (HREM).

1.5.2 Electron energy loss spectroscopy of Ga(In)(N)As and GaN

Energy loss spectroscopy is the study of the energy loss of an incident source after interaction with a specimen. Energy is lost to the specimen by exciting atomic electrons to higher energy states. As the energy states in atoms are discrete, only certain energies can be lost for specific elements, hence these energies can be characterised.

The theory of energy loss processes associated with high energy electrons interacting with specimens has been around since the early 20th Century, and has been utilised experimentally in several ways. The energy loss may be studied using

either the reflection or transmission of electrons. As a result, several techniques have been developed to allow for different analysis configurations. High-resolution electron energy loss spectroscopy (HREELS) concentrates on the 0 – 10eV energy loss and can be either a transmission or a reflection technique. Reflected electron energy loss spectroscopy (REELS) is a reflection technique using a hemispherical analyser which typically covers the electron energy range 10 – 5000eV. Electron energy loss spectroscopy (EELS) in a (S)TEM is a technique where the energy loss of an incident electron beam passing through a specimen is measured. When this is in a "parallel" manner (i.e. all electron energy losses over a given range are collected) it is known as PEELS. Another technique similar to PEELS is energy filtered TEM (EFTEM). In this case, spectrum images are acquired from the electrons that have lost specific energies, hence spatial information is acquired in a parallel manner and the spectral information must be acquired serially.

The EELS technique has many applications, and can be used to determine the optical, electronic and mechanical properties of a material[60,61,62]; two main energy regions are investigated in EELS:

1) The energy-loss range between 50eV and 3000eV is conventionally used for the study of lighter elements, which cannot be detected by energy dispersive X-ray (EDX) analysis to give information on core loss through analysis of the ionisation edges. Closer analysis of the energy loss near-edge structure (ELNES) may give information on bonding and the density of states (DOS).
2) Below 50eV, information about the outer shell electrons can be obtained including band gap energies, plasmon effects and joint DOS amongst others.

Keast et al (e.g.[61]) have extensively studied the ELNES of (In)GaN materials. These edges, for example the N-K edge, are the result of a transition from the core (K) electrons into unoccupied electron states. By studying the fine structure in the edges, the DOS may be calculated. *Keast et al*[63] have also studied the low loss region from GaN and noted the shift in plasmon peak towards lower energies with the introduction of In. Moreover, they observed additional peaks at slightly higher energies (23 – 29eV) and related them to the transition of the Ga (or In) 3d state to the unoccupied states[63].

Another area of interest in using EELS is for the study of the band gap transitions in semiconductor materials. As these transitions often occur at very low energies (0.1eV to ~4eV), optical spectroscopy techniques are frequently used, which offer very high-energy resolution in the order of 1 – 500 meV. Unfortunately, the spatial resolution of these techniques is often limited, achieving in the range of microns at best[64]. Alternatively, by studying the EELS spectrum in a STEM a spatial resolution can be achieved in the order of a nanometre. However, the energy resolution is poor in comparison, ranging typically from 0.3 – 1.0eV. The energy resolution of EELS in a TEM will improve in the future, with the introduction of monochromated FEG-TEM's, but will still not reach the resolution of optical methods. A compromise must therefore be made on either energy or spatial resolution when low-energy loss data is to be analysed.

For large band gap semiconductor materials and insulators ($E_g > 3$ eV), it is possible to study the band-gap region using EELS in a TEM. In semiconductors and insulators, no electrons should lose energy less than their band gap energy[60].

Consequently, if the zero loss peak and plural scattering are removed from the energy loss spectrum to give a single scattered distribution, the onset of the spectrum will be at the band gap energy. This has been successfully demonstrated for large band gap semiconductor materials such as Ga(In)N[64] and AlN[65], and for insulators such as carbon in its different forms. Unfortunately, because of the energy resolution of EELS in the TEM, it cannot be used to measure the small band gap energies of semiconductor materials such as GaAs (1.42eV) or GaIn(N)As (~1eV), as the onset is masked in the zero loss peak (ZLP). For this, optical methods must be applied as described previously.

Until recently, most of the data published on EELS acquired in a (S)TEM has been from point analysis or energy filtered-TEM (EFTEM). Point analysis has excellent spatial resolution in a STEM, however it does not convey the spatial information of the EDX maps and could not be easily used to show segregation of elements. Several papers were published on spectrum-imaging in a STEM in the early 1990's (e.g.[66,67]). Spectral imaging is the acquisition of an entire EELS spectrum at every pixel in the image, permitting subsequent processing of data to be carried out off-line. However, the volume of information associated with the spectrum images was a major problem. For instance, a map of size 128 x 128 pixels would require 16 Mbytes of memory, and a *Kramers-Kronig* analysis to calculate the complex dielectric-response function would have an execution time of 55 minutes. It is only recently, with the improvements in computer technology and increased processing speeds that the idea of spectrum imaging has become feasible. Companies like Gatan have taken this opportunity to produce their Enfina™ spectrometer with a spectrum-imaging software package. This allows spectrum images to be acquired,

where each pixel contains a spectrum between user specified limits. These can then be analysed as point- or line-spectra or as entire maps, which can show (among others), elemental distributions and variations in electronic structure. *Kramers-Kronig* transformation of a spectrum image (128 x 128 pixels) now takes around 10 minutes and can compute additional parameters such as sample thickness, effective number of electrons, optical absorption etc, (further details can be found in Chapter 3). *Scheu et al*[68] published the first results using this equipment and demonstrated how the atomic percentage of Ga in an Al-2at%Ga alloy can be mapped using the Ga-$L_{2,3}$ edge. EFTEM on the other hand has been able to acquire excellent energy selected images for some time[69], however, unlike PEELS, the whole energy spectrum cannot be acquired. The operator must have an understanding of the material and the elements present, so that the correct energy slices are selected before the data is acquired.

To date there has been little data published on EELS of GaInNAs, and the work that has been published is based on work for this thesis[70,71].

References

[1] M. Kondow, T. Kitatani, S. Nakatsuka, M. Larson, K. Nakahara, Y. Yazawa, M. Okai and K. Uomi, IEEE, **3**, 719 (1997)

[2] S. Fischer, D. Fekete, G. Feak and J. Ballantyne, Appl. Phys. Lett., **50**, 714 (1987)

[3] M. Kondow, K. Uomi, A. Niwa, T. Kitatani, S. Watahiki and Y. Yazawa, Japp. J. Appl. Phys., **35**, 1273-1275 (1996)

[4] J.-M. Chauveau, A. Trampert, M.-A. Pinault, E. Tournié, K. Du and K.H. Ploog, J. Crystal Growth, **251**, 383-387 (2003)

[5] V.M. Ustinov, A.Y. Egorov, V.A. Odnoblyudov, N.V. Kryxhanovskaya, Y.G. Musikhin, A.F. Tsatsul'nikov and Z.I. Alferov, J. Crystal Growth, **251**, 388-391 (2003)

[6] H.P. Xin, K.L. Kavanagh and C.W. Tu, J. Crystal Growth, **208**, 145-152 (2000)

[7] Z. Pan, L.H. Li, W. Zhang, Y.W. Lin, R.H. Wu and W. Ge, Appl. Phys. Lett., **77**, 1280-1282 (2000)

[8] W. Shan, W. Walukiewicz, J.W. Ager, E.E. Haller, J.F. Geisz, D.J. Friedman, J.M. Olson and S.R. Kurtz, J. Appl. Phys., **86**, 2349 (1999)

[9] T. Kageyama, T. Miyamoto, S. Makino, F. Koyama and K. Iga, Jap. J. Appl. Phys., **38**, L298 (1999)

[10] S. Mazzucato, A. Erol, R.J. Potter, N. Balkan, P.R. Chalker, S. Thomas, T.B. Joyce and T.J. Bullough, Solid-State Elect., **47**, 483 (2003)

[11] J.B. Heroux, X. Yang and W.I. Wang, Appl. Phys. Lett., **75**, 2716-2718 (1999)

[12] D.J. Friedman, J.F. Geisz, S.R. Kurtz and J.M. Olson, J. Crystal Growth, **195**, 409 (1998)

[13] S.R. Kurtz, A.A. Allerman, E.D. Jones, J.M. Gee, J.J. Banas and B.E. Hammons, Appl. Phys. Lett., **74**, 729-731 (1999)

[14] H.P. Xin, C.W. Tu and M. Geva, Appl. Phys. Lett., **75**, 1416-1418 (1999)

[15] J. Singh, Semiconductor Devices, An Introduction, McGraw-Hill, Inc. (1994)

[16] T. Chen, L. Eng, Y. Zhuang, Y. Xu, H. Zaren and A Yariv, Appl. Phys. Lett. **57**, 2762 (1990)

[17] V. Ustinov, N. Maleev, A. Zhukov, A. Kovsh, A. Egorov, A. Lunev, B. Volovik, I. Krestnikov, Y. Musikhin, N. Bert, P. Kop'ev, Z. Alferov, N. Ledenstov and D. Bimberg, Appl. Phys. Let. **74**, 2815 (1999)

[18] M. Kondow, K. Uomi, A. Niwa, T. Kitatani, S. Watahiki and Y. Yazawa, Solid State Device and Materials, 1016-1018 (1995)

[19] J.F. Geisz, D.F. Friedman, J.M. Olson, S.R. Kurtz and B.M. Keyes, J. Crystal Growth, **195**, 401 (1998)

[20] B.V. Volovik, A.R. Kovsh, W. Passenberg, H. Kuenzel, N. Grote, N.A. Cherkashin, Y.G. Musikhin, N.N. Ledentsov, D. Bimberg and V.M. Ustinov, Semicond. Sci. Technol., **16**, 186 (2001)

[21] G.G. MacFarlane, T.P. McLean, J.E. Quarrington and V. Roberts, Proceedings of the Physical Society of London, **71**, 863 (1958)

[22] J.C. Phillips, Solid State Physics, Academic, New York, (1966)

[23] J.A.R. Sampson, Techniques of Vacuum Ultraviolet Spectroscopy, Wiley, New York (1967)

[24] H.R. Philipp and H. Ehrenreich, Phys. Rev. Lett., **8**, 92 (1962)

[25] H.R. Philipp and H. Ehrenreich, Phys. Rev., **129**, 1550 (1963)

[26] F. Herman and S. Skillman, Atomic Structure Calculations, Prentice-Hall, Englewood Cliffs, N.J. (1963)

[27] M. Cardona, W. Gudat, E.E. Koch, M. Skibowsil, B. Sontag and P.Y. Yu, Phys. Rev. Lett., **25**, 659 (1970)

[28] L. Ley, R.A. Pollak, F.R. McFeely, S.P. Kowalczyk and D.A. Shirley, Phys. Rev. B, **9**, 600 (1974)

[29] D.E. Aspnes, C.G. Olson and D.W. Lynch, Phys. Rev. B, **12**, 2527 (1975)

[30] D.E. Aspnes, C.G. Olson and D.W. Lynch, Phys. Rev. B, **14**, 2534 (1976)

[31] D.E. Aspnes, C.G. Olson and D.W. Lynch, Phys. Rev. B, **14**, 4450 (1976)

[32] D.E. Aspnes, Phys. Rev. B, **14**, 5331 (1976)

[33] D.E. Aspnes, M. Cardona, V. Saile, M. Skibowski and G. Sprüssel, Solid State Comm., **31**, 99 (1979)

[34] H. Ehrenreich, Phys. Rev., **120**, 1951 (1960)

[35] M. Kondow, K. Uomi, K. Hosomi and T. Mozume, Japp. J. Appl. Phys., **33**, L1056 (1994)

[36] K. Uesugi, N. Morooka and I. Suemuna, Appl. Phys. Lett., **74**, 1254 (1999)

[37] S. Sakai, Y. Ueta and Y. Terauchi, Japp. J. Appl. Phys., **32**, 4413 (1993)

[38] W.G. Bi and C.W. Tu, Appl. Phys. Lett., **70**, 1608 (1997)

[39] K. Uesugi and I. Suemune, Jap. J. Appl. Phys., **36**, L1572 (1997)

[40] W. Shan, W. Walukiewicz, J.W. Ager, E.E. Haller, J.F. Geisz, D.J. Friedman, J.M. Olson and S.R. Kurtz, Phys. Rev. Lett., **82**, 1221 (1999)

[41] E.D. Jones, N.A. Modine, A.A. Allerman, S.R. Kurtz, A.F. Wright, S.T. Torez and X. Wei, Phys. Rev. B, **60**, 4430 (1999)

[42] T. Mattila, S.-H. Wei and A. Zunger, Phys. Rev. B, **60**, R11245 (1999)

[43] B.V. Volovik, A.R. Kovsh, W. Passenberg, H. Kuenzel, N. Grote, N.A. Cherkashin, Y.G. Musikhin, N.N. Ledentsov, D. Bimberg and V.M. Ustinov, Semicond. Sci. Technol., **16**, 186 (2001)

[44] X. Liang, D. Jiang, B. Sun, L. Bian, Z. Pan, L. Li and R. Wu, J. Cryst. Growth, **243**, 261 (2002)

[45] T. Kageyama, T. Miyamoto, S. Makino, F. Koyama and K. Iga, Jap. J. Appl. Phys., **38**, L298 (1999)

[46] Z. Pan, L. H. Li, Y. W. Lin, B. Q. Sun, D. S. Jiang, and W. K. Ge, Appl. Phys. Lett. **78**, 2217 (2001)

[47] M. Hetterich, M. D. Dawson, A. Yu. Egorov, D. Bernklau, and H. Riechert, Appl. Phys. Lett. **76**, 1030 (2000)

[48] P. N. Hai, W. M. Chen, I. A. Buyanova, H. P. Xin, and C. W. Tu, Appl. Phys. Lett. **77**, 1843 (2000)

[49] Y. Zhang, A. Mascarenhas, H. P. Xin, and C. W. Tu, Phys. Rev. B **61**, 7479 (2000)

[50] S. Mazzucato and N. Balkan, A. Teke, A. Erol, R. J. Potter, M. C. Arikan, X. Marie, C. Fontaine, H. Carrère, E. Bedel, and G. Lacoste, J. Appl. Phys. **93** (5) 2440 (2003)

[51] C. Skierbiszewski et al., Appl. Phys. Lett. **76**, 2409 (2000)

[52] A. Lindsay and E. P. O'Reilly, Solid State Commun. **122**, 443 (1999)

[53] D.L. Young, J.F. Geisz and T.J. Coutts, Appl. Phys. Lett. **82**, 1236 (2003)

[54] E. Barta, Infrared Physics, **17**, 111 (1977)

[55] H.A. Kramer, Atti Congr. Intern. Fis., Como-Pavia-Roma, **II**, 545 (1927)

[56] J.L.P. Hughes, Y. Wang and J.E. Sipe, Phys. Rev. B, **55**, 13630 (1997)

[57] Shimadzu Application News, A228, Shimadzu Corp. (2000)

[58] C.J. Fall, A.T. Blumenau, R. Jones, P.R. Briddon, T. Frauenheim, A. Gutiérrez-Sosa, U. Bangert, A.E. Mora, J.W. Steeds and J.E. Butler, Phys. Rev. B, **65**, 205206 (2002)

[59] S. Thomas, Thesis: Structural, compositional and ICP processing analysis of CBE grown InGaAsN/GaAs, The University of Liverpool (2003)

[60] R.F. Egerton, Electron Energy Loss Spectroscopy in the Electron Microscope, Plenum Press, New York (1996)

[61] V.J. Keast, A.J. Scott, R. Brydson, D.B. Williams and J. Bruley, J. Microsc., **203**, 135 (2001)

[62] V.J. Keast, M.J. Kappers and C.J. Humphreys, J. Microsc., **210**, 89 (2003)

[63] V.J. Keast, A.J. Scott, M.J. Kappers, C.T. Foxon and C.J. Humphreys, Phys. Rev. B, **66**, 125319 (2002)

[64] G. Brocket and H. Lakner, Micron, **31**, 435 (2000)

[65] A.D. Dorneich, R.H. French, H. Müllejans, S. Loughin and M. Rühle, J. Microsc., **191**, 286 (1998)

[66] C. Jeanguillaume and C. Colliex, Ultramicroscopy, **28**, 252 (1989)

[67] J.A. Hunt and D.B. Williams, Ultramicroscopy, **38**, 47 (1991)

[68] C. Scheu, M. Gao, K. Van Benthem, S. Tsukimoto, S. Schmidt, W. Sigle, G. Richter and J. Thomas, J. Microsc., **210**, 16 (2003)

[69] P. Thomas, Thesis: Energy-Filtered Imaging in the Transmission Electron Microscope: Novel Techniques and Applications, The University of Cambridge (2000)

[70] M.H. Gass, A.J. Papworth, T.J. Bullough, and P.R. Chalker, Ultramicroscopy, **101**, 257 (2004)

[71] M.H. Gass, A.J. Papworth, T.B. Joyce, T.J. Bullough, P.R. Chalker, Appl. Phys. Lett., **84**, 1453 (2004)

Chapter 2

Electron-Sample interactions

Section		**Page**
2.1	Elastic Scattering	36
2.2	Inelastic scattering	38
2.3	The Energy Loss Spectrum	43
2.4	Outer-Shell Excitation	45
2.5	Inner-shell excitations	50
2.6	Single scattering of electrons	51

2 Electron-Sample interactions

The scattering of fast electrons in solids may be divided into two components; elastic and inelastic, where the term elastic can be taken to mean that the energy loss to the sample is less than the experimental resolution.

In this chapter both elastic and inelastic scattering will be considered with the different theories of calculating the probability of an incident electron being scattered (the differential cross section). The energy loss spectrum will then be discussed in detail, considering both the outer- and inner-shell interactions, and the effect of specimen thickness on obtaining single scattered data.

2.1 Elastic Scattering

2.1.1 Introduction

The interaction of the incident electrons with the electrostatic field of the atomic nucleus is known as elastic scattering. The electrons are attracted by the positive nucleus and are scattered with an angle θ, which increases as the impact parameter b decreases, Figure 2-1. As the nucleus is far more massive than the incident electron, the energy transfer is negligible for the collection angles in (S)TEM analysis[i]. It must be noted that although elastic scattering is generally not directly studied in EELS, it must be understood due to its implication for the EELS spectrum,

- Some electrons undergo both elastic and inelastic scattering, thus the angular distribution of the inelastically scattered electrons is modified.

[i] For electrons scattered at greater angles for example, $\theta \geq \pi$, the energy transfer can be significant.

- The intensity of elastic scattering can provide an estimate of the local atomic number of a specimen.
- Elastic scattering may redistribute the electron flux in unit cells of a crystalline material, hence alter the probability of certain inelastic scattering events.

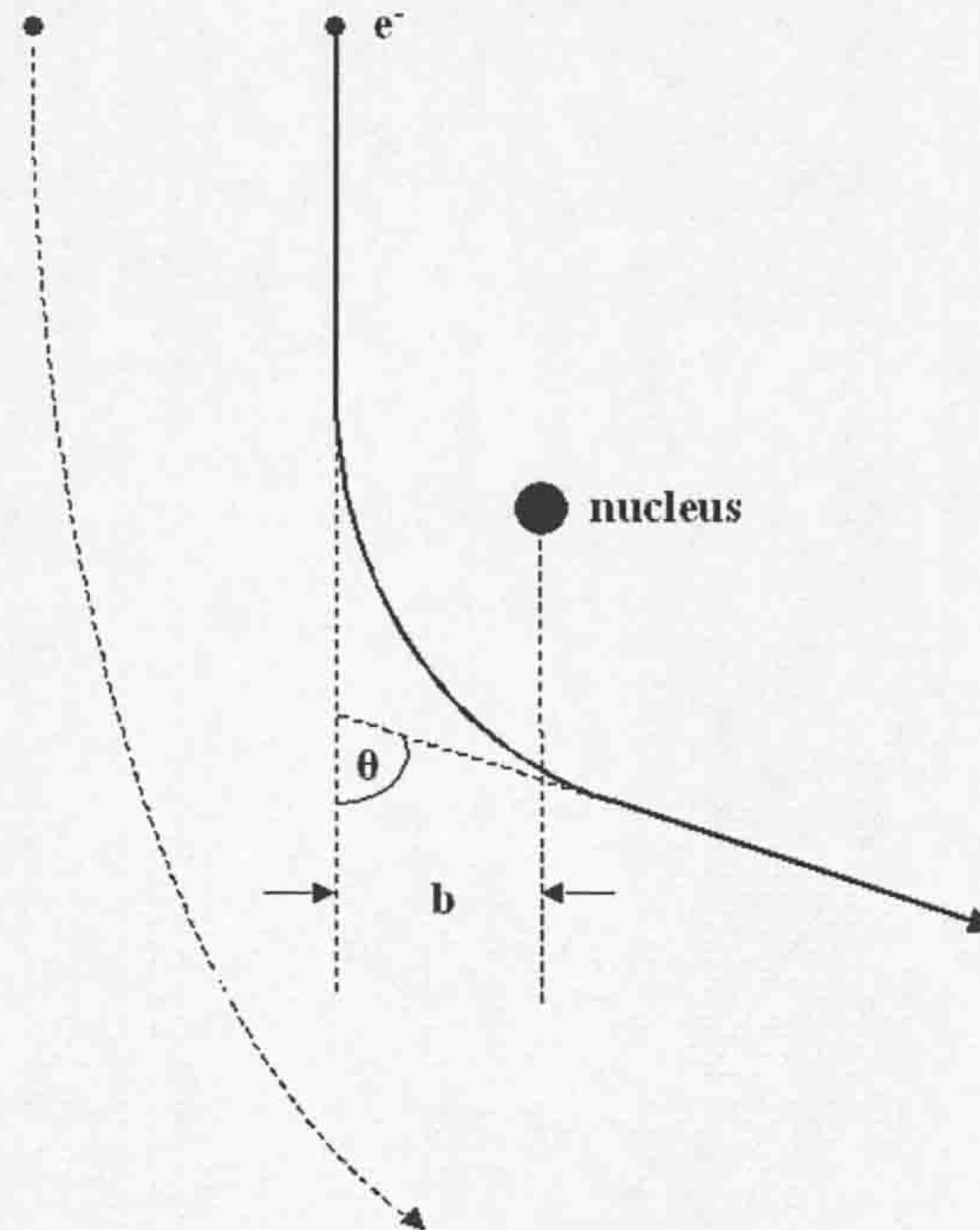

Figure 2-1. The Rutherford scattering of an incoming electron as it passes the nucleus shows that the closer the incoming electron is to the nucleus, i.e. the smaller b is, the greater the angle of deflection, θ, from the original trajectory.

A thorough discussion of the interference of electron scattering from each unit cell may be found in *Egerton*[1].

2.1.2 Differential cross-section for elastic scattering

The differential cross section represents the probability of an incident electron being scattered (per unit solid angle Ω) by a given atom. For the elastic differential cross section it may be related to the complex scattering amplitude *f(q)* by,

$$\frac{d\sigma}{d\Omega} = |f(q)|^2 \qquad 2.1$$

f(q) is a measure of the amplitude of an electron wave scattered from an isolated atom and is a function of the scattering vector **q**.

The *Mott* formula[2] considers interaction with a 'real' atom and is expressed in terms of an elastic form factor $F_{el}(q)$,

$$\frac{d\sigma}{d\Omega} = \frac{4}{a_0^2 q^4}|F_{el}(q)|^2 = \frac{4\gamma^2}{a_0^2 q^4}|Z - f_x(q)|^2 \qquad 2.2$$

Where a_0 is the Bohr radius, γ is a relativistic factor and $f_x(q)$ is the x-ray atomic scattering factor. The dependence on atomic number, *Z*, shows that the incident electrons are scattered by the entire electrostatic field of an atom while the X-rays interact mainly with the atomic electrons.

2.2 Inelastic scattering

Inelastic scattering results from the interaction of the incident electrons with either outer- or inner-shell atomic electrons. Excluding the ZLP, this is what constitutes the EELS spectrum. The energy loss spectrum can be split into three main regions,

- The ZLP, elastically scattered electrons, previously discussed in section 2.1,

- The low-loss, arising from the interaction with outer-shell electrons,
- The core-loss, arising from the interaction with inner-shell electrons.

Combinations of these interactions may also occur, and the data collected must be treated with caution and interpreted with this in mind. The low- and core-loss will be further discussed in section 2.3; first the atomic model for inelastic scattering will be discussed.

2.2.1 Differential cross section for inelastic scattering

The *Bethe* theory[3] states that the differential cross section for a transition *n,* that describes the inelastic scattering of electrons by an atom, must specify the state of each atomic electron as a transition from an initial state of wave function ψ_0 to a final state of wave function ψ_n. Using the first *Born* approximation[4] this is,

$$\frac{d\sigma_n}{d\Omega} = \left(\frac{m_0}{2\pi\hbar^2}\right)^2 \frac{\mathbf{k_1}}{\mathbf{k_0}} \left| \int V(r)\psi_0\psi_n^* \exp(i\mathbf{q}\cdot\mathbf{r}) d\tau^2 \right| \qquad 2.3$$

Where $\mathbf{k_0}$ and $\mathbf{k_1}$ are wave vectors of the fast electron before and after scattering, as shown in Figure 2-2, $\mathbf{q}$ is the momentum and $\mathbf{r}$ is the position of the particle relative to the centre of the atom.

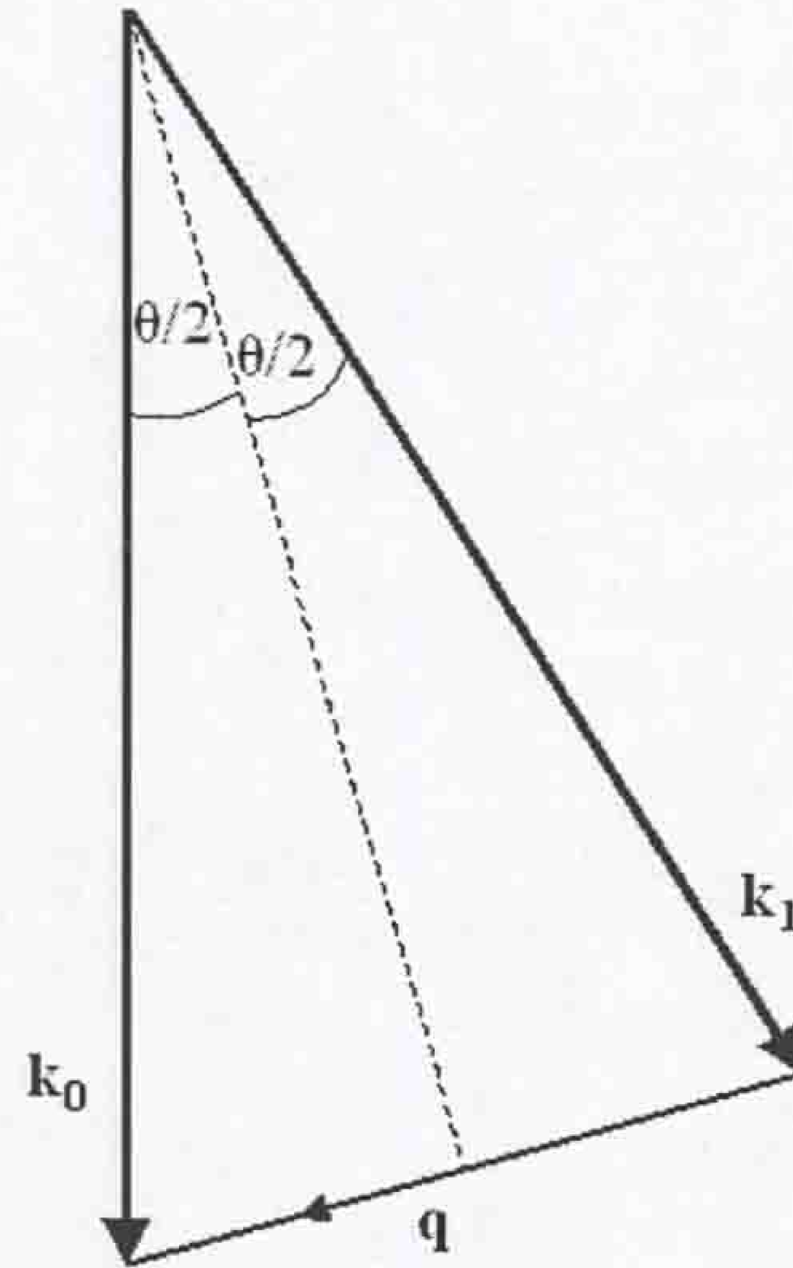

Figure 2-2. A schematic of the wave vectors of an incident electron, where $\mathbf{k_0}$ is the wave vector before scattering, $\mathbf{k_1}$ the vector after scattering at angle θ, and $\mathbf{q}$ is the scattering vector.

For incident energies less than 300 keV, equation 2.3 can be rewritten in the form,

$$\frac{d\sigma_n}{d\Omega} = \frac{4\gamma^2 R}{E_n \mathrm{q}^2} \frac{\mathrm{k}_1}{\mathrm{k}_0} f_n(q) \qquad 2.4$$

Where $f_n(q)$ is the generalized oscillator strength (GOS)[ii], γ is the usual relativistic factor, R is the Rydberg energy (13.6 eV) and E_n is the energy loss associated with the transition.

By defining the GOS per unit excitation energy, $df(q,E)/dE$, the energy loss spectrum may be defined as a continuous rather than a discrete function of energy loss, E. To achieve this, the angular and energy dependence of scattering are specified as a double differential cross section as follows,

[ii] GOS is defined as: $f_n(q) = \frac{E_n}{R} \frac{|\varepsilon_n(q)|^2}{(qa_0)^2}$, where $|\varepsilon_n(q)|^2$ is the dimensionless inelastic form factor.

$$\frac{d^2\sigma}{d\Omega dE} = \frac{4\gamma^2 R}{E\,\mathrm{q}^2}\frac{\mathrm{k}_1}{\mathrm{k}_0}\frac{df}{dE}(q,E) \qquad 2.5$$

By taking the approximation $k_1/k_0 = 1$ where $\theta << 1$ rad and $E << E_0$ (E_0 is the incident beam energy) and writing magnitude of the scattering vector, q as,

$$\mathrm{q}^2 = k_0^2(\theta^2 + \theta_E^2) \qquad 2.6$$

where the θ_E, characteristic angle is defined by,

$$\theta_E = \frac{E}{\gamma m_0 \upsilon^2} = \frac{E}{(E_0 + m_0 c^2)(\upsilon/c)^2} \qquad 2.7$$

The double differential cross section can be rewritten as,

$$\frac{d^2\sigma}{d\Omega dE} \approx \frac{8a_0^2 R^2}{E m_0 \upsilon^2}\left(\frac{1}{\theta^2 + \theta_E^2}\right)\frac{df}{dE} \qquad 2.8$$

where v is the velocity of the incident electron. The latter equation allows non-relativistic calculations of the inelastic cross sections from experimentally or theoretically determined generalized oscillator strengths.

2.2.2 Dielectric formulation

The *Bethe* theory gives a good estimation of the inelastic scattering, which takes place from single inner-atomic shell electrons. However, the outer shell of an atom has an added dimension concerning chemical bonding, thus the wave functions are somewhat modified. There are also collective effects involving many electrons for which the *Bethe* theory is no longer suitable. For the outer shell electrons another

approach where the interaction is explained in terms of the dielectric response function $\varepsilon(q,\omega)$ is useful. This describes the interaction of an external perturbation, for example transmitted electrons, with the entire solid. In 1957, Richie[5] explained that the double-differentiated inelastic scattering cross section could be related to the dielectric response function via,

$$\frac{d^2\sigma}{d\Omega dE} \approx \frac{\mathrm{Im}[-1/\varepsilon(q,E)]}{\pi^2 a_0 m_0 \upsilon^2 n_a}\left(\frac{1}{\theta^2+\theta_E^2}\right) \qquad 2.9$$

where the imaginary part of $[-1/\varepsilon(q,\omega)]$, known as the energy-loss function provides a complete description of the medium through which the fast electron is travelling. By comparing equations 2.8 and 2.9, it can be shown that they will equal if,

$$\frac{df}{dE}(q,E) = \frac{2E}{\pi E_a^2}\mathrm{Im}[-1/\varepsilon(q,E)] \qquad 2.10$$

where $E_a^2 = \hbar^2 n_a e^2/(\varepsilon_0 m_0)$, the plasmon energy, which corresponds to one free electron per atom.

EELS spectra that are acquired in the TEM have small collection angles, and $\varepsilon(q,E)$ varies little with **q**, thus may be replaced with the optical relative permittivity of the specimen $\varepsilon(0,E)$, at an angular frequency, $\omega = E/\hbar$. The EELS spectra can thus be directly compared to the optical data, after applying the *Kramers-Kronig* transformation to obtain $Re[1/\varepsilon(0,E)]$. The energy dependence of the real and imaginary parts, (written as ε_1 and ε_2 respectively) of $\varepsilon(0,E)$ can be studied and further information obtained.

2.3 The Energy Loss Spectrum

The energy loss spectrum consists of three main areas as indicated on Figure 2.3. The first area (section A) is the zero loss peak. This is the most intense part of the spectrum and consists of the elastically scattered electrons, described in section 2.1. The rest of the spectrum is the result of inelastically scattered electrons, and the two other sections consist of the low loss and core loss. The low loss region (section B) results from the interaction of the incident electrons with the outer-shell atomic electrons where the most important feature is the plasmon peak, described in section 2.4.1. The core loss (section C) results in interaction of the incident electron with the inner-shell atomic electrons described in section 2.5.

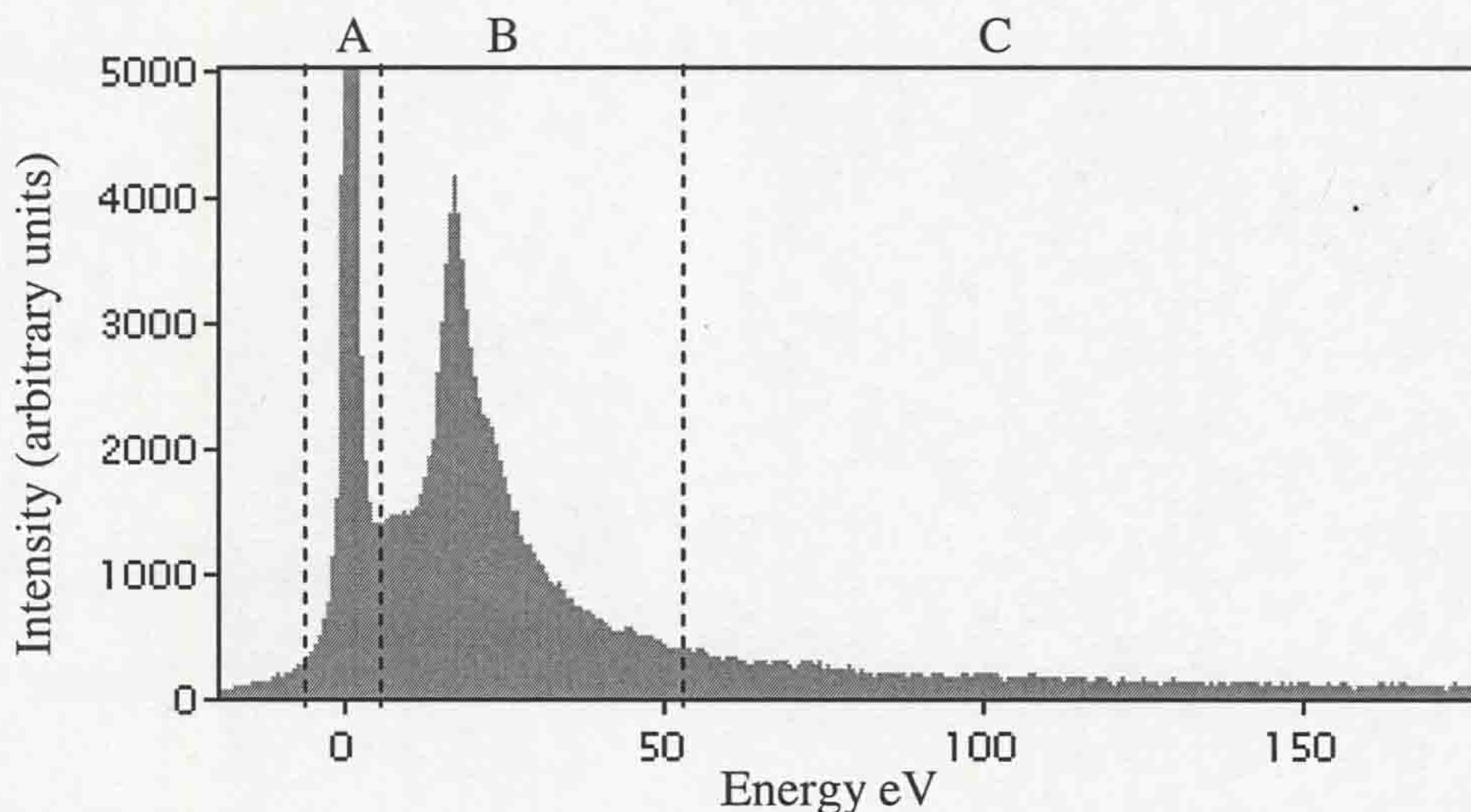

Figure 2-3. An energy loss spectrum defining the three main regions; A the zero loss peak, B the low-loss and C the core-loss which can extend to several thousand eV. The intensity on the *y*-axis is in arbitrary units.

It can be seen in Figure 2-3 that for energies above that of the plasmon, the spectrum consists of a gradually decreasing background caused by different interactions. Ionisation edges from core-loss are superimposed onto it. A small contribution to

the background may be instrumental, and this can be measured by taking a spectrum without a specimen and if it is significant it can be subtracted from the real data. The rest of the background is made up of contributions from many different scattering effects.

By integrating Equation 2.9 to get the 'energy dependent' cross-section we obtain,

$$\frac{d\sigma}{dE} \propto \mathrm{Im}\left(\frac{-1}{\varepsilon}\right)\ln\left(\frac{\beta}{\theta_E}\right) \qquad 2.11$$

By assuming that β is large compared to θ_E, it is shown that for low energy loss (after the plasmon) the intensity should decrease roughly as E^{-3} (as $Im(-1/\varepsilon)$ is proportional to E^{-3} as shown in Equation 2.19) . For larger energy losses a single electron approach is to be taken as the probability of plural scattering is low and the intensity, $d\sigma/dE$, has a power law energy dependence,

$$\frac{d\sigma}{dE} \propto E^{-s} \qquad 2.12$$

Where s depends on the size of the collection aperture and should have a value of around 4 or 5 with small β[6].

When considering at the inner-shell electrons, which have large binding energies, it is found that the core-loss intensity is concentrated into smaller scattering angles than the background, therefore by using a smaller collection aperture, the energy to background ratio is improved.

2.4 Outer-Shell Excitation

The interactions of fast electrons with outer-shell electrons occur in the 0-100 eV range of the EELS spectrum, and apart from the elastically scattered electrons, they make the greatest contribution to the spectrum. A major feature in the spectrum is the plasmon peak. Plasmon excitation is an important process, but is not predicted by atomic models and is a consequence of collective electron oscillations in extended arrays of atoms. There are several types of plasmon excitation; the volume and surface plasmons are discussed below.

2.4.1 Volume plasmons

A volume plasmon occurs from the interaction of a fast electron with the outer shell electrons. This excitation creates a plasma resonance in the form of a longitudinal wave and the collective oscillation of the loosely bound valence or conduction electron 'gas' creates the plasmon at a characteristic angular frequency, ω_p. If there were no lattice damping this resonant motion would be self-sustaining. The following sections discuss the theories used to describe the plasmon effect, and the parameters that affect its energy.

2.4.1.1 The *Drude-Lorenz* Theory

The *Drude* theory treats the outer-shell electrons as a free-electron gas, or "jellium". It assumes that the interaction with the ion-core lattice is minor and may be incorporated by assigning an effective mass m_e^* to the electrons, and introducing a

damping constant Γ. If the electron gas with effective mass m_e^* is displaced by an amount **x** under the influence of an electric field **E**, it must satisfy the equation of motion,

$$m_e^* \frac{d^2\mathbf{x}}{dt^2} + m_e^* \Gamma \frac{d\mathbf{x}}{dt} = -e\mathbf{E} \qquad 2.13$$

When $E = E_0 \exp(-i\omega t)$, the differential equation has the solution,

$$\mathbf{x} = \left(\frac{e\mathbf{E}}{m_e^*}\right)\left(\frac{1}{(\omega^2 + i\Gamma\omega)}\right) \qquad 2.14$$

A polarization $\mathbf{P} = -en_f\boldsymbol{x} = \varepsilon_0 \chi_f \boldsymbol{E}$ arises due to the displacement, where χ_f is the electronic susceptibility and n_f the number of free electrons per unit volume.

Using the frequency dependent dielectric function for free electrons, $\varepsilon(\omega) = 1 + \chi_f$

with, $\chi_f = \dfrac{n_f e^2}{\varepsilon_0 m} \dfrac{1}{\omega^2 + i\Gamma\omega}$ 2.15

the dielectric function can be given by,

$$\varepsilon(\omega) = \varepsilon_1 + i\varepsilon_2 = 1 - \frac{\omega_p^2}{\omega^2 + \Gamma^2} + \frac{i\Gamma\omega_p^2}{\omega(\omega^2 + \Gamma^2)} \qquad 2.16$$

where,

$$\omega_p = \left[\frac{n_f e^2}{\varepsilon_0 m}\right]^{1/2} \qquad 2.17$$

The energy loss function may thus be defined as,

$$\mathrm{Im}\left[\frac{-1}{\varepsilon(\omega)}\right]=\frac{\varepsilon_2}{\varepsilon_1^2+\varepsilon_2^2}=\frac{\omega\Gamma\omega_p^2}{(\omega^2-\omega_p^2)^2+(\omega\Gamma)^2} \qquad 2.18$$

Pines[7] stated that the plasma oscillation of the outer-shell electrons at an angular frequency of ω_p is equivalent to creating a pseudoparticle of energy $E_p = \hbar\omega_p$ called a plasmon. By writing the energy loss function in terms of energy dependence, $Im[-1/\varepsilon(E)]$, where $E = \hbar\omega$ represents the energy loss, Equation 2.18 may be rewritten in the form,

$$\mathrm{Im}\left[\frac{-1}{\varepsilon(E)}\right]=\frac{E_p^2(E\hbar/\tau)}{(E^2-E_p^2)^2+(E\hbar/\tau)^2} \qquad 2.19$$

Where the relaxation time, $\tau = 1 / \Gamma$.

This is a simplified example based on the free-electron model, however it gives a good approximation to observed experimental data showing simple plasmon behaviour, such as metals. For insulators and semiconductors, where the outer-shell electrons have a minimum binding energy of the band gap, an additional force must be overcome before the collective oscillation may occur. Here, the valence electrons are to be considered as bound oscillators, n_b, with eigenfrequencies ω_b, damping constant Γ_b and electron susceptibility, χ_b.

The *Lorentz* theory takes into account these parameters and adds an extra term to the equation of motion,

$$m_e^*\left(\frac{d^2\mathbf{x}}{dt^2}+\Gamma\frac{d\mathbf{x}}{dt}+\omega_b^2\mathbf{x}\right)=-e\mathbf{E} \qquad 2.20$$

The solution of this equation gives the *Lorentz* model[8], or the modified free-electron model, where the dielectric response of bound charges is $\varepsilon(\omega) = 1 + \chi_b$, and,

$$\chi_b = \frac{n_b e^2}{\varepsilon_0 m} \frac{1}{(\omega_b^2 - \omega^2 - i\omega\Gamma_b)} \qquad 2.21$$

The *Drude-Lorentz* model can be achieved by combining the equations 2.15 and 2.21 to give,

$$\varepsilon(\omega) = 1 + \chi_f + \sum_j \chi_{b_j}$$

$$= 1 + \frac{e^2}{m\varepsilon_0} \sum_j \frac{n_j}{\omega_j^2 - \omega^2 - i\omega\Gamma_j} \qquad 2.22$$

Where n_j is the number density of electrons bound with resonance ω_j. This equation can be used to model the dielectric properties of any medium with a careful choice of oscillator energies and strengths. A limiting factor of these models is that they apply only to small scattering vectors **q**. The model had been extended to cover higher **q** by *Lindhard* in 1957 and has since been modified. A full explanation of this model can be found in *Egerton*[1].

2.4.1.2 Shift of Plasmon Peaks

The energy of the plasmon peak is affected by the energy of interband transitions, which occur at energy, E_i. By incorporating this into the Drude theory, using n_i as the total number of bound electrons which behave as simple-harmonic oscillators with characteristic angular frequency ω_i and damping constant Γ_i, the contribution to the susceptibility χ_i becomes,

$$\chi_i(\omega) = \left(\frac{n_i e^2}{\varepsilon_0 m}\right)^{1/2} \left(\omega_i^2 - \omega^2 + i\omega\Gamma_i\right)^{1/2} \qquad 2.23$$

And for small Γ, the new plasmon energy $E_p^{\,i}$ occurring at $\varepsilon_1(\omega)$=0, becomes,

$$E_p^i \cong E_p\left[1 + \chi(\omega_p)\right]^{-1/2} \qquad 2.24$$

where $E_p/\hbar=\omega_p$ if all electrons are free (n_i=0). The plasmon energy is likely to increase above the free-electron value if an interband transition occurs below the plasmon energy i.e. $\omega_i < \omega_p$, giving,

$$(E_p^i)^2 \cong E_p^2 + E_i^2 \qquad 2.25$$

For semiconductors, $E_i \cong E_g$, where E_g is the average band gap, thus,

$$(E_p^i)^2 \cong E_p^2 + E_g^2 \qquad 2.26$$

If the interband transition occurs above the plasmon energy, i.e. $\omega_i > \omega_p$ then the E_p will be lowered in energy.

2.4.2 Surface Plasmons

Unlike the volume plasmons, where a longitudinal wave propagates within a solid, when a longitudinal wave travels parallel to the surface it is known as a surface plasmon. These become more important the thinner the specimen is because the ratio of surface to volume area increases and can be approximated by the free-electron model, assuming negligible damping as,

$$E_s = \hbar\omega_s = \frac{\hbar\omega_p}{\sqrt{2}} = \frac{E_p}{\sqrt{2}} \qquad 2.27$$

Further discussion of surface plasmons and further modelling can be found in *Egerton*[1].

2.5 Inner-shell excitations

As inner-shell excitations are of relatively high energies, it is unlikely that plural scattering will occur, they may therefore be described using a single-atom model. The different cross-sections for the K-, L-, and M-shell ionisations, have been calculated by *Leapman et al*[9], using both the *Bethe* theory and *Hartree-Slater* central-field model[10,9]. Further edges, such as the $N_{6,7}$ and $O_{2,3}$ edges have been recorded for heavier elements such as uranium, but will not be discussed in this work[iii,11]. The K-shell edges have a saw-tooth shape and the sharp rise occurs at the ionisation threshold, the edge contains fine structure, which can be analysed to obtain more information on the material. The L-shell edges have several different shapes. In third period elements (Na to Cl) the $L_{2,3}$ edges have a more rounded profile with a delayed intensity maximum at around 10 – 20 eV above the ionisation threshold. This can be shown theoretically in the radial Schrödinger equation[12]. Fourth period elements, however, have quite distinctive $L_{2,3}$ edges with a sharp peak at the ionisation threshold. They exhibit white lines, or two separate peaks, which are due to the L_2 and L_3 spin orbit splitting, causing the L_2 binding energy to be

[iii] Further information on this may be found in the EELS atlas, (C.C. Ahn, O.L. Krivanek, EELS Atlas, Gatan Inc., (1983)

slightly higher than that of the L_3. The L_1 edge has been shown to possess the saw-tooth edge like the K-edge, but is of low intensity and may often be seen as a small step on the decreasing background of the $L_{2,3}$ edge.

The fifth-period elements have a prominent $M_{4,5}$ edge which has a delayed intensity maximum beyond the threshold as the 3d-4f transition which is optically preferred is suppressed by the centrifugal potential[13]. For the heavier sixth period elements, there is a high density of unfilled f-states, thus white line peaks occur at the threshold and the M_4 - M_5 splitting is apparent. The $M_{2,3}$ edges can be seen from the fourth period and tend to resemble the K-edges whilst the M_1 edges are very weak and not often observed.

2.6 Single scattering of electrons

There is a finite probability that a fast electron can be inelastically scattered more than once. This probability of n collisions through a sample of thickness t can be written following *Poisson's* statistics,

$$P_n = \frac{I_n}{I} = \left(\frac{1}{n!}\right)\left(\frac{t}{\lambda}\right)^n \exp\left(\frac{-t}{\lambda}\right) \qquad 2.28$$

Where λ is the mean free path between collisions. This again is an approximation, as assumptions have to be made such as; all scattering events are recorded and the area in which the spectrum is recorded is of uniform thickness. When plural scattering occurs, for example, a fast electron undergoes two inelastic scattering events, both of the plasmon energy, it will have lost an energy of $2\hbar\omega_p$. This energy

consists of two separate plasmons and there will be an event at an energy loss of $2\hbar\omega_p$, which represents double plasmon excitation and two single plasmon scattering events. Mixed plural scattering may also occur, for example, a fast electron may undergo a core-shell and outer-shell scattering event.

Multiple scattering occurs when samples reach a thickness greater that $t/\lambda = 10$, multiple outer- and inner-shell scattering events occur, resulting in a broad peak at an energy loss of a few hundred eV, this is known as a *Landau* distribution[14] and individual peaks are no longer visible. To obtain data that can be analysed, it is thus necessary that samples are thinner than $t/\lambda = 10$.

Before analysis is carried out on EELS spectra it is important that the plural scattering events are removed. For the low-loss region, a Fourier transform deconvolution is the standard technique to obtain the single scattered distribution (SSD) written,

$$J^1(E) \approx S(E) = \frac{2I_0 t}{\pi a_0 m_0 v^2} \mathrm{Im}\left[\frac{-1}{\varepsilon(E)}\right] \int_0^{\beta} \frac{\theta d\theta}{\theta^2 + \theta_E^2}$$

$$= \frac{I_0 t}{\pi a_0 m_0 v^2} \mathrm{Im}\left[\frac{-1}{\varepsilon(E)}\right] \ln\left[1 + \left(\frac{\beta}{\theta_E}\right)^2\right] \qquad 2.29$$

Where, I_0 is the zero-loss intensity, t is the specimen thickness, v the velocity of the incident electron, β the collection semi-angle, and $\theta_E = E/(\gamma m_0 v^2)$, the characteristic scattering angle. It is possible to use the raw data if the specimen is less than 10nm thick (where incident electrons have an energy of 100 keV), as the likelihood of plural scattering is low. However this data will contain appreciable surface loss

information, which when analysing the bulk material is not desirable. Work is being carried out to improve the SSD, as there is often a lot of noise associated with the first few eV. This is due to a poor fitting of the zero loss peak and can result in a *Kramers-Kronig* analysis which is of little use for the first 10 eV. This fitting is shown in Figure 2-4a for GaAs where it is clearly seen that the SSD has taken two different forms for the first few eV although the material is the same. In Figure 2-4b it can be seen how this fitting has affected the imaginary part (ε_2) of ε.

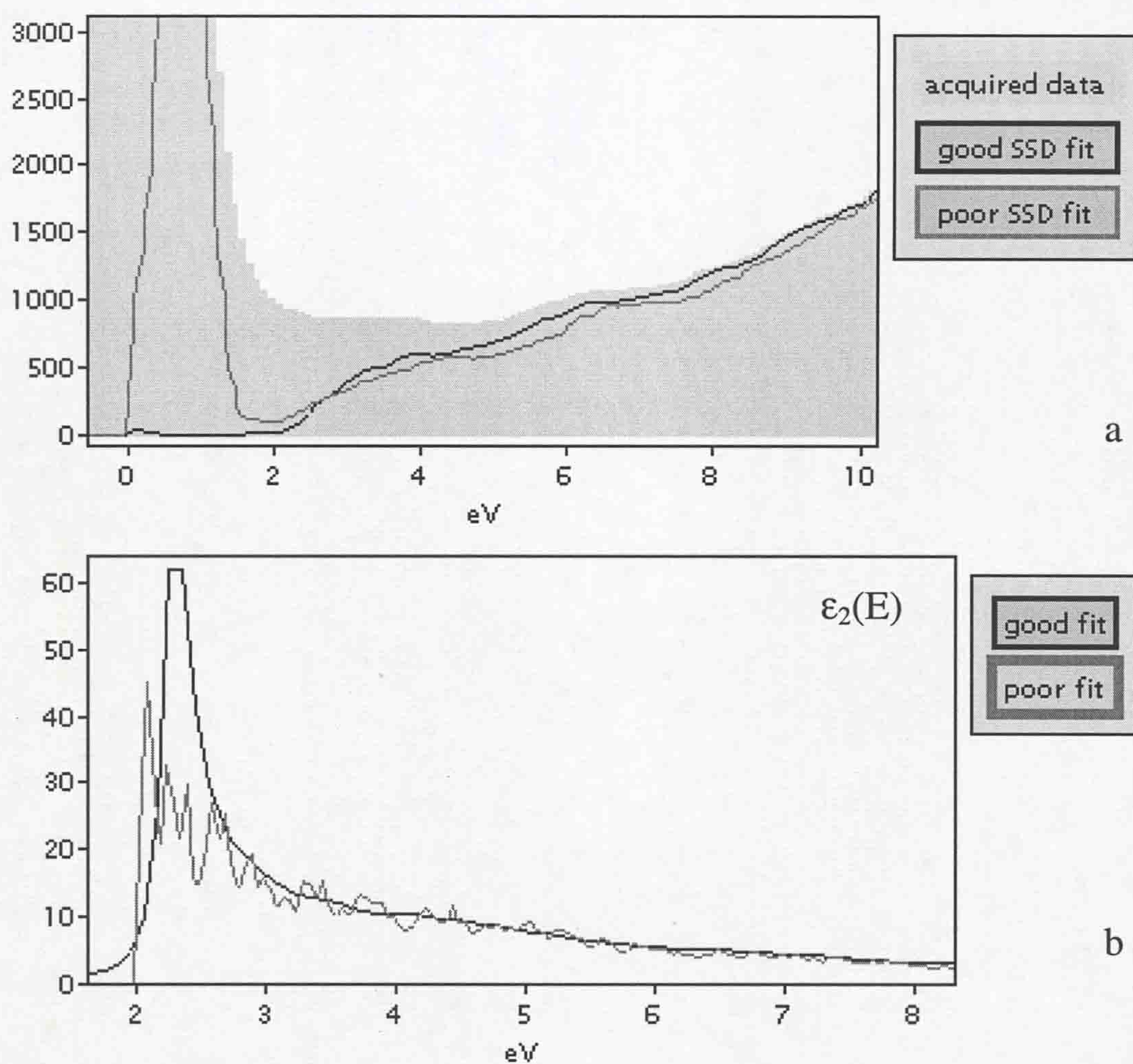

Figure 2-4. In a) the removal of the ZLP and plural scattering to obtain SSD shows the good fit (black line) where the intensity drops to zero below ~2 eV, and a poor fit (grey line) where part of the ZLP has been included in the SSD. The consequence of this poor fit can be seen in b), the imaginary part (ε_2) of the dielectric function (ε), where for the first 5 eV the data appears to be predominantly noise.

References

[1] R.F. Egerton, Electron Energy Loss Spectroscopy in the Electron Microscope, Plenum Press, New York (1986)

[2] N.F. Mott and H.S.W. Massey, The Theory of Atomic Collisions, Clarendon Press (1965)

[3] H. Bethe, Ann. Phys., **5**, 325 (1930)

[4] M. Inokuti, Rev. Mod. Phys., **43**, 297 (1971)

[5] R.H. Rithcie, Phys. Rev., **106**, 874 (1957)

[6] D.M. Mather, D.C. Joy, R.F. Egerton and P.Mochel, J. App. Phys., **50**, 5105 (1979)

[7] D.Pines, Elementary Excitations in Solids, Benjamin, New York (1963)

[8] A.V. Sokolov, Optical properties of metals, Blakie, London (1967)

[9] R.D. Leapman, P. Rez and D.F. Mayers, J. Chem. Phys., **72**, 1232 (1980)

[10] C.C. Ahn and P. Rez, Ultramicroscopy, **17**, 105 (1985)

[11] C.C. Ahn, O.L. Krivanek, EELS Atlas, Gatan Inc., (1983)

[12] F. Herman and S. Silkman, Atomic structure calculations, Prentice-Hall, Englewood Cliffs (1963)

[13] S.T. Manson and J.W. Cooper, Phys. Rev., **165**, 126 (1968)

[14] M.J. Whelan, J. Phys. C – Solid State Phys., **9**, L195 (1976)

Chapter 3

Experimental Techniques

Section		Page
3.1	CBE and MBE growth of samples	56
3.2	Sample preparation for transmission electron microscopy	58
3.3	Scanning Transmission Electron Microscopy (STEM)	63
3.4	Electron Energy Loss Spectroscopy (EELS)	65
3.5	Energy dispersive X-ray (EDX) analysis	81
3.6	Photoluminescence	82

3 Experimental Techniques

3.1 CBE and MBE growth of samples

The GaInNAs samples studied during this thesis are grown using two different systems. Those from the University of Liverpool are grown on a VG V80H chemical beam epitaxy (CBE) system, configured for all vapour sources. Triethylgallium (TEG) and trimethylindium (TMIn) are the group III precursors. Arsine (AsH_3) is pre-cracked to give an As_2 flux (H_2 is also produced) and an Oxford Applied HD25 RF atom source is used to inject an atomic nitrogen plasma flux into the chamber with flow rates between 1 and 5 sccm and forward power between 100 - 300W. Substrates are epi-ready (001) GaAs wafers. They are mounted on an indium free holding stage rotated at ~ 1 rpm to provide uniform deposition. Before layers are grown, the wafer is thermally cleaned in-situ under an arsenic flux to remove all surface oxides and establish an As-reconstructed surface and a GaAs buffer layer grown.

The GaInNAs samples from LAAS, France, are grown in a RIBER-32 MBE chamber using standard solid sources of Ga, In and As. These are heated in individual effusion cells to evaporate the elements, controlling the flow via temperature monitoring. Reactive nitrogen is supplied by an Oxford Applied Instruments HD25R RF atom source operated at 13.56 MHz. The reactive nitrogen is "leaked" into the growth chamber by a boron-nitride diffuser, containing 40 0.2 mm diameter holes. The nitrogen gas used in the RF sources is obtained from ultra

pure (6N) nitrogen gas (N_2), filtered using a particle filter and a heated getter filter (to stop H_2O, NO and other molecular impurities). Table 3-1 compares the typical growth parameters used for the growth of GaInNAs by Liverpool and LAAS.

Table 3-1. The typical growth parameters used for the different systems.

Sample origin	**Growth chamber**	**Temperature (GaAs)**	**Temperature (GaInNAs)**	**Nitrogen flow**	**RF Power**
Liverpool	CBE	600ºC	560ºC	1 - 5 sccm	100 - 300W
LAAS	MBE	580 - 600ºC	400 - 500ºC	0– 0.01 sccm	100 – 300W

The InAs QD structure was grown by Bookham Technology Inc using MOVPE in an Aixtron 2400 reactor on a 3" (001) GaAs substrate. The structure consists of one layer of InAs QDs. The InAs layer thickness was chosen to be above the critical thickness (>1.5ML) for the onset of the three-dimensional growth mode leading to the formation of the QDs. The growth temperature ranged from 500°C to 550°C.

The AlGaN/GaN sample was grown in a CVT MBE system. GaN was deposited on Si(111) substrates using the on-surface cracking of ammonia as the nitrogen source. The silicon wafers were initially cleaned, dipped in a buffered, HF solution, rinsed in de-ionized water, dried, and placed immediately into the MBE vacuum system. An AlN buffer layer 20–60nm thick was grown at a temperature of 530 °C. The resulting AlGaN and GaN layer thicknesses were approximately 600–850 nm as measured by a scanning transmission electron microscopy.

3.2 Sample preparation for transmission electron microscopy

Throughout the research, all the TEM samples were prepared as cross sections using two different methods; the first, a standard technique involving mechanical grinding and the second, a technique involving a dual beam FIB.

3.2.1 Mechanical grinding

Two pieces of wafer with a size of around 5mm x 3mm were glued together face to face with epoxy resin. Two pieces of silicon were then glued one on each side to strengthen the specimen, again with epoxy resin and the structure placed into a PTFE clamp to set. The specimen was mounted edge-on onto a grinding rig with superglue and mechanically ground to 4000 grit SiC paper to remove any roughness. The specimen was then soaked off in acetone, turned over, stuck down with superglue and ground and polished until the edges thinned away on 1200 to 4000 grit SiC, giving a thickness of <10 μm. Whilst the thinned specimen was still attached to the grinding stub, a 3.05mm copper TEM ring with a hole diameter of 2mm was fixed with epoxy, and any part of the sample lying outside the copper ring cut off.

The specimen was soaked off the stub in acetone and placed in a Gatan precision ion polishing system (PIPS), model 691. The PIPS uses a very high purity argon supply for the ion beams that were positioned one from above and one below the specimen at an angle of between 2 - 4°. During polishing, the specimen is rotating at ~ 3 revolutions per second and the operating energy of the ion beams was chosen to

be 5keV. Using this set-up, etching times of between 40 minutes to 2 hours produced large areas of TEM electron transparent material (20 – 150nm thick) for the GaAs based cross-sections, whilst minimising specimen damage and deposition of stray materials.

3.2.2 Dual Beam FIB

Dual beam focused ion beam (FIB) sample preparation is becoming popular as the technology becomes more accessible. It is the combination of a scanning electron microscope (SEM) and a focused ion beam, which allows the preparation of samples within the microscope. The samples are prepared using FIB milling which can produce thin sections at specific locations. The ion source produces Ga^+ ions from a gallium liquid metal and operates at energies of between 5 and 20 keV. The use of Ga as a source leads to the issue of whether this is a suitable process for materials containing Ga, including GaAs based semiconductors, as there may be the possibility of ion implantation during sample preparation. This would change the Ga composition in the specimen and give inaccurate compositional data on the material. It is also well known that crystalline material can become amorphous under the Ga flux. Samples of two of the laser structures prepared for this work were sent to two FIB companies so that they could prepare cross section samples using their dual beam FIB. The results of these are to be compared with the standard technique of mechanical grinding and PIPS.

Sample M1158, a GaInNAs QW laser structure grown by CBE at Liverpool, was sent to LEO where a cross section was prepared by FIB; another specimen was prepared conventionally at Liverpool so a comparison could be made.

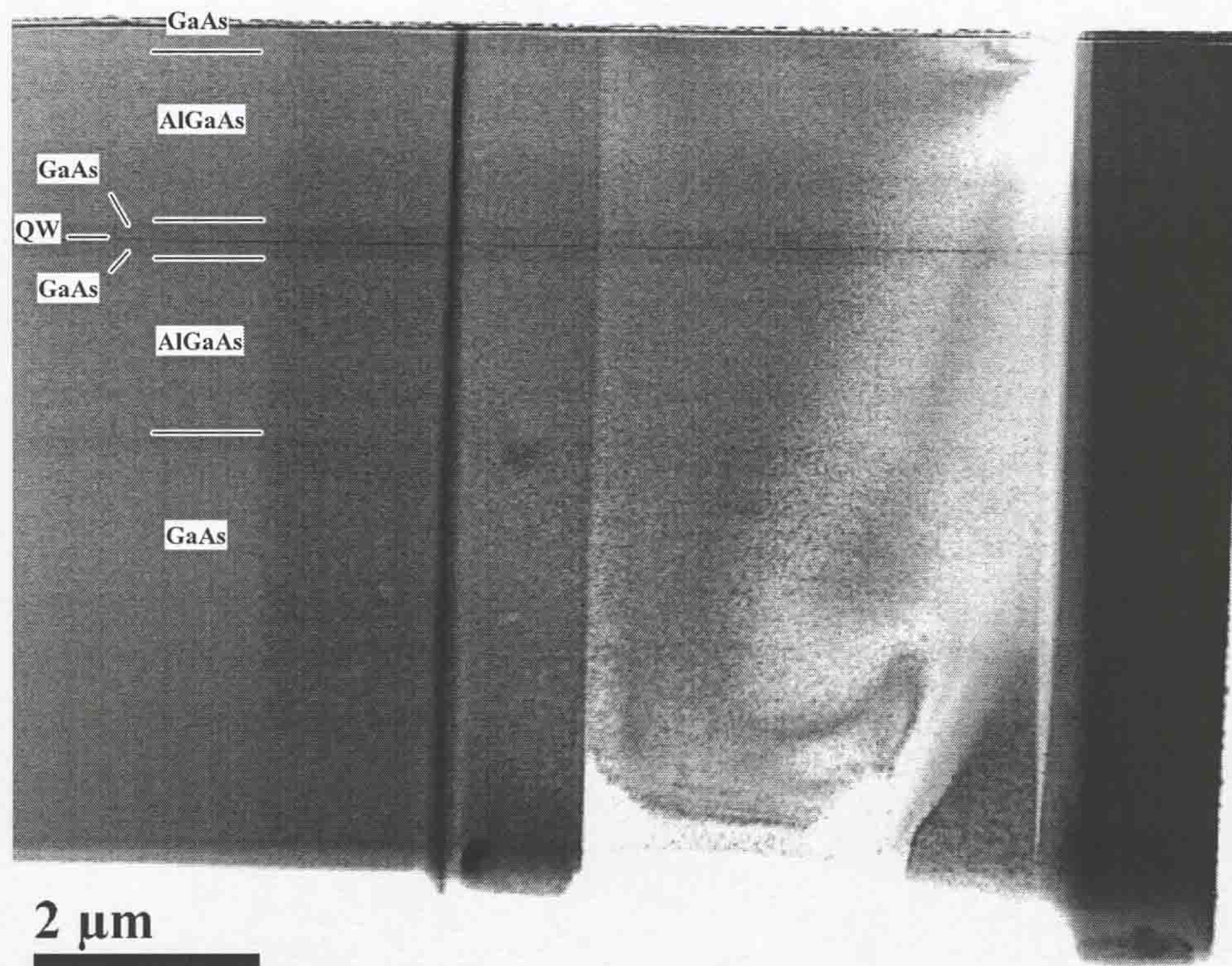

Figure 3-1 Shows the laser structure cross-section prepared by dual beam FIB at LEO, the different layers are indicated on the left hand side for clarity. The vertical lines that appear on the image are a printer artefact.

Figure 3-1 shows a low magnification bright field STEM image of the specimen prepared by LEO. The different layers of the laser structure can be seen across the image and on the left hand side the interfaces and layers are indicated by markers. Large areas of electron transparent material are visible with the thinner areas ~75nm in thickness towards the right hand side of the image, calculated via the EEL *Kramers-Kronig* analysis (described in more detail in subsection 3.4.5). The amount of electron transparent material is greater than that produced using conventional methods, however, it was found that the material had become amorphous during FIB preparation. A comparison of the bright field images from the sample prepared by FIB and ion beam thinning can be seen in Figure 3-2a. The structure of the specimen prepared by the conventional mechanical process and ion beam thinning

remains single crystal, and the sample is aligned on the –110 axis. The top layers (AlGaAs and GaAs) of the conventionally prepared sample were removed by the sample preparation. The conventionally prepared specimen clearly shows strain fields around the QW; this is not seen in the FIB specimen, as the microstructure has become amorphous.

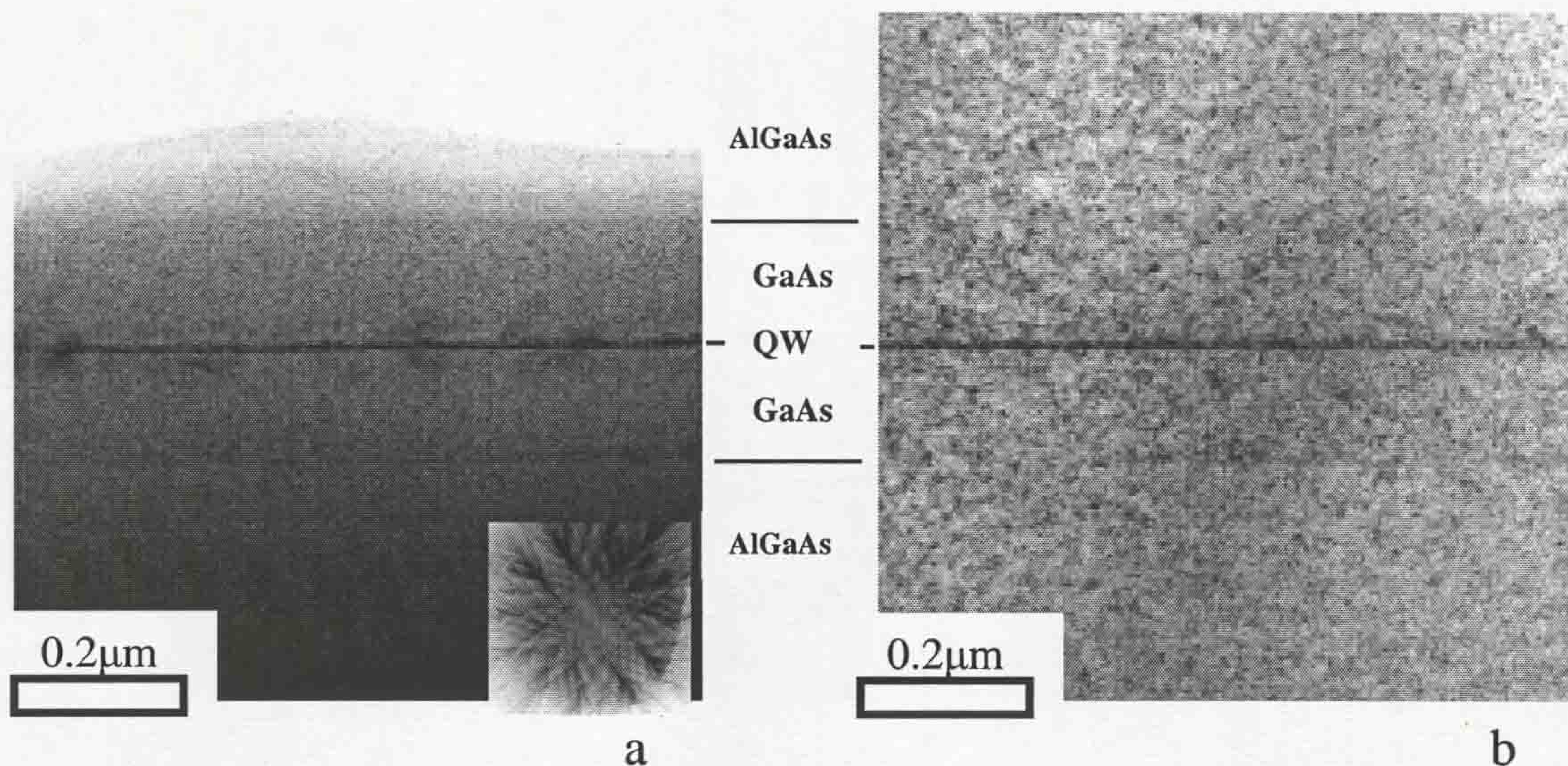

Figure 3-2 a) shows a bright field image of the specimen prepared by mechanical grinding with the aligned diffraction pattern on GaAs in the bottom right-hand corner, and b) prepared using the FIB method. Strain fields around the quantum well can only be seen in a).

Another GaInNAs QW laser structure, sample M1157, was sent to FEI, who also prepared several TEM specimens by dual beam FIB. The result can be seen in Figure 3-3. Again there is a large area of electron transparent material, and it has become amorphous during preparation. Moire fringes can be seen in the higher magnification image, indicating lots of small-disorientated crystals and rendering it unsuitable for detailed analysis. A further problem arising with samples prepared by dual beam FIB is that the thinned specimen is placed onto a holey carbon grid for support, and there may therefore be a layer of carbon underneath areas of the specimen to be analysed. This can be seen in Figure 3-3 in the low magnification

image, where the outline of a hole in the carbon grid can be seen through the centre of the thin area of the specimen. For low-loss EELS the presence of carbon is undesirable as it masks the Ga $M_{4,5}$ transition to be analysed and modifies the quantification of the material's properties when analysed using the *Kramers-Kronig* transformations.

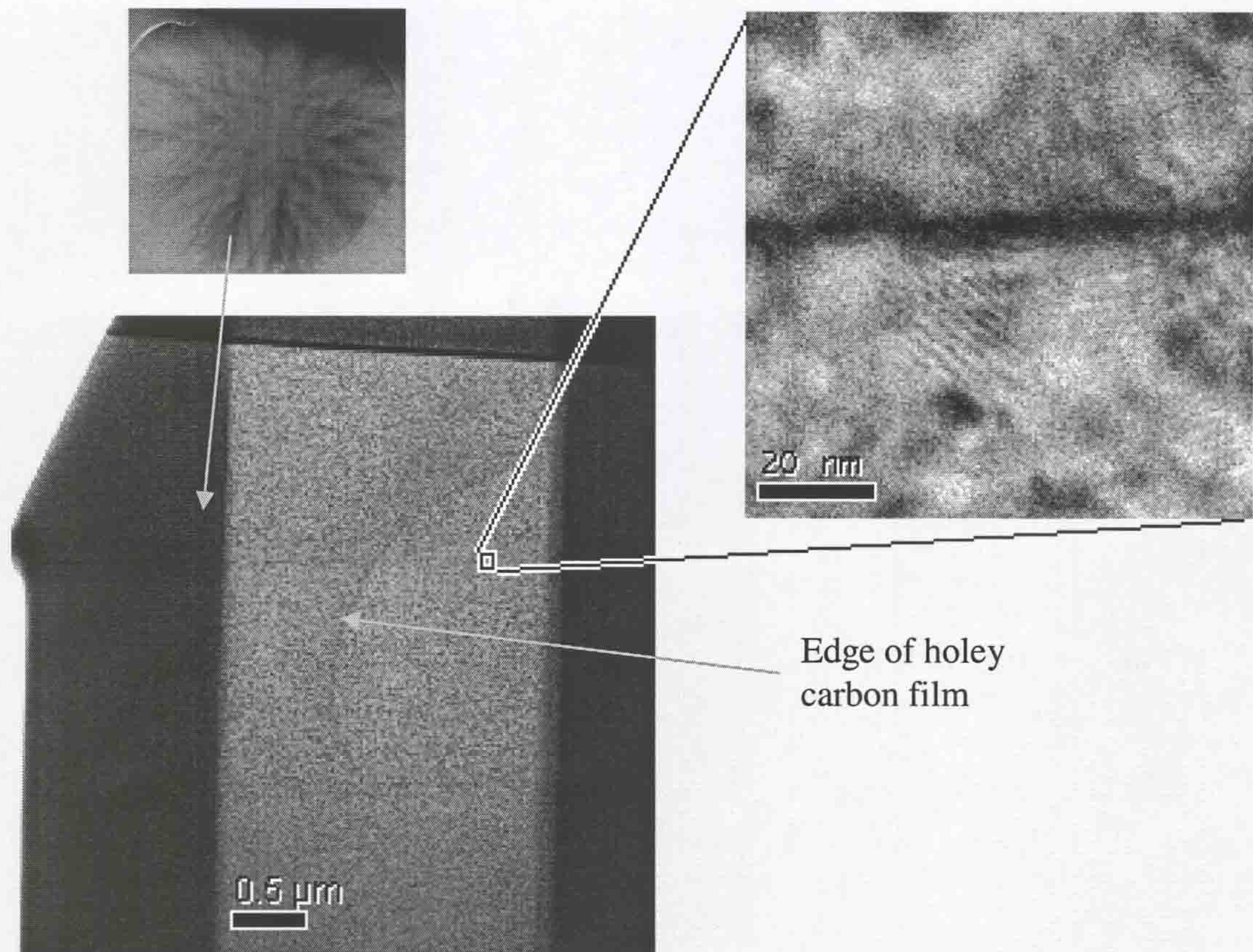

Figure 3-3. The specimen prepared by FEI shows a large area of electron transparent material in the low magnification bright field image. The insets show a higher magnification bright field image and the GaAs diffraction pattern from a thick area of the specimen. The holey carbon film can also be seen underneath the specimen.

At present, it is clear that for TEM specimens with minimum damage arising from preparation, conventional methods of mechanical grinding are superior to FIB. Further developments in dual beam FIB, such as different ion sources or lower operating energies, may in the future reduce sample damage enabling them to

produce good quality TEM specimens. However, in this present study all samples were prepared by conventional mechanical polishing and ion beam thinning.

3.3 Scanning Transmission Electron Microscopy (STEM)

The microscope used throughout the experimental work was the VG601UX scanning transmission electron microscope (STEM), which uses a 100keV convergent beam with a ~1nA current and 1nm "spot" at the specimen. The electron beam is rastered over the specimen area to create an image. The STEM differs from traditional TEM in several ways. The TEM uses a 100-200keV electron beam which is parallel (or slightly convergent) to the column producing uniform electron-beam intensity over the sample area to be imaged. Unlike the STEM, the TEM requires post-objective lenses. A further important difference is that in the STEM the electron source is situated at the bottom of the microscope column, instead of the top for a conventional TEM, leading to greater vibrational stability. The electron beam travels up the microscope through the lenses, apertures and specimen to the top of the column where the bright field and EELS detectors are to be found. Figure 3-4 shows a schematic of a STEM and a TEM set up for scanning mode.

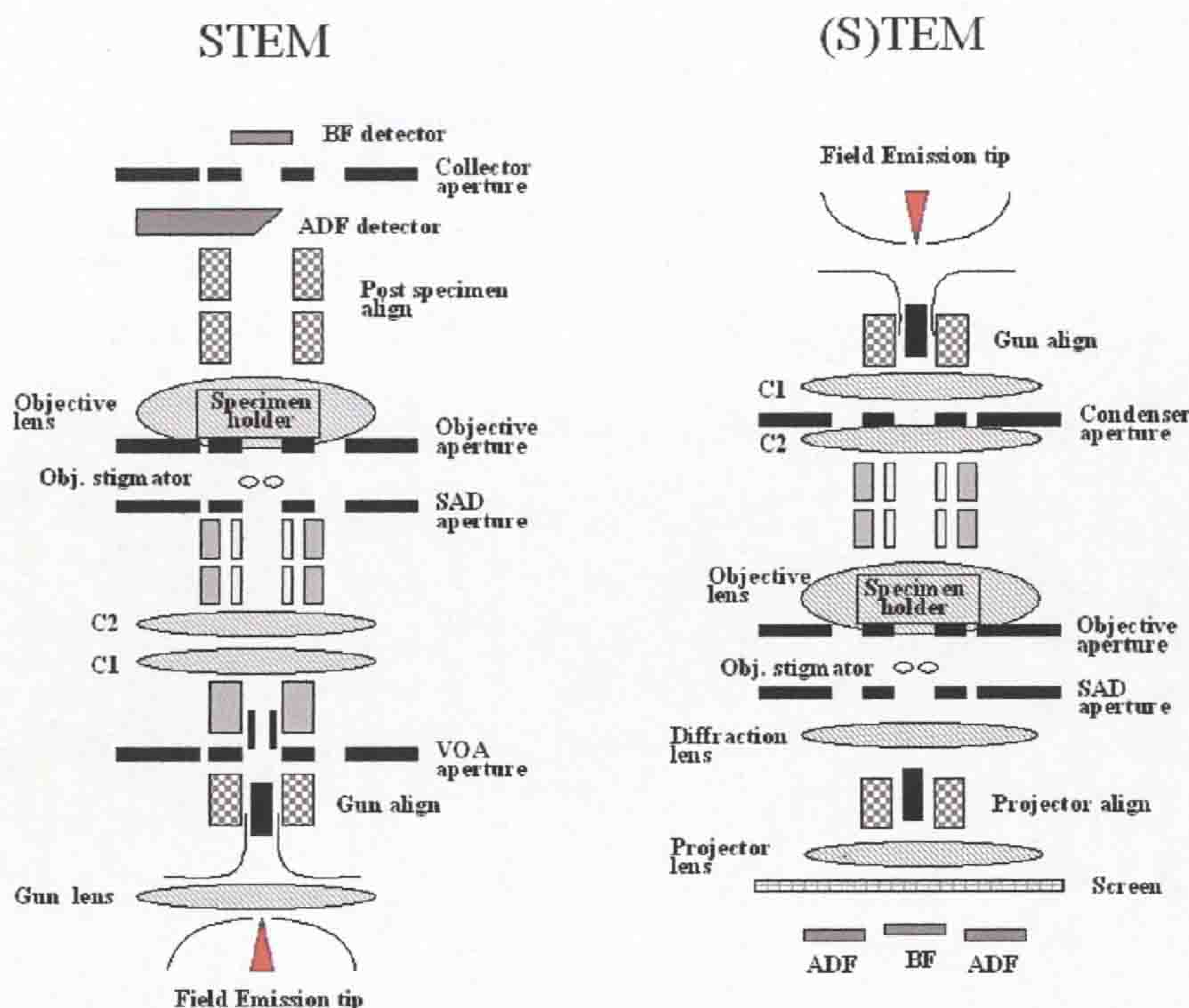

Figure 3-4. A schematic showing the difference between a STEM and a TEM set up for scanning mode, the red arrow indicates the direction of the electron beam.

In the VG 601 UX, the electron source is a cold field emission gun (FEG). The 'triode' FEG consists of a metal surface with a radius of curvature of ~50nm. This can give an effective source size of 5nm diameter and a probe size of 0.5nm after demagnification through the column. Typically, the source is made from a single tungsten crystal, which has been electrolytically sharpened. Compared to the traditional tungsten hairpin filament, this provides an increase in brightness of up to 1000 times for a given accelerating voltage.

For chemical analysis to be carried out, or for the electron beam to be focused on to a small area of specimen for a period of time, both a clean specimen and high vacuum are essential to avoid contamination. The tip also needs very good stability

so that the work function does not change. It is for this reason that the VG 601 UX STEM employs an ultra high vacuum (UHV) in the gun and a high vacuum in the column; it is also necessary to 'clean' the tip regularly during a session, as FEG tips degrade over a period of ~ 2 hours. A full discussion on STEM optics and imaging can be found in *Keyse*[1].

3.4 Electron Energy Loss Spectroscopy (EELS)

Throughout this thesis, the Gatan Enfina™ system was used for analysing the EELS data. This is a parallel EELS detector, with an EELS spectrometer interfaced onto the top of the STEM. It uses a thermostatically cooled scintillator-charge coupled device (CCD) based detector, which is 30 times more sensitive than the typical photo diode array (PDA) giving improved resolution measured as point spread function (PSF), greater sensitivity and faster acquisition times. Figure 3-5 shows the path of the electrons through the spectrometer. The spectrometer is a magnetic prism (or sector), which bends the path of the electrons. The more energy the electrons have lost, the greater their angular deflection as they pass through the spectrometer. This deflection is measured at the focal point and a spectrum is produced of intensity versus energy loss of the electrons. Factors such as acquisition time, energy dispersion and collector apertures must be selected to optimise the information collected, these will be discussed in the following sections. The theory behind electron sample interactions is covered in detail in Chapter 2.

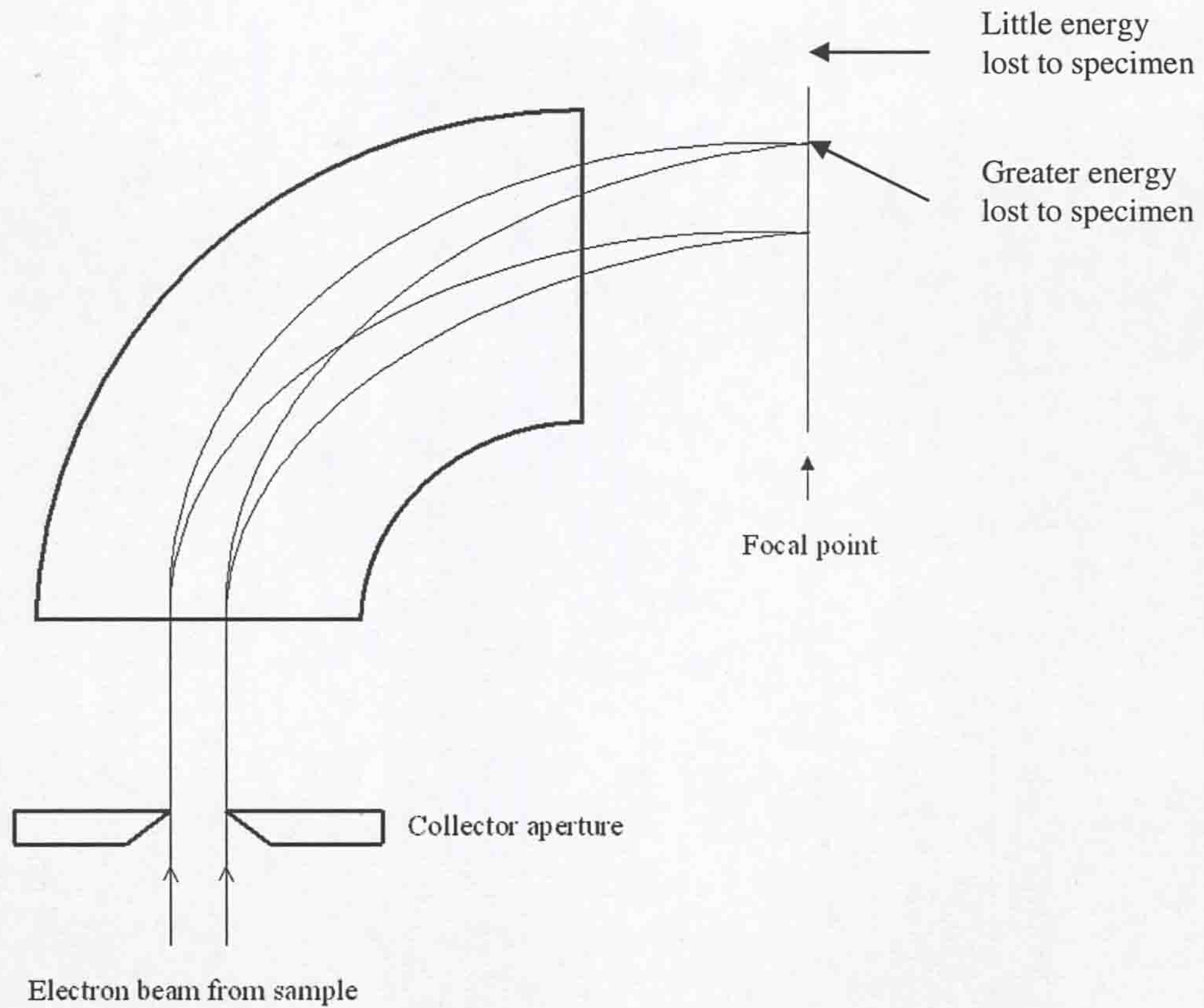

Figure 3-5. A schematic diagram of the ray paths through a magnetic prism spectrometer.

There are many different ways in which an EELS spectrum may be examined. Each obtains different information on the material being studied, from elemental analysis to electronic structure. Throughout this thesis, several methods have been used, and new ones developed to extract further information from the EELS data. These methods exploit the ability of the Gatan Digital Micrograph package installed on the STEM to apply techniques previously used just for single spectra to produce entire EELS spectrum images. These techniques are described below for single spectra, but all may be applied to mapped areas as well.

3.4.1 Introduction to core-loss analysis

EELS is often used to obtain quantitative information on the lighter elements, which cannot normally be observed through techniques such as EDX. On interaction with the incident electrons, elements emit characteristic X-rays, which in the case of the lighter elements are generally of too low an energy to be detected by conventional EDX methods. EELS, however, measures the energy lost by the incident electrons on interaction with the specimen. Generally, in EELS, the lower the energy loss, the greater the intensity observed in the spectrum[2]. It is thus preferable to study the lighter elements with core loss measurements acquired with EELS, as the incident electrons generally lose a smaller amount of energy on interaction with lighter elements than with the heavier elements. The different types of edges that occur have been discussed in section 2.5. The major core-loss edges in a GaInNAs / GaAs material occur from the transitions of the Ga $M_{2,3}$ (103 eV), In $N_{2,3}$ (77 eV), N K (400 eV), As $M_{2,3}$ (144 eV) and As $M_{4,5}$ (41 eV) shells to the conduction band, all with energies between 40 - ~400 eV. Over the years, these edges have been studied in detail; their energies and shapes can be found in standard EELS texts[3,4]. However, there are other transitions that exist, such as those due to the $M_{4,5}$ and $N_{4,5}$ states for Ga and In respectively found on the far edge of the GaInNAs plasmon peak and for N the L_1 transition near the centre of the plasmon peak. There is some debate as to whether these transitions are core-loss or not, and they have been called valence-band or semi-core states. Although they are not part of the outer shell, the Ga 3d and In 4d electrons (equivalent to the $M_{4,5}$ and $N_{4,5}$ states) are shallow, thus are very close to the Ga $4s^2$ and $4p^1$, and In $5s^2$ and $5p^1$ electrons in energy. It has been shown that these d-electrons hybridise[5,6] with the outer-shell electrons; therefore not allowing them to be treated as "frozen-core" electrons. As these

transitions appear in the low-loss region of the EELS spectrum, they will be discussed as part of the low loss data.

The quantification of core-loss edges to give compositional information is a well-established routine for the K- and L-edges, for which programmes have been written to calculate their cross sections. These programmes can be found on most EELS analysis packages[i], and will calculate the composition of a specimen with multiple elements. This procedure is not as well developed for the M-edges, as their shape is more complex and is not included in the Digital Micrograph package, although the facility to add in a script is available.

3.4.2 Core-loss analysis in the STEM

The set up of the microscope and detector for acquisition of core-loss EELS data is discussed here. The microscope must be well aligned with the objective aperture in. The EELS detector is at the top of the column and there is a choice of two spectrometer entrance (Gatan) apertures through which the beam may pass of 2 and 4mm. When this aperture is inserted, it is no longer possible to obtain a bright field image as they both use the same focal planes. It is, however, possible to acquire the dark field image, thus most of the sample manipulation is carried out using the dark field image during EELS acquisition. Another aperture, which is above the dark field plane, but below the Gatan aperture, is the collector aperture. This can be used to select the acceptance angle within which scattered electrons will be allowed through and knowledge of its size is important when undertaking further

[i] The Gatan Enfina Spectrum Imaging software has an extensive list of core-loss elemental edges in their quantification routine.

calculations after the EELS data has been collected, such as *Kramers-Kronig* analysis. The VG 601 UX STEM used has collector aperture sizes equivalent to acceptance angles of 0.34, 1.34, 3.4 and 6.8 mrad.

For core loss analysis, the probability that an incoming electron loses energy to a core-shell electron is much smaller than to an outer-shell electron, thus the intensity of the core-loss electrons in the specimen is relatively weak. For that reason it is necessary to let as many electrons pass through to the detector as possible. To do this a large spectrometer entrance aperture is used in combination with a large collector aperture. Next, the number of channels per eV of energy loss in the EEL spectrometer must be chosen. Again, by choosing a higher number of eV per channel both the intensity of the spectrum and the energy range to be acquired will be increased, however, at the expense of energy resolution. The distribution of eV per channel is dependent on the energy range to be studied and the thickness of the sample, as the thicker the sample, the weaker the signal. A further variable to consider is the acquisition time; for core-loss this can typically range from between 5 – 50 seconds, increasing with increasing energy-loss.

3.4.3 Introduction to low-loss analysis

The information contained in the low-loss region of an energy loss spectrum has not been fully exploited, with the preference being to concentrate on the core-loss. The usefulness of the low-loss information has previously been limited by the energy resolution of the EEL instrumentation and the complex computer programmes needed to analyse it, as described in subsection 1.5.2. However, it is the region of the spectrum that can in principle have the greatest energy resolution with the

highest acquisition rates, as described below. The different ways in which the low-loss data has been analysed during this research is also described in the following sections.

3.4.4 Low-loss analysis

As with the core-loss, the microscope must be well aligned, with the objective aperture in. However, as the intensity of electrons in the low-loss region is very high, the set up of the apertures must be such that the zero loss peak does not saturate. With this in mind, generally smaller collector and Gatan apertures are used; this gives an electron beam with very little deviation from the central axis i.e. θ is very small. The energy resolution is also maximised for low-loss, with typically 0.05 – 0.1 eV per channel used for analysis. A further advantage of the low-loss is the speed in which data may be acquired. As the zero loss peak can saturate very easily, especially if the specimen is relatively thin, the length of acquisition must be low, generally in the range of 0.05 – 0.5 second per spectrum. It may be the case that information at energies higher than the zero loss peak has poor statistics, in these circumstances, several spectra can be acquired at the same point and summed together. This will improve the statistics of the data without the zero loss peak becoming saturated.

3.4.4.1 Aligning the spectrum and removal of plural scattering

There is usually a small amount of drift in the energy spectrum over time. This means that if spectra are being acquired sequentially over a session, there is a chance that the spectra acquired later in the session will have shifted in energy relative to

those acquired earlier on. Due to this drift, the zero loss peak will no longer be at 0 eV in all cases, and all the other spectral information will also be shifted by the same amount. If there are several spectra to be summed it is essential that they are all aligned to a common zero. When dealing with the low loss this can be achieved by measuring the position of the zero loss peak and shifting it to zero using two scripts called *measure chromaticity* and *correct chromaticity* (© Gatan Inc) respectively.

The EEL spectrum "as acquired" may contain plural scattering artefacts as described in section 2.6. This is often observed for the plasmon peak, as a second, less intense feature present at double the energy of the plasmon. In order that the low-loss spectra can be further analysed, both effects of the plural scattering and the zero loss peak must be removed. Fourier-log deconvolution is used when analysing low-loss data and this is applied to obtain the single scattered distribution (SSD) (see Equation 2.29). It should be noted that the specimen must have a fairly uniform thickness for deconvolution to succeed.

The Gatan Digital Micrograph software has several different fitting routines to obtain the best fit possible to the zero loss peak, and through experimental analysis it was found the setting that best fits the zero loss peaks obtained from the STEM is the *Gaussian and Lorentzian* model. It is essential that a good fit is achieved otherwise further spectral processing will be hindered due to added statistical noise or poor ZLP fits leaving small peaks. An example of an "as-acquired" spectrum and the SSD spectrum are shown in Figure 3-6.

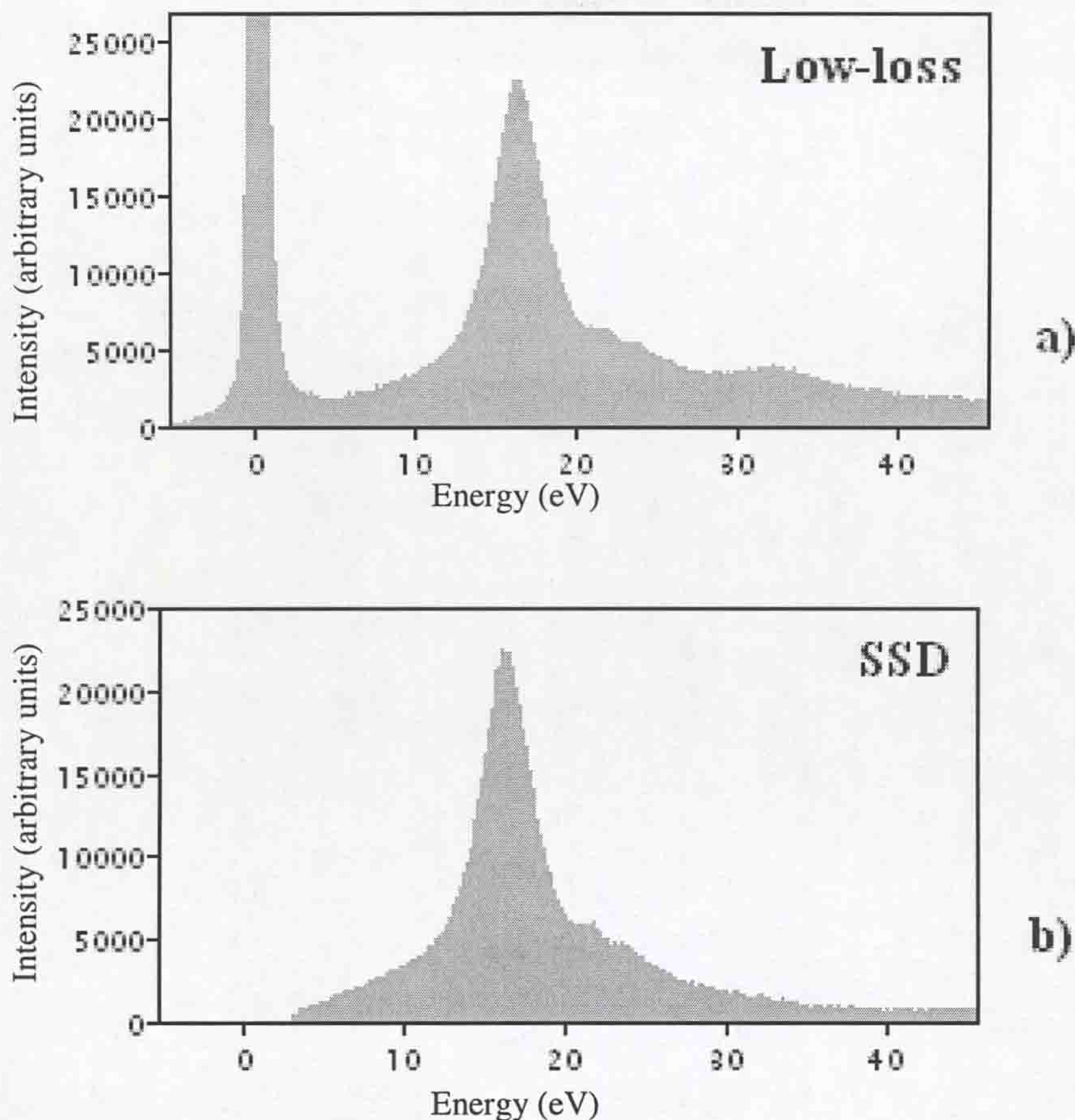

Figure 3-6. a) The low-loss spectrum and b) the SSD after the Fourrier-log deconvolution using the *Gaussian and Lorentzian* model to remove the zero loss peak. This is a good example of the SSD and shows how the plural scattering of the plasmon peak at ~32eV has been removed. It also shows the intensity drops off as the energy loss decreases to zero.

3.4.4.2 Determination of the plasmon energy

The plasmon frequency may be determined using two techniques. The first method is obtained using a procedure called *non-linear least squares* (NLLS) fitting in the Gatan software. This procedure allows single or multiple Gaussian models to be fit to the spectrum. To determine the plasmon frequency, a single Gaussian is fit to the plasmon peak from the single scattering distribution, as seen in Figure 3-7. This will in turn determine the full width half maximum (FWHM), the energy of the centre of

the Gaussian and the intensity of the Gaussian. The plasmon frequency can be determined using the equation,

$$\omega_p = \frac{E_p e}{\hbar} \qquad 3.1$$

where E_p (in electron-volts) is the energy at the centre of the Gaussian, and is multiplied by $e/\hbar = 1.51927\text{x}10^{15}$ $CJ^{-1}s^{-1}$ to give ω_p in the region of 10^{16} s^{-1}.

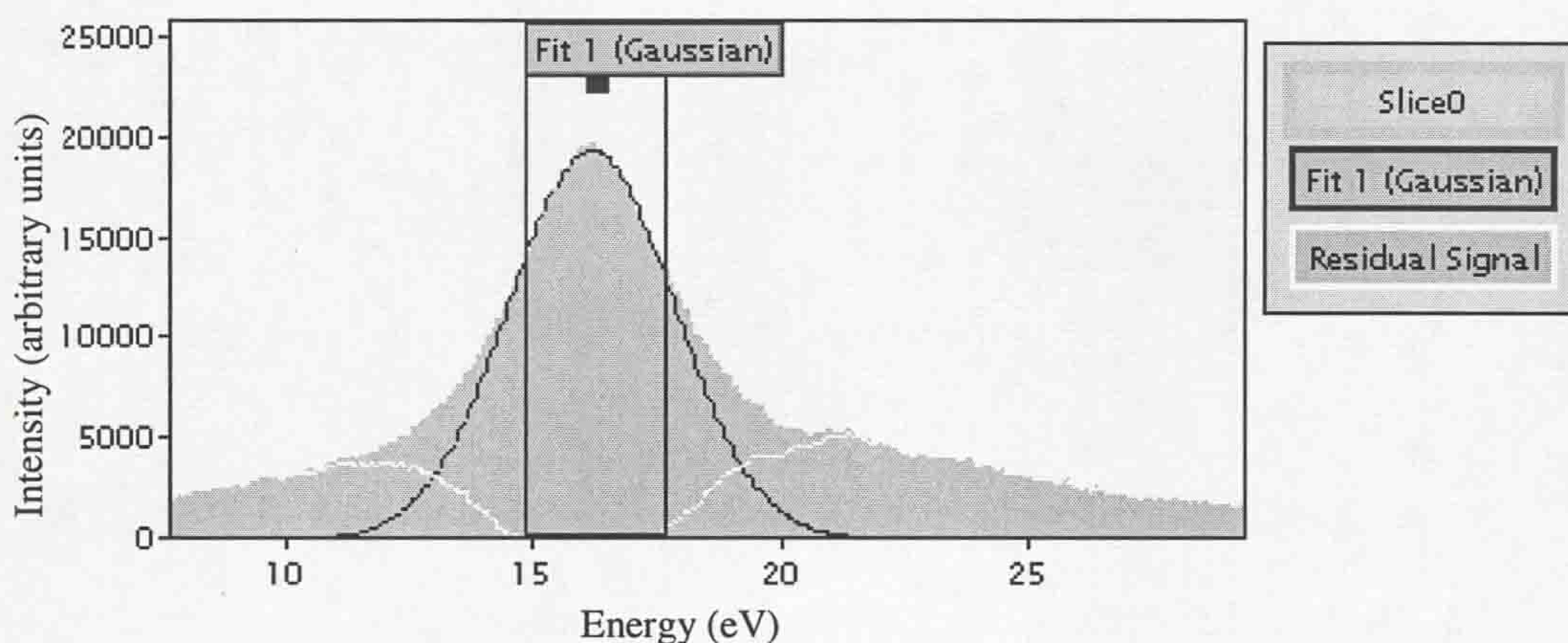

Figure 3-7. The Gaussian fit is shown by the curve superimposed onto the spectrum.

The second method of obtaining the plasmon frequency uses the real part of the dielectric function, ε_1. The plasmon energy is determined by the energy at which ε_1 passes through a value of zero on the ε_1 versus energy spectrum. This will be further discussed in Section 3.4.5 as part of the *Kramers-Kronig* analysis; the two methods will be compared and discussed. The effect of thickness of the specimen on the plasmon energy will also be investigated.

3.4.5 *Kramers-Kronig* Analysis

Kramers-Kronig (KK) analysis allows the energy dependence of the real and imaginary parts of the dielectric function to be calculated from single scattered distribution energy loss data. As the dielectric response function is causal, the function *Re[1/ε(E)]* can be derived from *Im[-1/ε(E)]* in the SSD (see Equation 2.29) using[7],

$$\mathrm{Re}\left[\frac{1}{\varepsilon(E)}\right]=1-\frac{2}{\pi}P\int_0^{\infty}\mathrm{Im}\left[\frac{-1}{\varepsilon(E')}\right]\frac{E'dE'}{E'^2-E^2} \qquad 3.2$$

where *P* denotes the Cauchy principle part of the integral. There are several ways of achieving the KK transformation, but the fastest (which is used by the Gatan software), is the *Johnson* method. This method, using a fast-Fourier algorithm; takes the sine transformation of *Im[-1/ε(E)]*, followed by an inverse cosine transformation. Details of the computer programme can be found in Appendix B5 of *Egerton*[8]. Several parameters must be entered before the calculations can take place: the incident beam energy, E_0; the convergence semi-angle (defined by the objective aperture) α, 14.2 mrad; the collection semi-angle (defined by the collector aperture), β; and the refractive index (for visible light), *n*. These calculations assume that the beam is perpendicular to the specimen, and that the specimen is also clean and free from oxide.

After computation of the real and imaginary parts of the dielectric function, the functions $\varepsilon_1(E)$ and $\varepsilon_2(E)$ and other functions which come from the KK analysis in the Gatan Digital Micrograph software can be obtained from,

$$\varepsilon(E) = \varepsilon_1(E) + i\varepsilon_2(E) = \frac{\mathrm{Re}[1/\varepsilon(E)] + i\,\mathrm{Im}[-1/\varepsilon(E)]}{\{\mathrm{Re}[1/\varepsilon(E)]\}^2 + \{\mathrm{Im}[-1/\varepsilon(E)]\}^2} \qquad 3.3$$

3.4.5.1 Epsilon 1 (ε_1)

ε_1, is derived from Equation 3.3 above to give[9],

$$\varepsilon_1(E) = \frac{1}{\pi} P \int_{-\infty}^{\infty} \frac{\varepsilon_2(E')}{E' - E} dE' \qquad 3.4$$

ε_1 is the real part of the dielectric function and represents the dispersive element of the transitions. In an electron gas, the condition for a plasma oscillation is that both ε_1 and ε_2 must equal zero and marks the transition from the reflecting to transmission region. When the plasma resonance occurs within a solid it is damped and the condition described can no longer exist, factors that could increase the damping are crystal boundaries and strain[10]. As long as $\varepsilon_2 << 1$, the condition $\varepsilon_1=0$ can still be used to determine the plasmon energy, however it will generally be lower than the real value. Semiconductor materials exhibit another point at which $\varepsilon_1(E)=0$ (on a negative gradient) at lower energies, this occurs at an energy where $\varepsilon_2(E)$ has a maximum due to the energy gap between the valence and conduction band at the *X* point in the Brillouin zone.

Figure 3-8 shows a spectrum of ε_1. The red (solid) arrow indicates $\varepsilon_1(E) = 0$, the transition from the reflection to transmission region, or the plasmon energy and the black (dashed) arrow indicates the energy gap at the *X* point of the Brillouin zone. Gatan were asked to write a script to determine the point at which ε_1 crosses through 0, providing a measurement of the plasmon energy. The script can be found in Appendix B1; this could then be compared with the plasmon energy determined using the process described in Section 3.4.4.2.

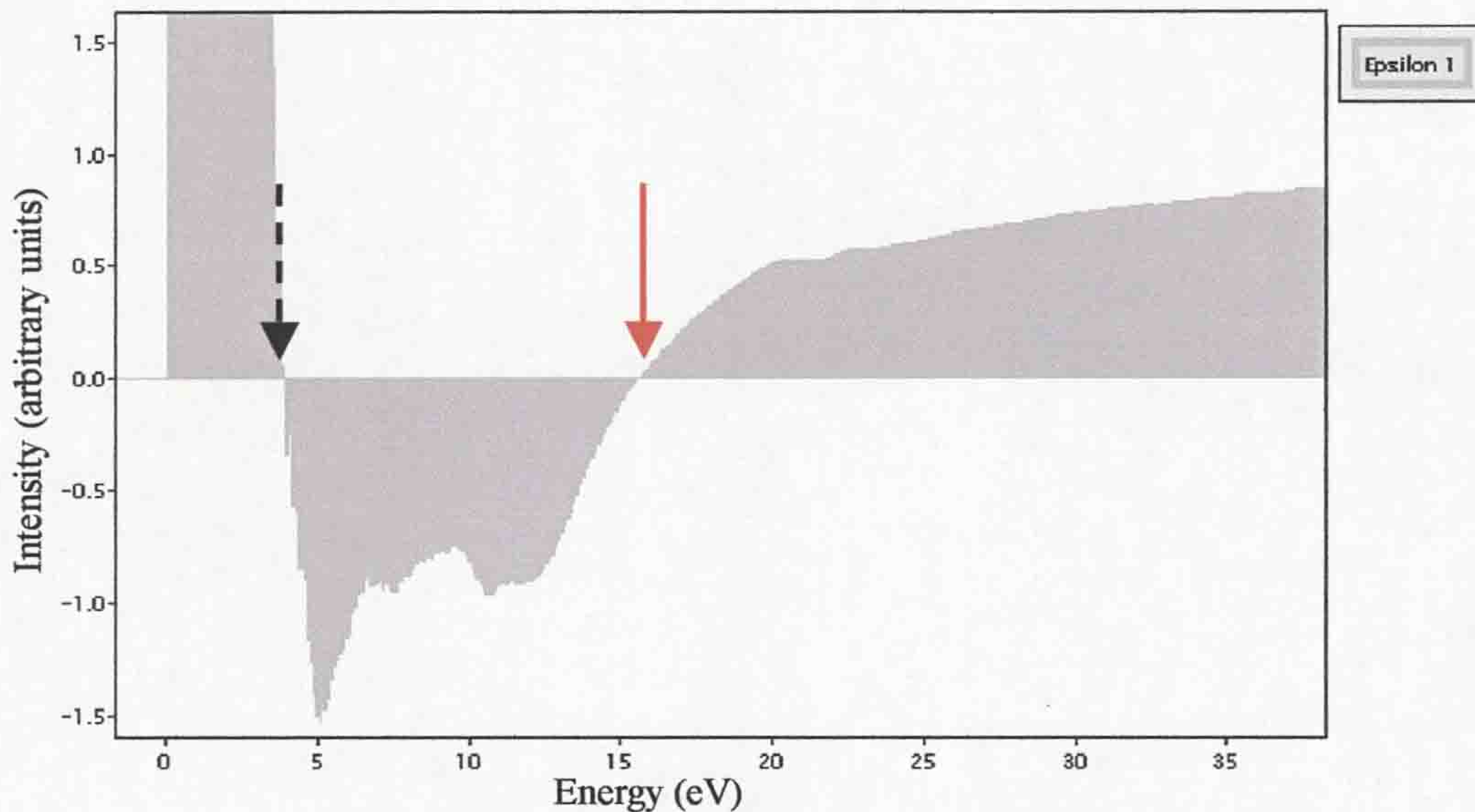

Figure 3-8. The spectrum shows how the real part of the dielectric function, ε_1, changes with energy loss for GaAs. The red (solid) arrow marks the transition from the reflection to the transmitting region, often used to determine the plasmon energy.

3.4.5.2 Epsilon 2 (ε_2)

ε_2 is the imaginary part of the dielectric function and represents the absorption of energy by optical transitions. It can be calculated by[9],

$$\varepsilon_2(E) = -\frac{1}{\pi} P \int_{-\infty}^{\infty} \frac{\varepsilon_1(E')}{E'-E} dE' \qquad 3.5$$

ε_2 contains information about the optical absorption of the material and has previously been used[11] to obtain information about the band-gap region and other similar valence band transitions in the first 10 eV. However, further information on the absorption associated with the Ga 3d and In 4d transitions will be present in the 18 – 25 eV range. It was an aim of this present research that, by using this absorption information, elemental composition could be determined and high energy- and spatial-resolution maps of elemental composition could be produced. Figure 3-9 shows how in ε_2 the background signal is removed. An energy slice is then selected for the integration of the signal to obtain a measure of the intensity of the ε_2 signal associated with the Ga 3d and In 4d transitions. For the Ga 3d transition this is chosen to be 20 – 24.5 eV and for the In 4d transition 18.0 – 19.6 eV as they cover the main peaks without overlapping with each other. The window to be integrated is then applied to each spectrum in the SI to give a spatially resolved elemental map. There is a possibility that the tail of the In 4d signal will continue into the Ga 3d signal, effecting the quantification process. To overcome this, the In 4d signal could be removed from the spectrum before quantification of the Ga 3d, however, no attempt has been made to do this during this work.

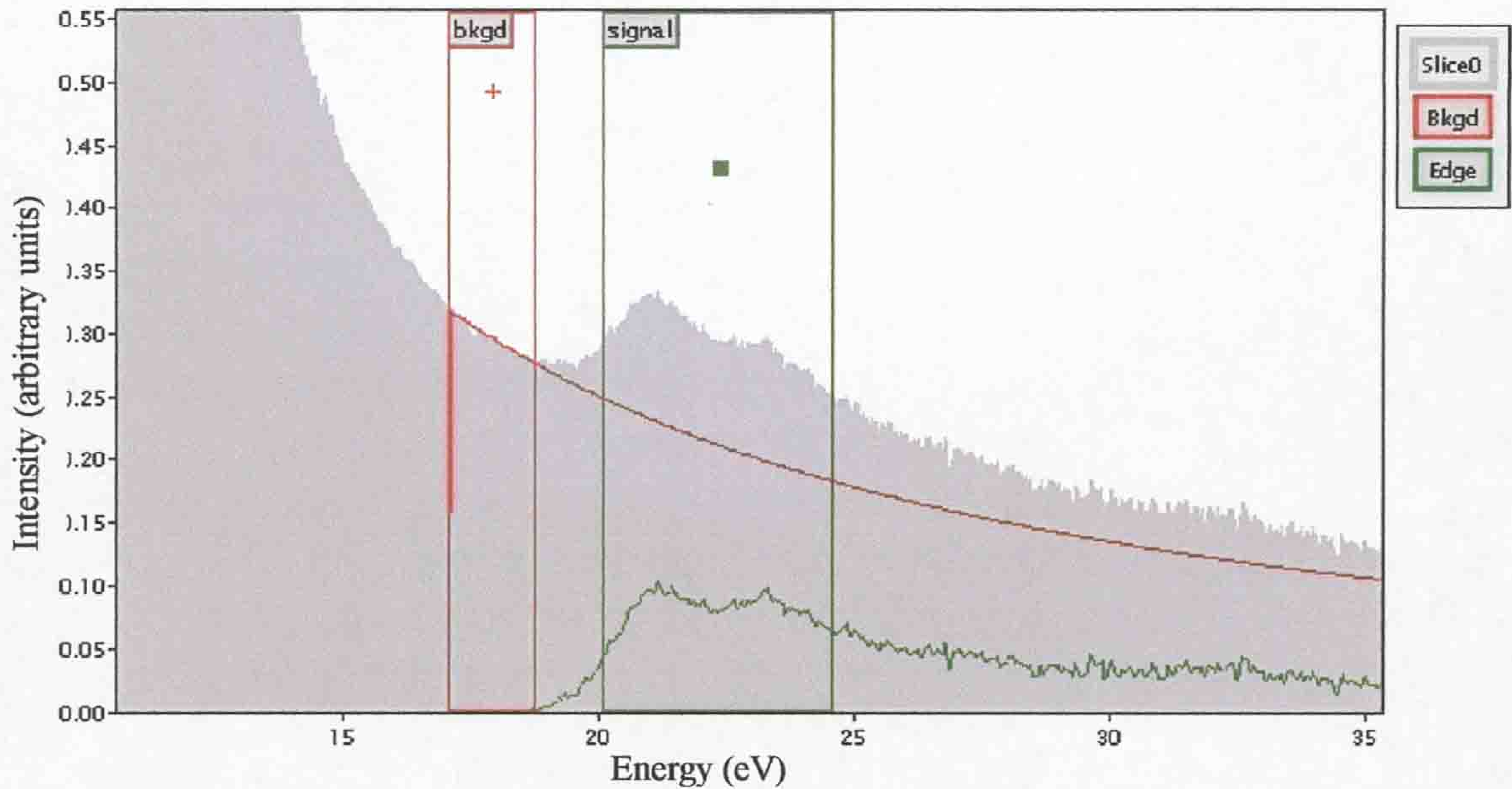

Figure 3-9. A selected area from ε_2 shows the background removal and area to be integrated to calculate the intensity of the Ga 3d transition. The integrated area for the Ga 3d transition is 20 – 24.5 eV and 18 – 19.6 eV for the In 4d transition.

The same transitions can be seen in the SSD spectrum, and using the same method of background removal and signal selection, the accuracy and resolution of the two techniques will be compared.

3.4.5.3 Effective number of electrons

The effective number of electrons, n_{eff} is calculated from the imaginary part of the dielectric function and its chosen output is in units of electrons per nm^3 (e$^-$/nm^3) using the equation[12],

$$n_{eff}(\varepsilon_2) = \frac{2\varepsilon_0 m_0}{\pi\hbar^2 e^2}\int_0^\infty E'\varepsilon_2(E')dE' \qquad 3.6$$

where ε_0 is the permittivity of free space, m_0 is the electron mass at rest, $\hbar$ is Plank's constant divided by 2π, and e is the electronic charge. n_{eff} shows graphically how

many electrons at a given energy have been promoted to the conduction band and using a material's density, the number of electrons per atom can be calculated. An example of this is shown in Figure 3-10, a spectrum of n_{eff} versus energy for GaAs. It can be seen that gradient changes at ~15eV, this is the point at which all the valence electrons have been used and has an intensity of 141 electrons per nm^3. Using the accepted value of atom density for GaAs, 44.2 atoms per nm^3, an average of 3.2 electrons per atom is calculated, slightly under the 4 valence electrons per atom average for GaAs.

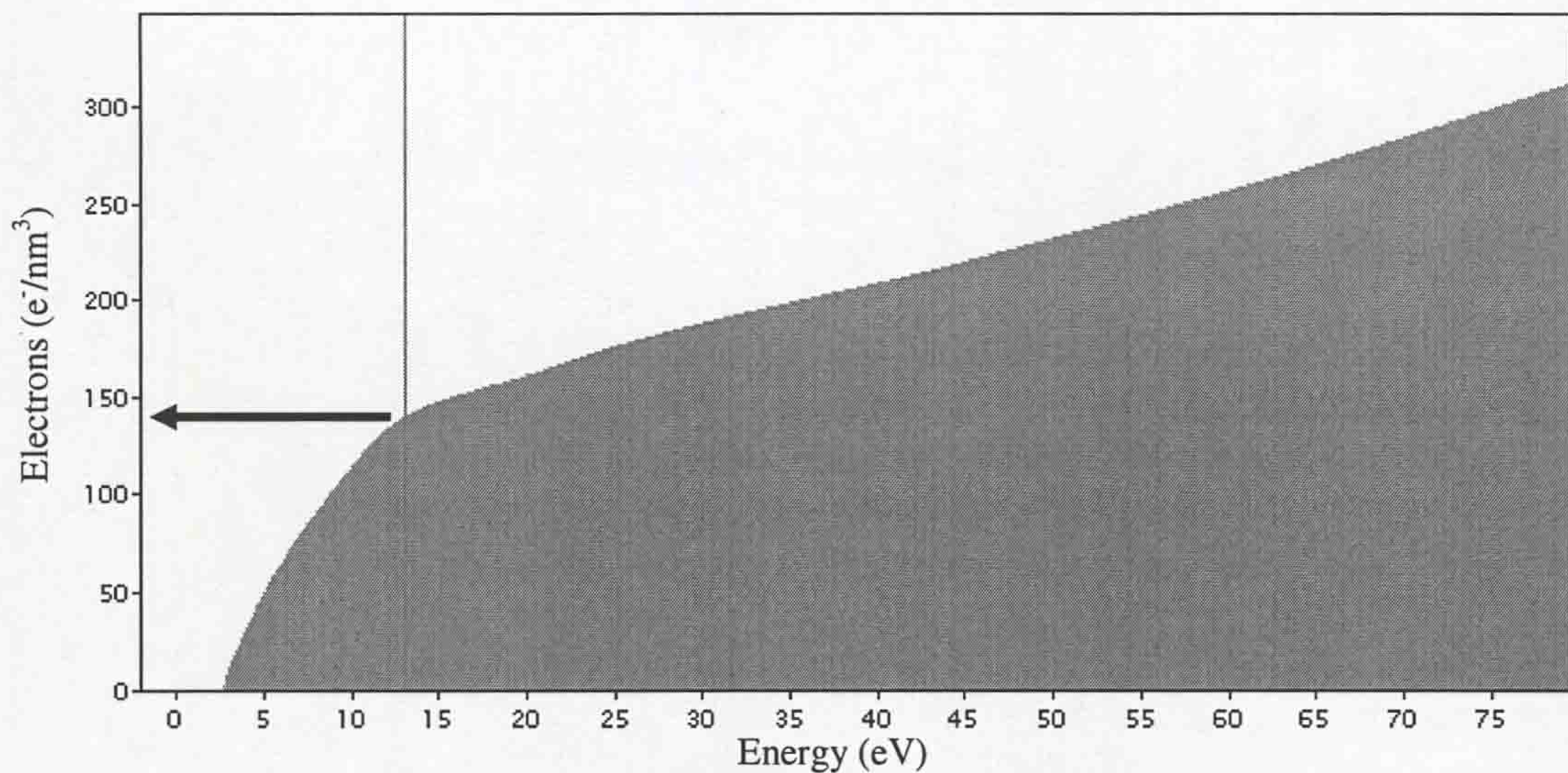

Figure 3-10. n_{eff} versus energy. The steep gradient at low energy loss is due to the valence electrons, the gradient changes when all the valence electrons have been involved.

3.4.5.4 Absolute sample thickness

Using the *Kramers-Kronig* sum rule, an iterative computation of the thickness, t, can be calculated by[12],

$$t = \frac{4a_0 F E_0}{I_0(1-n^{-2})} \int_0^{\infty} \frac{S(E)dE}{E\ln(1+\beta^2/\theta_E^2)} \qquad 3.7$$

where a_0 is the Bohr radius, F is a relativistic factor, E_0 the beam energy, I_0 the zero-loss intensity, n the refractive index for visible light, $S(E)$ the single scattered distribution, β the effective collection angle and θ_E the characteristic scattering angle. This method of determining sample thickness takes into account the surface-loss component and gives an absolute value. There are other methods, which give a relative value and are useful if there is a large variation in refractive index (n), or if the refractive index is unknown for a material, though a precise value of n is not essential in the calculations, as it affects the thickness as $1/n^2$ term.

3.4.5.5 Optical absorption coefficient

The optical absorption coefficient $\mu(E)$ can also be computed from the dielectric function using the following[12],

$$\mu(E) = \frac{E}{\hbar c}\left[2\left(\varepsilon_1^2 + \varepsilon_2^2\right)^{\frac{1}{2}} - 2\varepsilon_1\right]^{\frac{1}{2}} \qquad 3.8$$

where c is the speed of light in a vacuum.

3.4.5.6 Effective mass (m_e^*)

The effective mass is a very important parameter for semiconductor materials allowing electrons and holes to be treated as classically charged particles. It is possible to obtain direct measurements of the effective mass through EELS using the equation,

$$m_e^* = \frac{n\,\hbar^2}{E_p^2 \varepsilon_0 \varepsilon_\infty} \qquad 3.9$$

where $\hbar$ is Plank's constant divided by 2π, ε_0 the permittivity of free space and ε_∞ is the high frequency dielectric constant. Experimentally, m_e^* is obtained by using the calculated values of n (Section 3.4.5.3) to determine the number of electrons involved in the plasmon at the plasmon energy and, the plasmon energy, E_p (Section 3.4.4.2). It is possible to measure m_e^* in this way, as this plasmon is an oscillation of the valence electrons which have been promoted to the conduction band minimum[10] and n is a measure of the number of electrons which have been promoted to the conduction band at the same energy. This process relies on a very accurate removal of the plural scattering, ZLP and further KKA, as noise added in by these processes at the low-energy loss could result in a fluctuation of intensities for n, masking all useful information. Gatan was asked to write a script that uses the SI of the effective number of electrons and the map of the plasmon energy that determines the effective number of electrons at the plasmon energy for every pixel and puts the values back into equation 3-9 to obtain a map of m_e*. This script can be found in Appendix B3 (a script used to remove any value less than zero from the E_p map so that the calculations can be carried out can be found in Appendix B2).

3.5 Energy dispersive X-ray (EDX) analysis

As discussed previously, the incident electron beam may undergo elastic and inelastic scattering as it passes through an electron transparent specimen in the

TEM. The production of X-rays as a result of inelastic scattering was not discussed in Chapter 2 (electron sample interaction), as the chapter focuses on the energy loss of the incident electron for EELS analysis. However, on interaction with the specimen, the incident electron may lose energy equal to the energy needed to excite an atomic inner-shell electron to the conduction band. This leaves the atom in an excited electronic state, and a higher shell electron will fill the hole to allow the atom to return to its ground state. This latter transition is accompanied by the emission of a characteristic X-ray whose energy is equal to the difference in energy between the two electron shells involved, and thus is characteristic of the specific element.

Two EDX systems were used on the STEM during the period of this research, with the same detector in both cases. The detector used is an Oxford Applied Instruments silicon-lithium windowless detector, cooled with liquid N_2 and attached to the STEM in such a way that it is within 400μm of the sample during acquisition. EDX analysis is used as a secondary technique to confirm results obtained through procedures being developed from EELS data.

3.6 Photoluminescence

With the exception of the samples grown by LAAS, the photoluminescence (PL) measurements of the GaInNAs quantum wells and laser structures quoted during this research were provided by colleagues in the Department of Physics at University of Essex. The process of PL is the induction of optical emission from a specimen via

photon excitation from a laser. A laser is focused onto a specimen and if the incident photons have an energy that is greater than the band gap of the specimen, the sample will emit light as photons. Due to the thermal effect on band gap energy, PL investigations of semiconductors are often carried out at low temperatures. This will maximise optical emission and reduce spectral width. Many of the PL values quoted were measured at a temperature of 77K and were extended out to 300K to determine the band-gap at room temperature by using a model developed by Potter for the rapid calculation of interband transitions in dilute nitride quantum well structures with the addition of information such as quantum well width and gamma.

The excitation source used at Essex is a 647nm wavelength krypton ion laser with a spot size at the specimen of diameter ~0.25mm. PL measurements could be carried out at a range of temperatures from T = 4 to 300 K and is a standard technique used for band gap determination. It can also be used to determine the concentration of elements present.

References

[1] R. Keyse, P.J. Goodhew, A.J. Garratt-Reed and G.W. Lorimer, Introduction to Scanning Transmission Electron Microscopy, BIOS Scientific Publishers Ltd, Oxford (1998)

[2] R.F. Egerton, Electron Energy Loss Spectroscopy, Chapter 1, page 5, Plenum Press, NY (1986)

[3] R.F. Egerton, Electron Energy Loss Spectroscopy, Apendix D, page 371, Plenum Press, NY (1986)

[4] C.C. Ahn, O.L. Krivanek, EELS Atlas, Gatan Inc., (1983)

[5] S. Massidda, A. Continenza, A.J. Freeman, T.M. de Pascale, F. Meloni and M. Serra, Phys. Rev. B, **41**, 12079 (1990)

[6] G.B. Blachelet and N.E. Christensen, Phys. Rev. B, **31**, 879 (1985)

[7] R.F. Egerton, Electron Energy Loss Spectroscopy, Chapter 4, page 243, Plenum Press, NY (1986)

[8] R.F. Egerton, Electron Energy Loss Spectroscopy, Apendix B5, page 367, Plenum Press, NY (1986)

[9] H. Ibach and H. Lüth, Solid State Physics, Chapter 11, page 350, Springer-Verlag Berlin Heidelberg (2003)

[10] D. Pines, Elementary Excitations in Solids, W.A. Benjamin Inc., NY (1963)

[11] S. Schamm and G. Zanchi, Ultramicroscopy, **96**, 559 (2003)

[12] Gatan Inc, Digital Micrograph EELS Analysis User's Guide, Chapter 3, Revision 1.2 (2003)

Chapter 4

Results: Elemental quantification using semi-core states

Section		Page
4.1	Quantum well and full laser structure specimens analysed in this study	86
4.2	Factors affecting the energy loss spectrum	88
4.3	Quantification of sample composition using semi-core states in energy loss spectra	92
4.4	Discussion	110

4 Results: Elemental quantification using semi-core states

This chapter is divided into three parts. In Section 4.1 the structure of the samples to be studied in this thesis will be presented. This is followed with a discussion of factors that affect electron energy loss (EELS) data in Section 4.2, such as specimen thickness and carbon contamination. In Section 4.3 elemental edges measured in the low loss EELS spectrum will be used for quantification of the composition and mapping of quantum wells.

4.1 Quantum well and full laser structure specimens analysed in this study

As a consequence of the conclusions drawn in Section 3.2, all specimens analysed herein have been prepared by the conventional method of mechanical grinding and ion-beam thinning to minimise modifications of the as-grown crystal structure. A summary detailing the composition of the samples investigated is given below, including compositions estimated from photoluminescence (PL) studies where possible.

Four different GaInNAs single-QW samples were investigated. These are referred to as M1048, M1049, M1055 and Fr1473. The *M* indicates that the samples were grown by CBE at Liverpool and the *Fr* indicates that the sample was grown by MBE in France (LAAS). Each sample also contains a reference GaInAs QW that was grown before the GaInNAs QW, separated by a GaAs spacer layer. Table 4-1 below shows the QW width and composition (In fraction), which the growers were aiming

for, and the In and N fractions in the QW estimated after growth from PL (when undertaken).

Table 4-1 QW width and compositions of samples studied.

Sample ID	QW	Width of QW	Growth T (°C)	Fraction In (from growth)	Fraction In (from PL)	Fraction N (from PL)
M1048	GaInNAs	7	450	0.1	0.11	0.031
M1049	GaInNAs	7	450	0.1	0.11	0.037
M1055[i]	GaInNAs	7	450	0.3	0.18	---
	GaInAs	3		0.3	0.18	---
Fr1473[i]	GaInNAs	6	400-500		0.24	0.023
	GaInAs	10	400-500		0.24	---

Two different "laser structures" have also been investigated, both containing a single GaInNAs QW as shown in Table 4-2. Fr1485 is doped and has graded layers of AlGaAs whereas M1058 in undoped throughout and has uniform AlGaAs layers.

Table 4-2 Growth of two GaInNAs QW "laser structures".

M1058		Fr1485	
		50nm	GaAs:Be
200nm	GaAs	200nm	GaAs: Be
1600nm	$Ga_{0.80}Al_{0.20}As$	1200nm	$Ga_{0.4}Al_{0.6}As$: Be
		170nm	$Ga_{(0.8-0.4)}AlAs_{(0.2-0.6)}$: Be
150nm	GaAs	100nm	GaAs
7nm	$Ga_{0.80}In_{0.20}N_{0.02}As_{0.98}$ QW	10nm	$Ga_{0.65}In_{0.35}N_{0.01}As_{0.99}$ QW
150nm	GaAs	100nm	GaAs
		170nm	$Ga_{(0.8-0.4)}AlAs_{(0.2-0.6)}$: Si
1600nm	$Ga_{0.80}Al_{0.20}As$	1200nm	$Ga_{0.4}Al_{0.6}As$: Si
		170nm	$Ga_{(0.4-0.8)}AlAs_{(0.6-0.2)}$: Si
1200nm	GaAs	1000nm	GaAs: Si
Substrate	GaAs	Substrate	GaAs: Si

Two different III-V systems were also investigated to confirm the techniques developed during this work. The first system was InAs QDs on a GaAs substrate, where the InAs layer thickness was chosen to be above the critical thickness leading

[i] Only GaInAs QW data from M1055 and Fr1473 is given in the table, as no results were collected from the M1048 and M1049 GaInAs QW.

to the formation of QDs. The second system was wurzite AlGaN/GaN where the layers were approximately 600 to 850 nm thick.

4.2 Factors affecting the energy loss spectrum

In this section, the effects of specimen thickness and carbon contamination on the EELS spectra are considered. The low-loss region of the EELS spectrum contains a lot of information. However, carbon contamination can alter the observed spectrum as it has several broad peaks in the first 30eV. It is thus important to know if carbon is present. If the specimen is contaminating, the carbon can build up during an acquisition, swamping and shifting the apparent position of other transitions.

4.2.1 Thickness effects on the energy loss spectrum

The thickness of specimen that the STEM electron beam has to pass through affects the EELS spectrum. As discussed in Chapter 2, plural scattering occurs if the specimen thickness approaches or exceeds the mean free path (MFP) of an inelastic scattering process. The MFP is described as the average distance travelled by an incident electron between two scattering events. For a 100keV electron beam scattering from the outer-shell electrons, the MFP can be of the order of 50 – 150 nm, depending on the scattering mechanism. It is common practice to remove the plural scattering from EELS spectra using a *Fourier-Log* deconvolution and it is therefore not a problem as long as there is still a significant contribution to the spectrum from single scattered electrons. However, if the specimen becomes too thin, it can create other problems such as the introduction of surface plasmons[1] into the EELS spectrum. Moreover it will be shown here that when the specimen

reaches a thickness less than ~25 nm the plasmon energy increases. Using the procedure described in subsection 3.4.4.2 to calculate the plasmon energy, a map of plasmon energy has been produced for the laser structure M1158. This map can be seen in Figure 4-1b, taken from the boxed region of the bright field image in Figure 4-1a. A temperature scale is used where blue/black represents a low energy and yellow/white represents a higher energy. It can be seen that the plasmon energy increases from the top to the bottom of the mapped region and there is a corresponding decrease in Figure 4-1c, the thickness map.

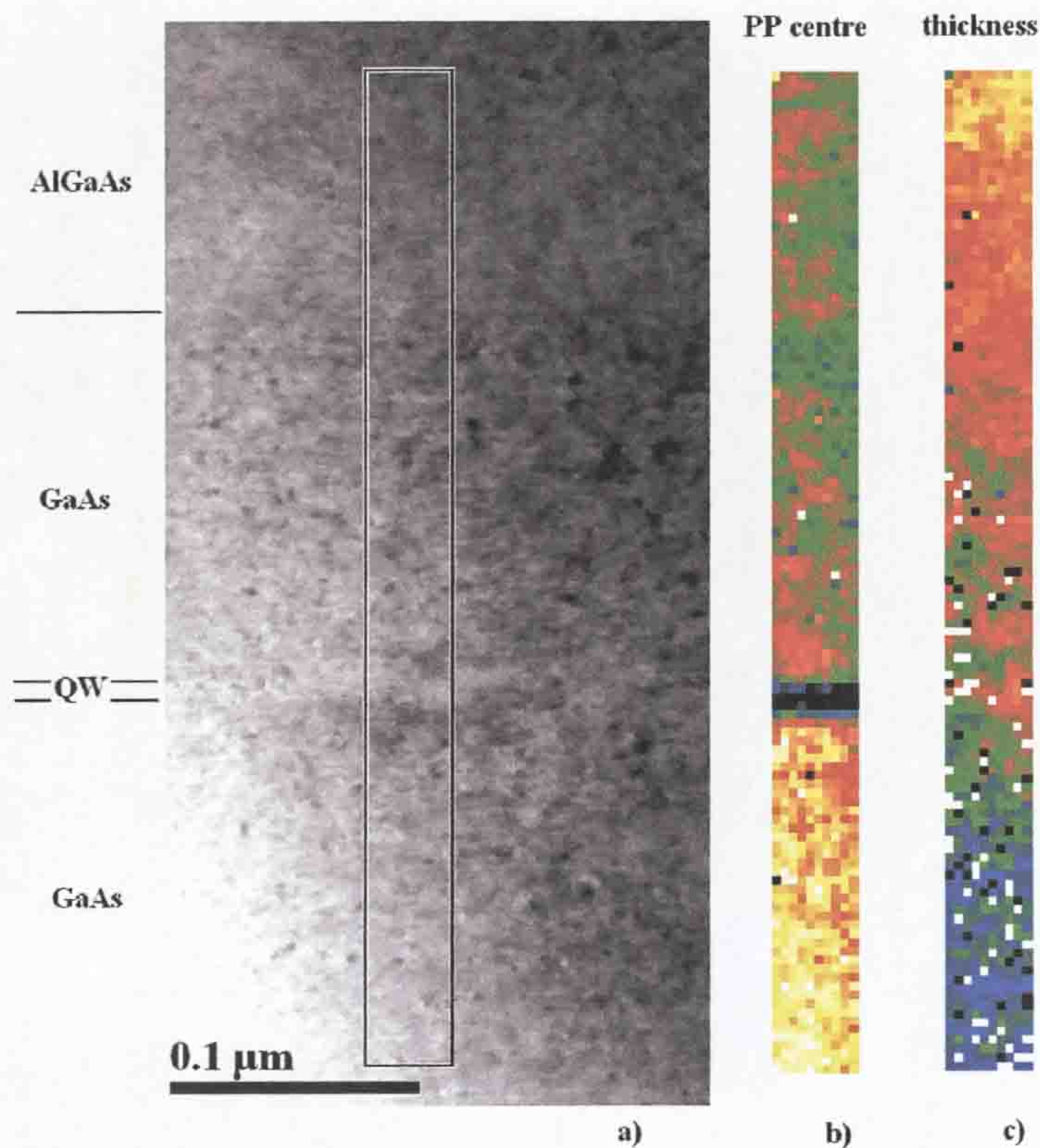

Figure 4-1. a) A bright field image of laser structure M1158 with the analysed area shown by the boxed region. The change in thickness can be seen in the contrast change of the bright field image and in c) where the absolute thickness ranges from 22 to 27nm. b) shows how the plasmon energy changes through the sample from 15.65 to 16.00eV. The black and white pixels in the thickness map are due to failure of the *Kramers-Kronig* routine.

This is also shown graphically by the dark diamond shaped data points in Figure 4-2, in which the plasmon energies from various points across the GaAs regions are plotted against the absolute thickness at each point (see subsection 3.4.5.4), obtained from the *Kramers-Kronig* (KK) transformations. The light triangular data points on the graph are from a different area of the same specimen, acquired during the same session. It must be noted that the light data points were acquired from GaAs 4 - 10nm from the GaInNAs QW, so there is a possibility that some of the measurements could have been affected by the presence of the QW. The graph shows that for specimen thickness above ~25nm, the large majority of plasmon energies from GaAs all lie between 15.90 and 16.03eV. However when the thickness decreases below this value, the plasmon energy will significantly increase. It is therefore necessary that GaAs specimens have a thickness greater than ~25 nm, equivalent to ~ 0.5 x MFP for reliable analysis of the type undertaken in this study to be carried out.

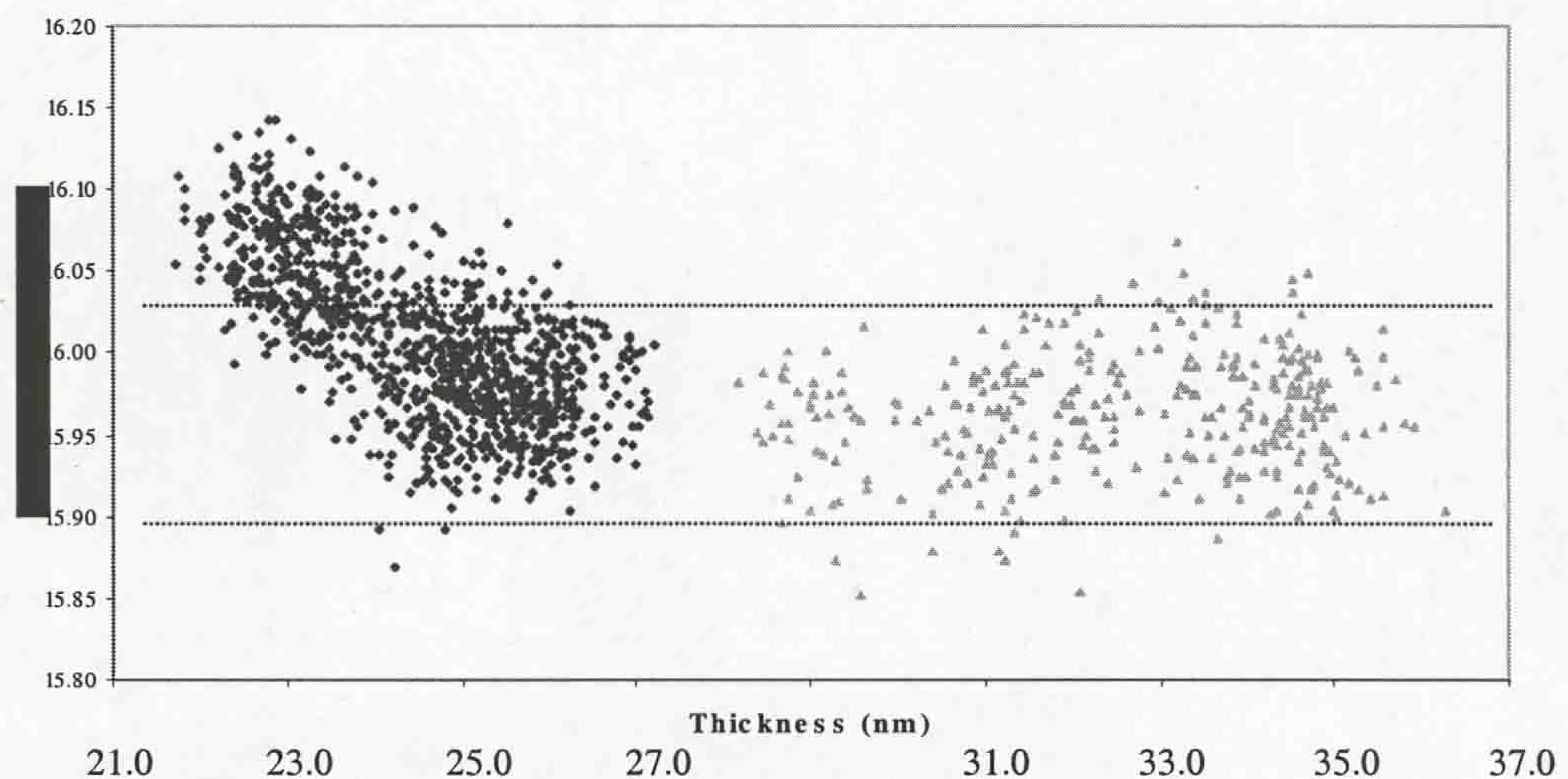

Figure 4-2. The plasmon energy from the GaAs regions in Figure 4-1b is plotted against the thickness of the specimen (dark diamond data points). The light triangular data points are taken from data acquired the same session on the same specimen, but from a different region of GaAs.

4.2.2 Carbon contamination during energy loss acquisition

Carbon contamination is a common occurrence in electron microscopes and particularly in STEMs due to the intensity of the focused electron beam at the specimen. It can be a consequence of many factors, such as a poor vacuum or a dirty specimen. For cross-sections it may also be a result of the epoxy glue covering the region of the specimen to be analysed. The observed contamination is a result of a build-up of carbon that is created on the specimen's surface in the vicinity of the electron probe as data is being acquired. Figure 4-3 shows how the low loss spectrum of GaAs is affected when there is carbon contamination. The two C transitions; the π plasmon at ~6 eV and the $\pi + \sigma$ plasmon at ~23 eV are apparent, and the latter completely obscures the Ga $M_{4,5}$ transition which has an onset of ~21eV. The presence of C has also caused an apparent shift of the GaAs plasmon energy up to 16.4eV. These effects prevent any analysis to be carried out in the low loss region for GaAs. For all samples studied, acquired EL spectra must be checked to confirm there is no significant C contamination, either by checking the EL region where the π peak occurs or by checking if the two peaks of the Ga $M_{4,5}$ edges are less distinct due to the $\pi + \sigma$ C-plasmon. When small amounts of C contamination are present in the EL spectra presented in this thesis, this is indicated.

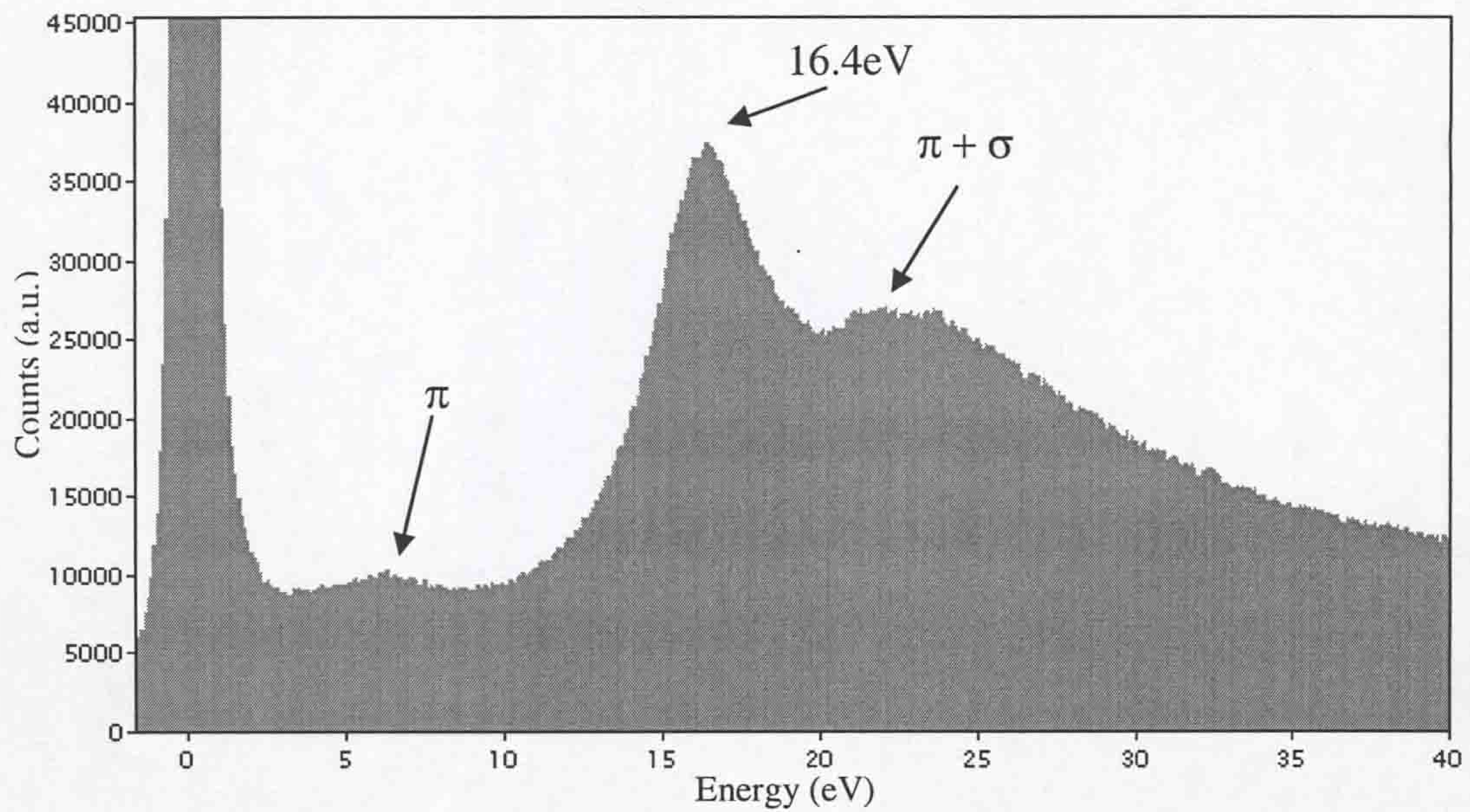

Figure 4-3. The low loss spectrum of GaAs which has suffered from carbon contamination. The two C plasmons, π and π+σ, can be seen at ~6eV and 23eV respectively, with the GaAs plasmon energy at 16.4eV.

4.3 Quantification of sample composition using semi-core states in energy loss spectra

The following sections deal with the quantification of the group III elements in GaInNAs QWs (4.3.1), InAs QDs (4.3.2) and GaN/AlGaN heterostructure (4.3.3) using the techniques described in Chapter 3. In 4.3.4 the quantification of group V elements in GaInNAs is also considered.

4.3.1 Quantification of the composition of group III elements in GaInNAs

The compositional quantification results from the single scattering distribution (SSD) and epsilon 2 (ε_2) will be compared by applying the two techniques described in subsection 3.4.5.2 to data acquired from a large area of a GaInNAs QW laser

structure at a low magnification. The laser structure is Fr1485 (see Table 4-2) from LAAS and consists of a 10nm GaInNAs QW flanked by 100nm undoped GaAs barrier layers, followed by graded AlGaAs layers, each 170nm thick. Each graded layer is bound by 1200nm of doped AlGaAs. The near-surface Be doped (p-type) AlGaAs is capped by 250nm of Be-doped GaAs, while the Si-doped (n-type) AlGaAs is separated from the GaAs substrate by another AlGaAs 170nm graded layer. Figure 4-4 shows a bright field image from a cross-section of this GaInNAs/GaAs QW laser structure. Also in this figure are maps of the Ga $M_{4,5}$ signal after background has been removed for the SSD in Figure 4-4b and epsilon 2 in Figure 4-4c. Their respective histograms show the spread of Ga concentration with the two intense peaks representing GaAs (Ga equals 100% of group III elements) and AlGaAs (Ga equals 40% of group III elements).

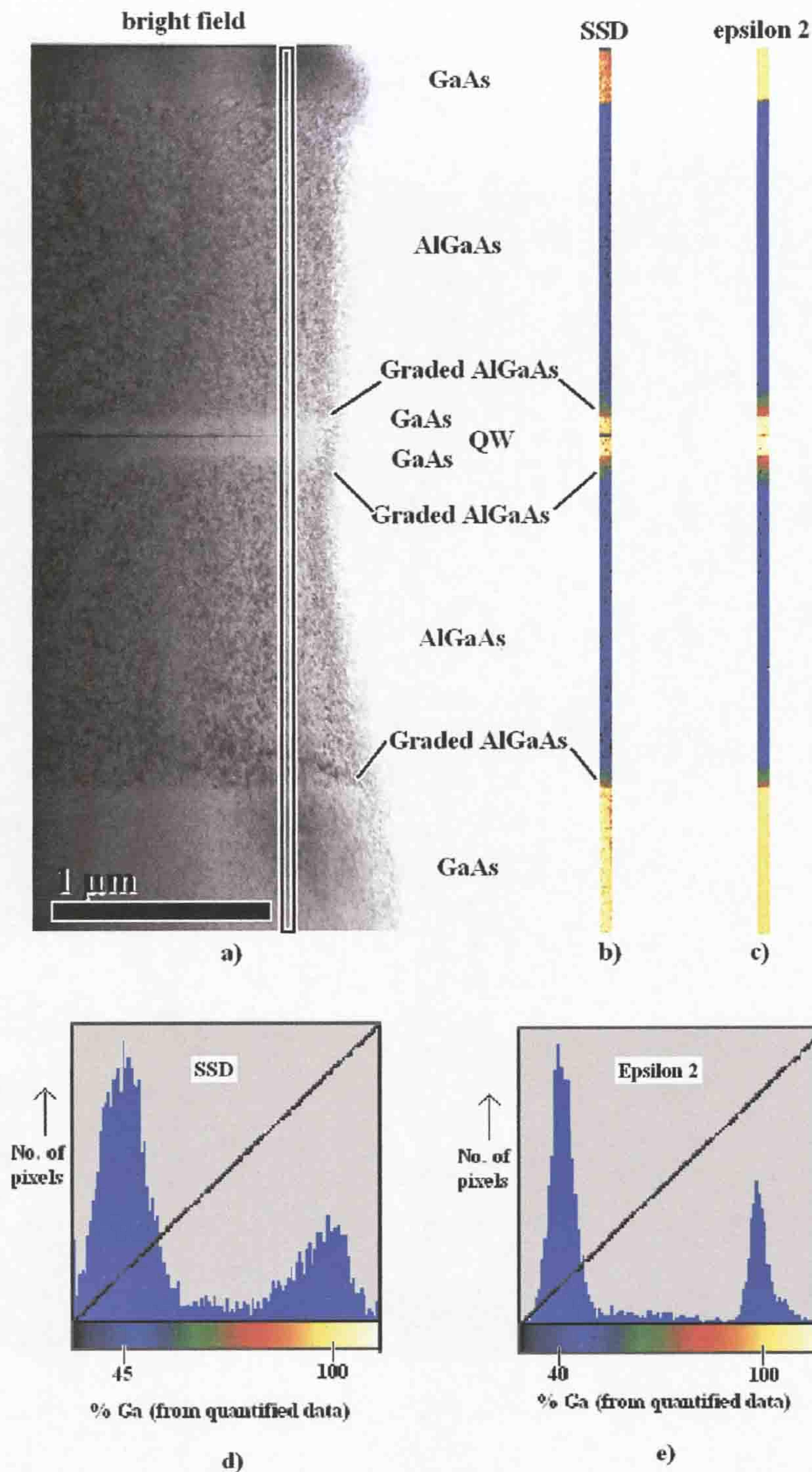

Figure 4-4. a) A bright field image of the GaInNAs QW laser structure with the substrate towards the bottom. The boxed area is the region mapped by EELS in b) which shows the single scattered distribution of the Ga $M_{4,5}$ edge intensity with the background removed whilst c) shows the ε_2 intensity over the Ga 3d transition with the background removed. d) and e) are histograms showing the number of pixels in the SSD and ε_2 maps corresponding to Ga concentrations, estimated from quantifying and normalising the Ga $M_{4,5}$ edge and Ga 3d transition intensities as explained in the text. Note, the intensity scales for the maps in b) and c) are shown in the % Ga axis in d) and e) respectively.

The background removal for the Ga $M_{4,5}$ edge must be performed in such a way that it achieves the best possible fit to the background for every spectrum in the spectrum image (SI) and is achieved by altering the width and position of a background window at energies just below the edge. This is shown in Figure 4-5a, where a signal window between 20.0 and 24.0eV defines the integral from which the Ga $M_{4,5}$ edge intensity will be calculated. The window's position and width is fixed and is used for the Ga signal integration throughout this thesis. The Ga $M_{4,5}$ edge sits on the back of the plasmon peak in the SSD so it is not straightforward to get an accurate background fit using SSD, as the plasmon energy also changes with composition. Figure 4-4b shows a map from the boxed area in Figure 4-4a of this integrated Ga edge intensity with the background removed. In this map, the GaAs in the substrate has been normalised to an average nominal intensity value of 100, to represent Ga being 100% of the group III elements present, this is also represented in the histogram, where the GaAs peak occurs at 100. The reduction in Ga concentration in the AlGaAs and GaInNAs regions can be clearly seen. However, it is clear that there is an effect due to sample thickness, as the GaAs cap layer has an intensity of less than 100. There is also a large spread of intensity in what in nominally GaAs and AlGaAs of fixed composition, which is seen pictorially in the histogram as the two intense peaks, Figure 4-4d. The compositions given in Table 4-3 show that the standard deviation of the different layers calculated from the SSD is generally higher and the value not as close to the nominal growth value compared to those from ε_2. As expected, the QW has a high standard deviation, as the composition is not uniform.

	GaAs (substrate)	**AlGaAs** (uniform)	**GaAs**	QW	**GaAs**	**AlGaAs** (uniform)	**GaAs** (cap)
SSD (Figure 4-4b)	100.4 ± 7.1	45.2 ± 8.5	100.7 ± 7.1	41.3 ± 8.2	98.1 ± 7.9	43.8 ± 7.5	88.9 ± 6.3
ε_2 (Figure 4-4c)	100.0 ± 2.2	40.9 ± 2.8	107.2 ± 2.8	81.5 ± 7.9	105.3 ± 3.2	40.9 ± 3.0	102.3 ± 2.6
ε_2 (Figure 4-6b)	——	——	100.5 ± 3.3	65.5 ± 9.3	101.2 ± 4.6	——	——
Target growth composition	100	40	100	65	100	40	100

Table 4-3. Amount of Ga in the various layers of the laser structure as a percentage of group III elements, the error is taken from the standard deviation of the results.

In Figure 4-5b the Ga 3d transition in ε_2 is shown, before and after the background has been removed, using the same signal energy window as used for the SSD (Figure 4-5a). Figure 4-5c from the GaInNAs QW show both the In 4d and Ga 3d edges. The background removal has been optimised to get the most consistent fit possible for all the spectra in the map. As there is no plasmon peak in ε_2 it is somewhat easier to find an appropriate fit to the background. Figure 4-4c shows the map of this Ga 3d transition intensity in ε_2 (with background removed) for the same boxed area as in Figure 4-4b. The map intensities have again been normalised so that the Ga content of the GaAs substrate equals 100%. The variation of the intensity in individual pixels contained in the GaAs and uniform AlGaAs areas of the maps are significantly reduced compared with the SSD map in Figure 4-4b. The two peaks in the intensity histogram (Figure 4-4e) representing the variation in Ga concentration across the GaAs and AlGaAs areas therefore have a much narrower width.

Table 4-3 compares the average composition and standard deviation from quantification analysis of SSD and ε_2 spectra from all the pixels in each region of the maps shown in Figure 4-5. The compositions obtained from ε_2 intensities are in better agreement with the sample compositions expected from the growth conditions than those from the SSD. The three graded $Al_xGa_{1-x}As$ (x = 0.2-0.6) layers are visible in both maps, although grading is noticeably smoother for the ε_2 map. It is also observed that using the ε_2 signal, the estimated Ga percentage in the QW and in the GaAs barrier layers around the QW are very slightly higher than expected. This might be a consequence of strain in these layers, as strain can change the absorption effects of a material. Strain effects are not seen in the SSD in Figure 4-4b, and this

may indicate that strain information may also be extracted by comparing absorption spectra and SSD data.

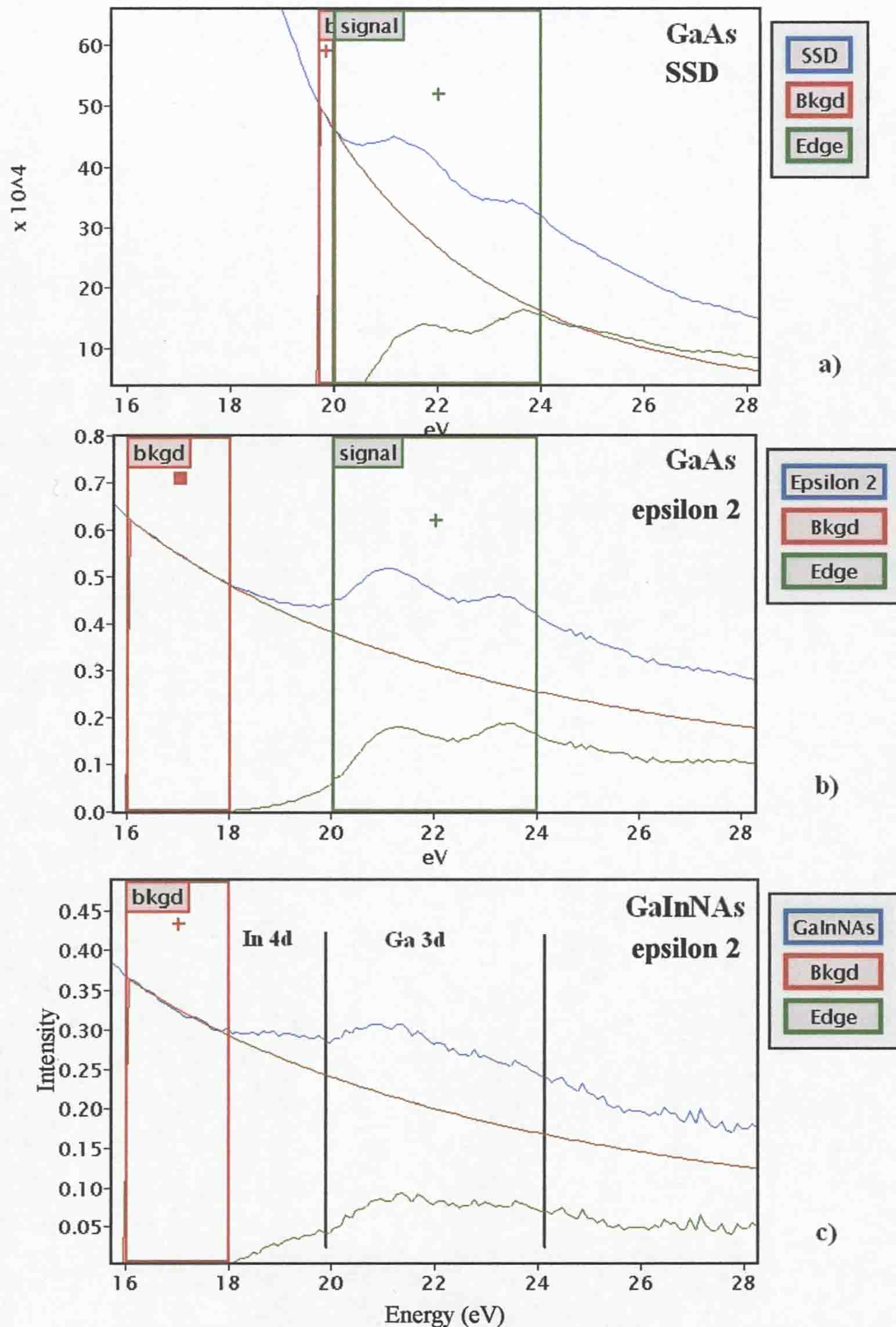

Figure 4-5 Show a series of spectra, where the blue line is the spectrum before background removal, the red line is the background and the green line is the extracted edge. a) Shows the Ga $M_{4,5}$ edge in the SSD and b) the Ga 3d transition in epsilon 2. c) is from the GaInNAs QW and shows both the In 4d and Ga 3d edges in epsilon 2.

A higher magnification bright field image of the GaInNAs QW from the same sample is shown in Figure 4-6a. An EELS map was acquired from the boxed area with a pixel resolution of 72 x 50, giving a pixel size of 0.85nm. The ZLP and plural scattering were removed from each spectrum, as discussed previously, and the *Kramers-Kronig* analysis performed. Figure 4-6b shows the map of the Ga 3d transition intensity in ε_2 with the background removed. By setting the average transition intensity in the GaAs either side of the GaInNAs quantum well to 100 at% Ga, the variation in the Ga distribution within the QW can be seen. Although the design composition of the QW is 65% Ga, the map shows this is reduced to as little as 45% (dark blue / black pixels in map) of the group III elements in some places. However, the average over the 10nm quantum well gives a concentration of 65.6%, which is in good agreement with the expected level from the growth parameters. The In 4d ε_2 transition map is shown in Figure 4-6c; and although this signal cannot reliably be used for quantitative analysis as the energy window integrated is very narrow, it can be used to show the spatial distribution of In in the QW. It is clear that the depletion of Ga in Figure 4-6b, corresponds to an increase of In in Figure 4-6c.

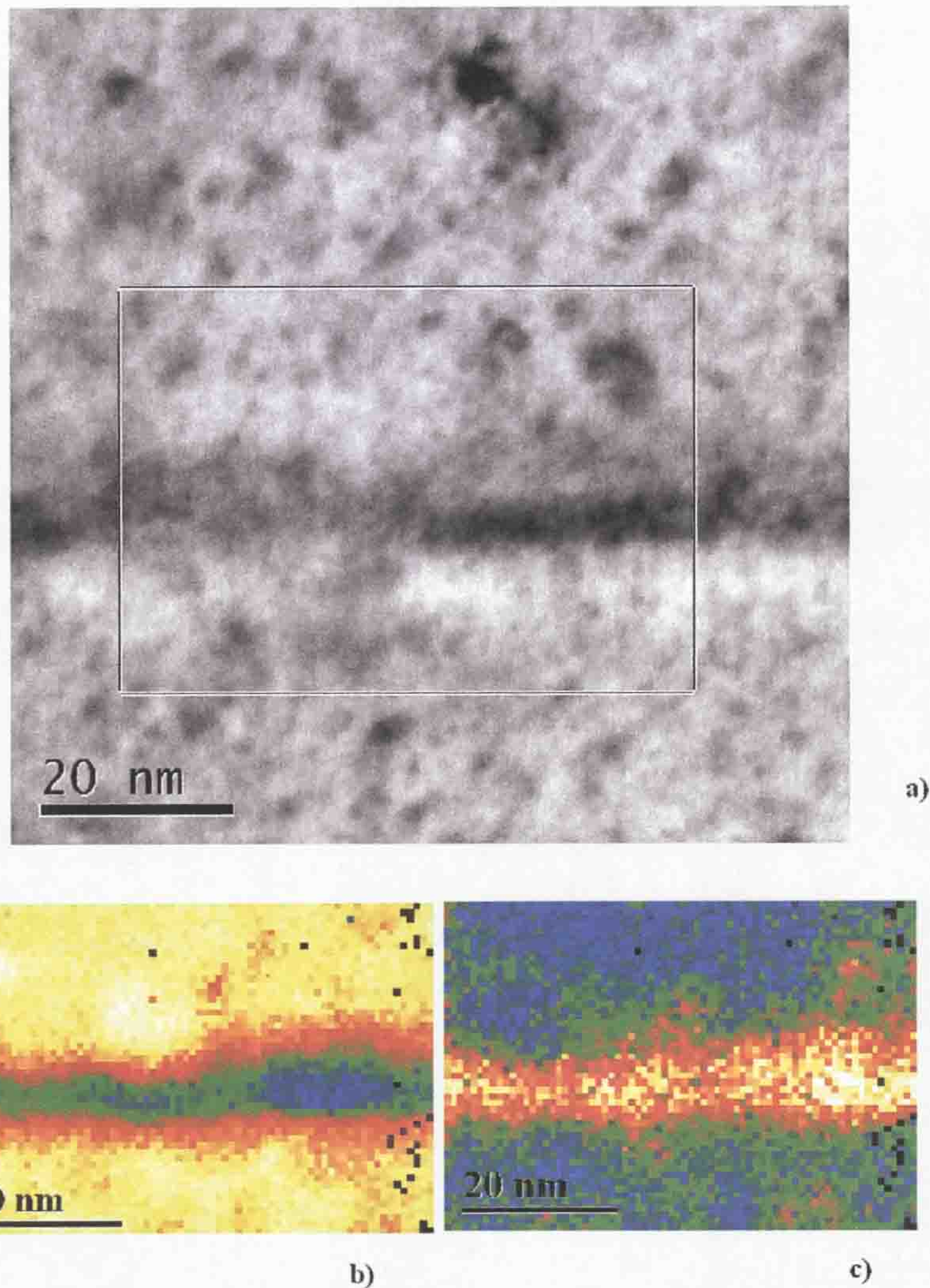

Figure 4-6 a) shows the STEM bright field image acquired at a magnification of x10^6, from around the 10 nm GaInNAs quantum well. The boxed area is the region mapped by EELS. b) is a map of the intensity of the Ga 3d transition in ε_2 and c) is a map of the In 4d transition in ε_2. Note that the black pixels in b) and c) are "dead" pixels due to a failure in the *Kramers-Kronig* routine and have not been included in the subsequent calculations.

Whilst it is not possible to quantitatively determine the Ga and In fraction within a specimen when there is significant carbon contamination or poor signal-to-noise, it is still possible to use the ε_2 mapping to qualitatively compare compositions across mapped areas. For example, during acquisition of the data for Fr1473, carbon contamination was observed. The carbon $\pi + \sigma$ plasmon occurs at the same energy region in the spectrum as the Ga 3d and In 4d peaks, so it is no longer feasible to use

the technique described in this study to quantitatively analyse the composition. However, as the analysed data is presented in the form of a map, it is still possible to qualitatively compare the compositions of GaInNAs QWs with GaInAs QWs when they are both present in the same sample. An example is shown in Figure 4-7 for the Fr1473 sample (see Table 4-1 for data), where ε_2 maps of the Ga 3d and In 4d signals show the change in composition through the GaInNAs and GaInAs QWs. The effect of increasing C contamination during the acquisition can be seen by the change in intensity going through the maps. This can be seen graphically in Figure 4-8, where spectra of GaAs have been taken from the top (blue line) and the bottom (red line) of the map. It can be seen by comparing the two curves that during the acquisition period the C π plasmon at ~6eV has increased and the resolution of the two Ga 3d edges has reduced. Although the C contamination is small in comparison with the example given in Figure 4-3, where the change in concentration of the Ga 3d and In 4d would not be resolvable, it is enough to affect the quantification process as the Ga does not appear uniform in the GaAs. However, it is reasonable to infer from Figure 4-7 that concentrations of Ga and In are similar in the GaInNAs and GaInAs QWs.

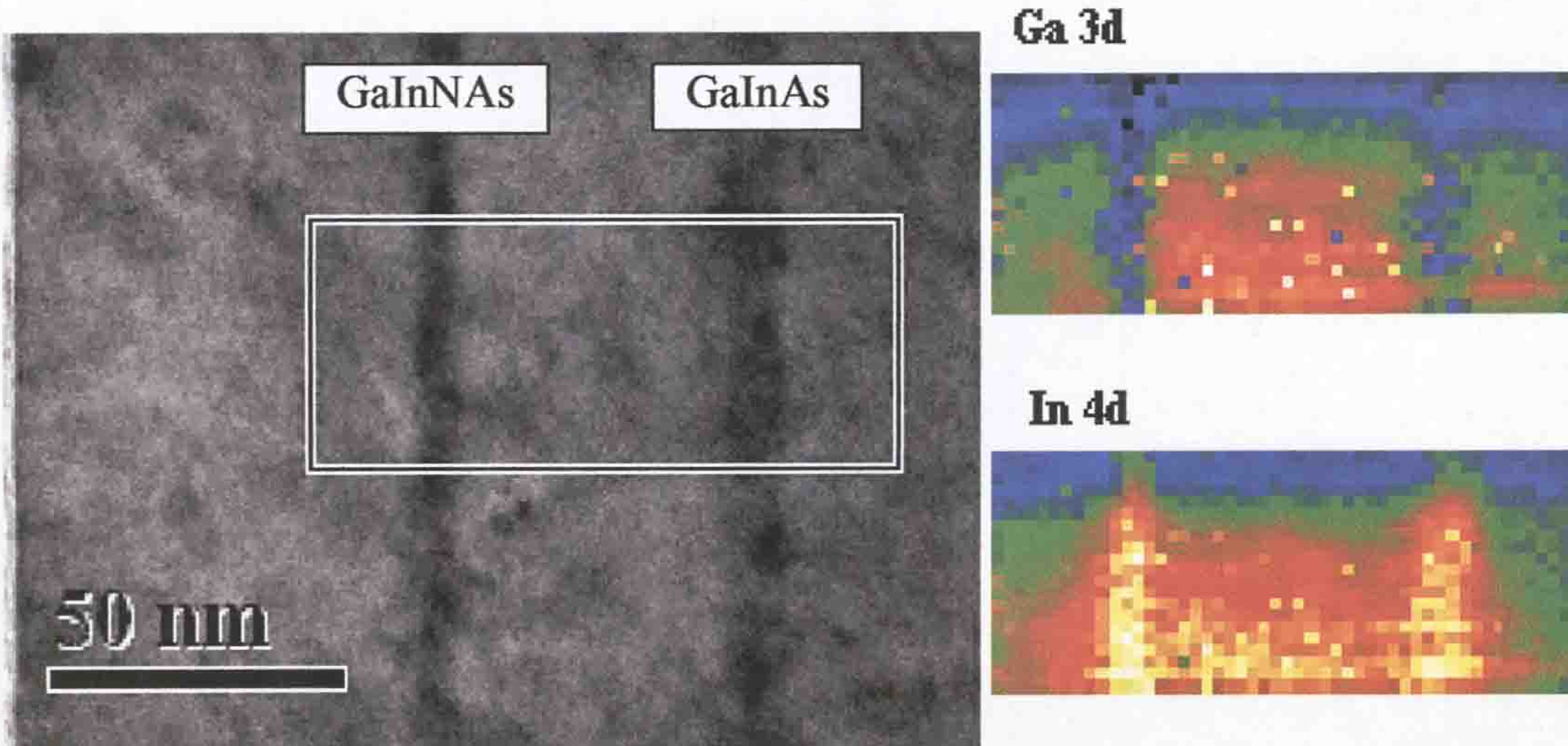

Figure 4-7. A bright field image of sample Fr1473. The Ga 3d and In 4d maps are from the boxed region and are displayed in arbitrary units. The change in intensity from top to bottom of the maps is due to the increasing C contamination.

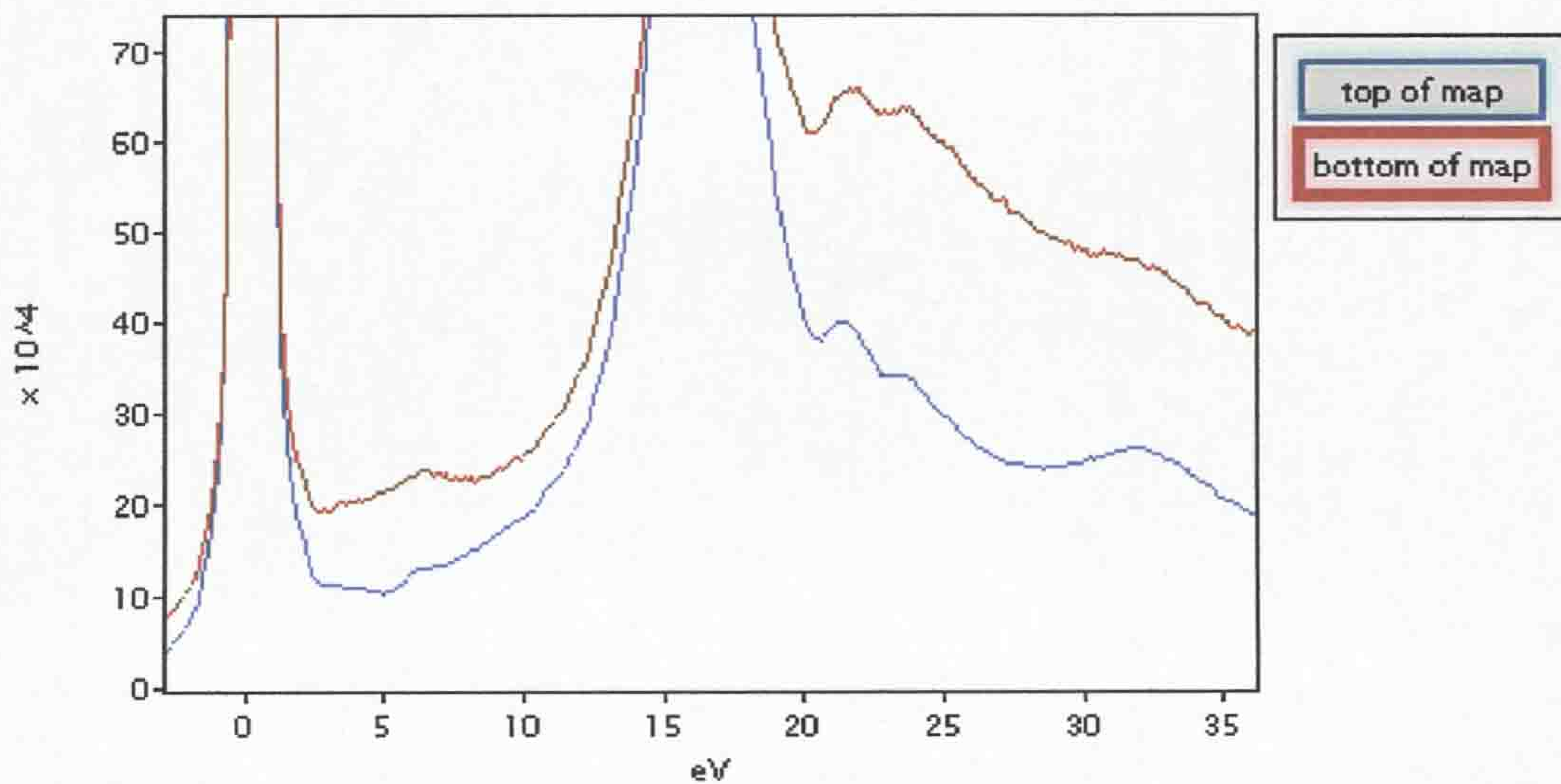

Figure 4-8. These spectra show the GaAs energy loss taken from the top of the map (blue) and from the bottom of the map (red) near the end of the acquisition.

Figure 4-9 shows bright field images and corresponding maps of the Ga 3d and In 4d intensities from M1055, which, like Fr1473 has both a GaInAs and GaInNAs QW. Although the GaInNAs QW was intended to have nominally the same In concentration as the GaInAs QW, it can be seen by comparing the Ga 3d and In 4d

intensities that this is not the case. In the GaInNAs QW Ga and In can clearly be distinguished, suggesting a high concentration of In. However, in the GaInAs QW it is very difficult to distinguish the QW region when examining the Ga 3d and In 4d intensities.

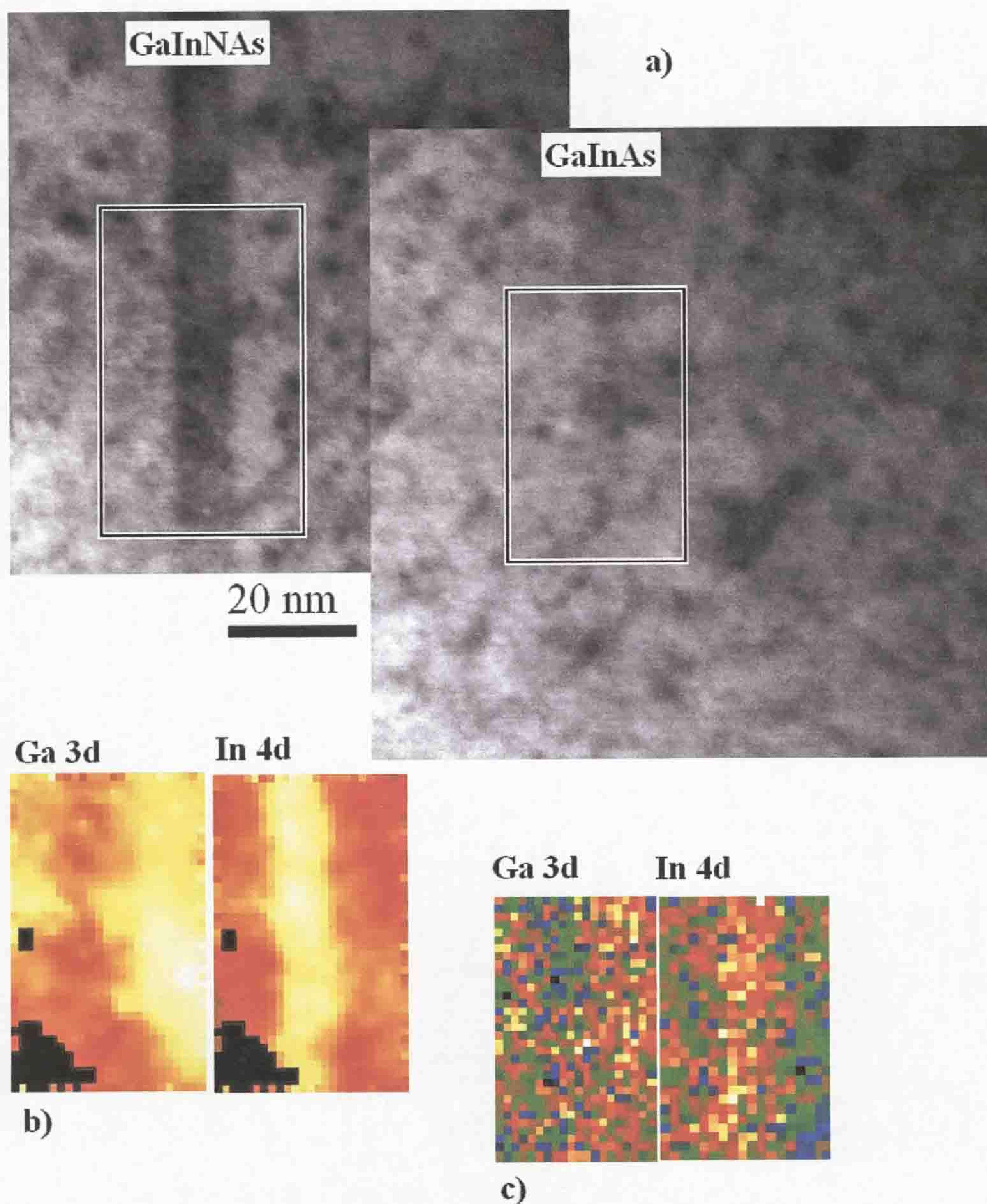

Figure 4-9. Sample M1055, a) is bright field images showing the GaInNAs QW on the left and the GaInAs QW on the right, b) and c) demonstrate the changes in concentration of Ga and In in the GaInNAs and GaInAs QWs respectively. It can be seen that the QWs do not exhibit similar Ga and In compositions.

4.3.2 Quantification of the composition of group III elements in InAs QDs

From ε_2, the same procedure has been used to determine the In and Ga concentrations of InAs QDs on a GaAs substrate. In Figure 4-10 it can be seen that where there is a QD present, there is a corresponding reduction in Ga, however, the increase in In is not as well defined and it has not been possible to quantify the Ga 3d data due to the carbon contamination suffered during the acquisition.

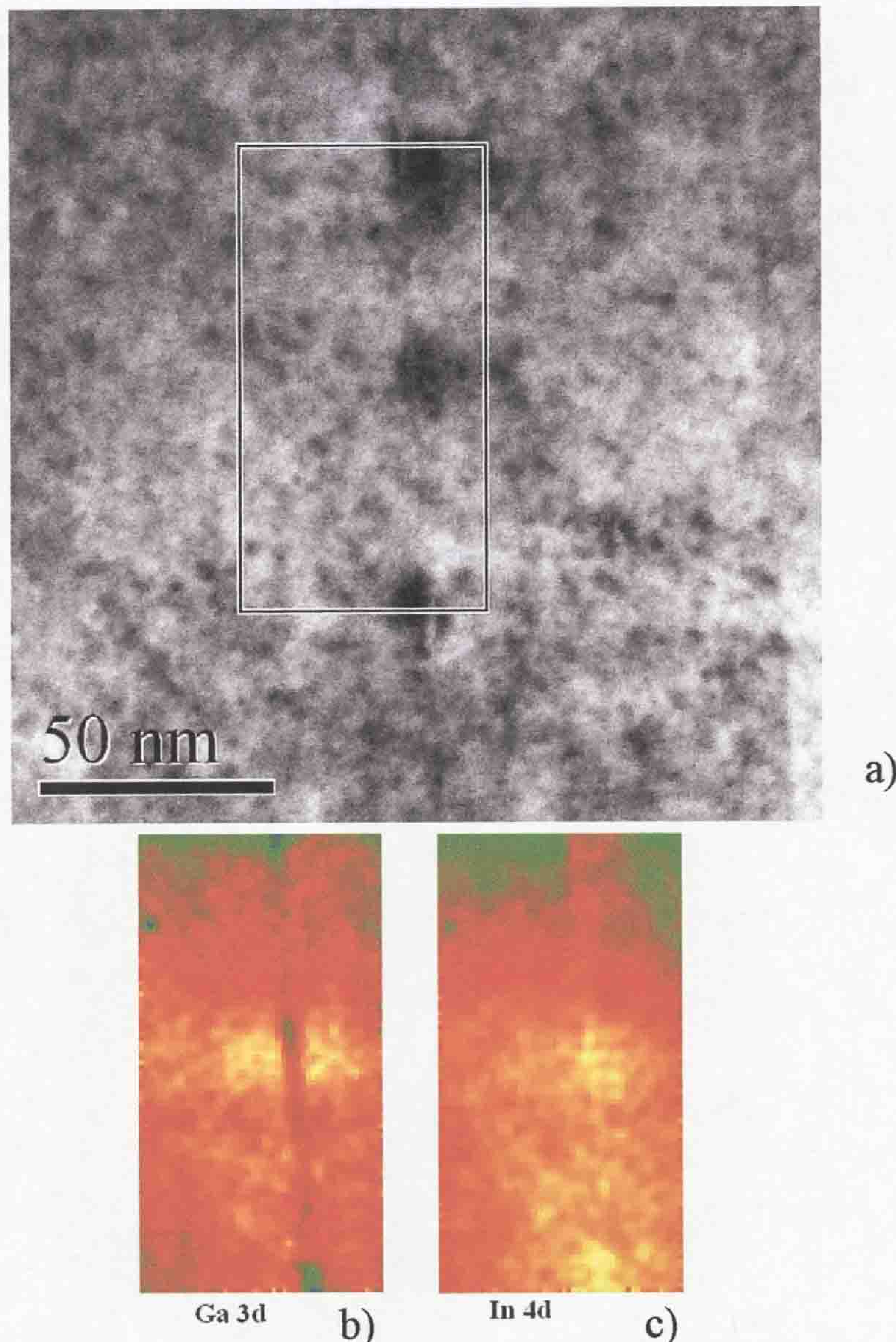

Figure 4-10. The bright field image of InAs QDs in a GaAs matrix can be seen in a). b) and c) show the Ga 3d and In 4d signals respectively. It is not possible to quantify the data as carbon contamination has occurred during data acquisition. It can be seen that where the InAs QDs can be seen in the bright field image, a reduction of Ga is observed.

4.3.3 Quantification of the composition of group III elements in GaN/AlGaN

The final system is wurzite GaN / AlGaN, grown on Si (111) with an AlN buffer layer. Interest has been shown in the growth of GaN on Si (111) for III-nitride light emitting devices, as Si(111) is more accessible than the conventional sapphire or silicon carbide substrates. If the two materials can be successfully integrated the material properties of the III-nitrides such as piezoelectricity and piezoresistivity could be exploited in transducer elements such as cantilevers or membranes in silicon microelectromechanical (MEM) devices. Depending on the thickness and composition of the AlGaN layer, polarization and strain in GaN/AlGaN structures generates electric fields leading to a two-dimensional electron gas (2DEG). A further reason for investigating this system is that unlike the previous systems investigated, it consists of thin films rather than quantum wells and dots, therefore does not suffer the same problems of quantum confinement or strain.

The bright field image can be seen in Figure 4-11a, which shows the Si (111) substrate followed by an AlN buffer layer, then the GaN and AlGaN thin films. The sample is aligned along the [1100] direction and faults can be seen running vertically through the material. An arrow indicates the interface between GaN and AlGaN as it is not clearly visible. Figure 4-11b shows the integrated Ga 3d signal from ε_2 and it is clear that there is a change in Ga intensity between GaN where Ga =100% of group III elements, and AlGaN where Ga has been calculated to be 90% of group the III elements. This is not in agreement with the growth data which suggests that Ga = 65% of the group III elements.

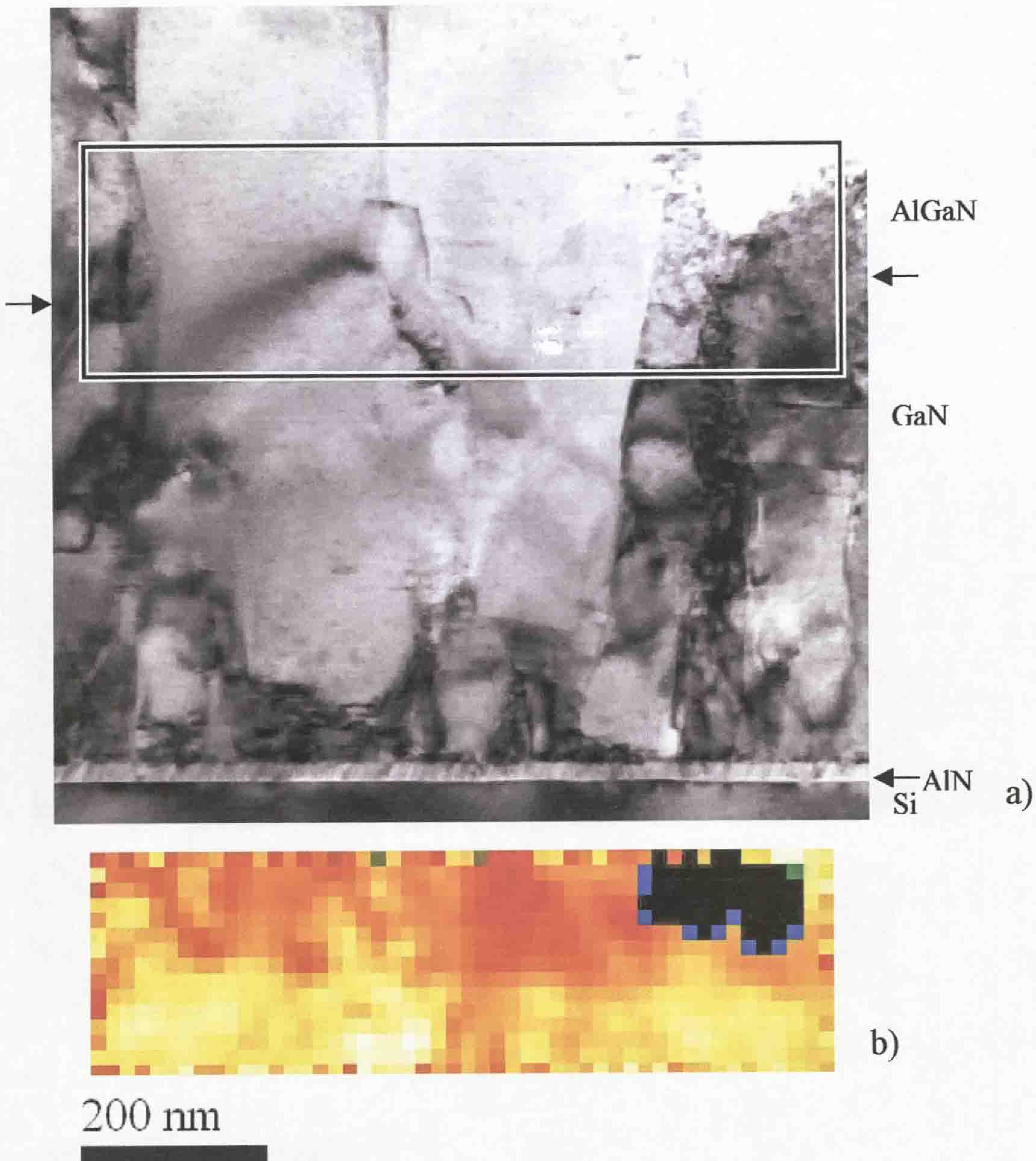

Figure 4-11. The bright field image of the GaN/AlGaN structure on a Si (111) substrate is shown in a), the arrows indicate the GaN/AlGaN interface. The EEL data was taken from the boxed region and the integrated Ga 3d signal can be seen in b).

4.3.4 Quantification of the composition of the group V elements in GaInNAs

As it has been seen in the previous section, using the absorption spectrum ε_2 can improve the accuracy of compositional information from the group III elements in comparison to the SSD. This approach is now applied to the N 2s and As 3d edges

which occur at around 16 and 41eV respectively. The N 2s edge is a very weak transition, and it also occurs in the region of the plasmon energy, making it impossible to observe in the SSD. Figure 4-12 shows the N 2s edge in ε_2 from several nitride materials, where N constitutes 100% of the group V elements. It is clear that even when the atomic percentage of nitrogen is high (50%), the edge intensity remains weak. It is also interesting to note the change in edge shape between the cubic and hexagonal GaN material. As the GaInNAs is a dilute nitride with N compositions reaching a maximum of 2 at% it is very unlikely that it will be possible to see the edge. However, by creating a map of the edge, fluctuations of N can be seen within the QW. A map of the integrated N 2s edge is shown in Figure 4-13a, from the same SI as was used in Figure 4-6 of a QW. As the concentration of nitrogen being investigated is low, the noise is of the same magnitude as the signal, thus as a single result it is of little significance. However, it is possible to verify the nitrogen distribution by looking at the As 3d to conduction band transition. Although the As 3d edge is larger, as it is situated at a higher energy loss it has poor signal-to-noise as the energy loss intensity drops off significantly and ε_2 tends towards zero. Figure 4-13b shows the integrated As 3d signal; the areas that show As depletion correlate closely with the N-rich regions.

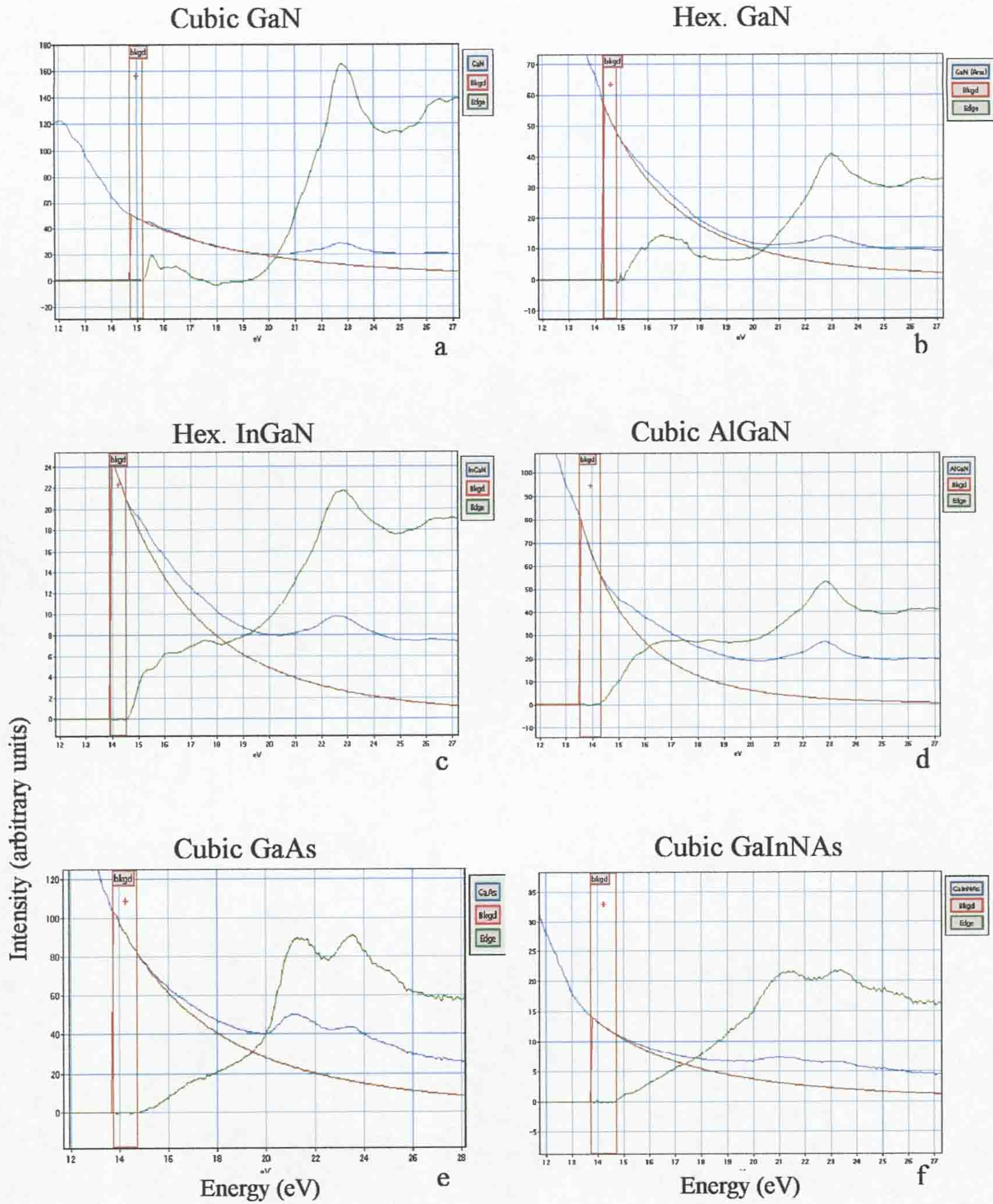

Figure 4-12 a-f illustrates N 2s edges in ε_2 from different N-containing III-V semiconductors where a is from cubic GaN, b hexagonal GaN, c hexagonal InGaN, d AlGaN, e cubic GaAs and f cubic GaInNAs. It can be seen that even when 50% of the specimen is nitrogen, the N 2s edge is very small.

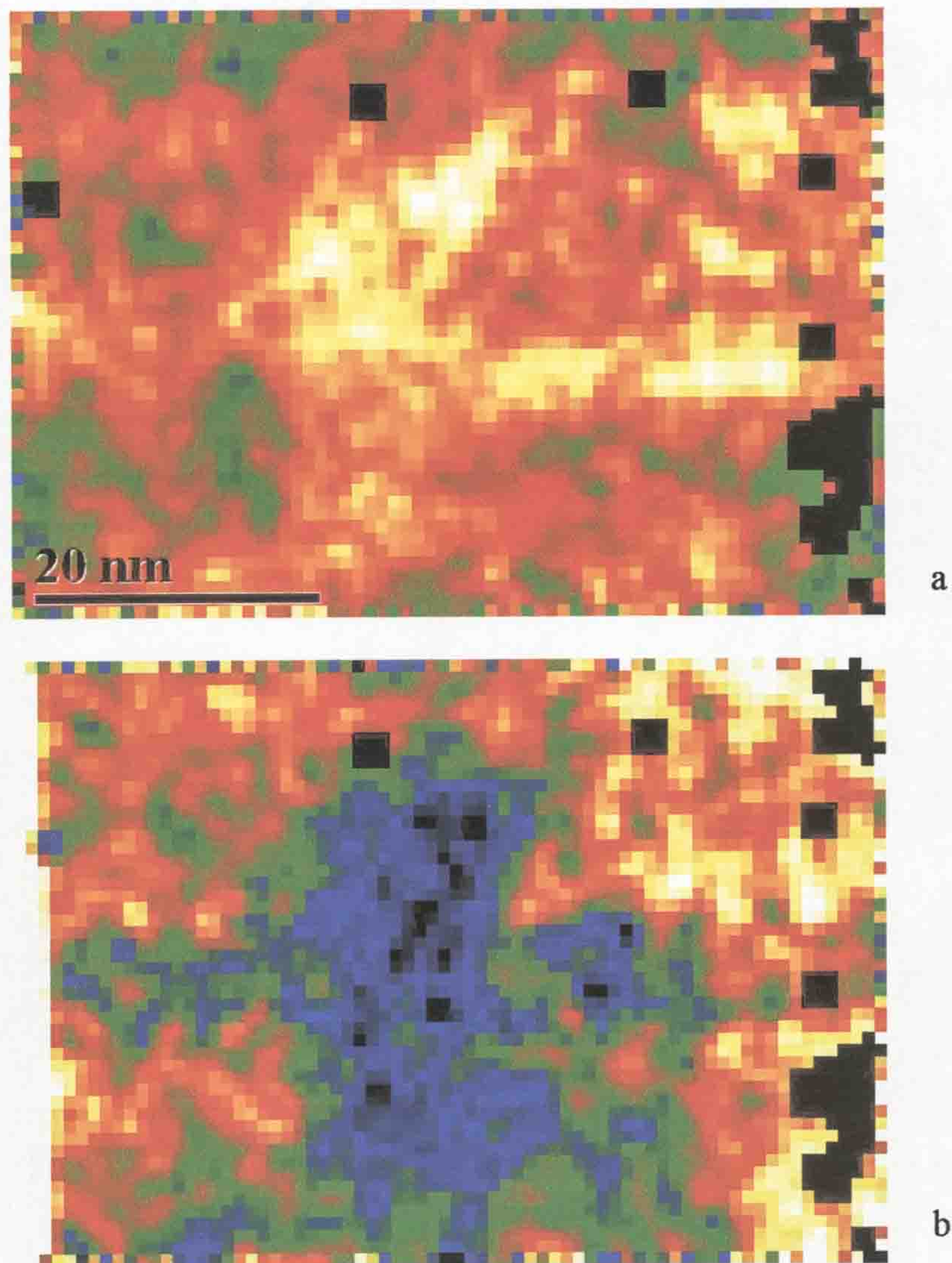

Figure 4-13a) the integrated N 2s edge from the ε_2 spectrum and b) the integrated As 3d edge. These maps are from the same SI taken from Figure 4-6 and can be compared with the Ga and In distributions.

Figure 4-14 shows the N 2s and As 3d maps taken from sample M1055 and corresponds to the maps in Figure 4-9. Although the statistics are poor it can again be seen that within the QW there is a decrease in As that corresponds with an increase in N. There is another effect that can be seen in all the elemental maps for M1055 outside of the QW region. On first inspection it seems to be due to carbon as it appears as a more intense area for both Ga and In. However, it is more likely to be due to strain. It appears as a more intense region to the right of the QW for all the elements with the exception of As where it appears as a reduction in intensity. A

further factor that prevents the quantification of the N signal is the possibility of other interband transitions occurring in the same energy loss region. A full understanding of all interband transitions that may occur in this energy region for GaInNAs must be understood and improved signal to background ratio must be achieved before quantification of the N 2s signal in dilute nitrides can be accomplished.

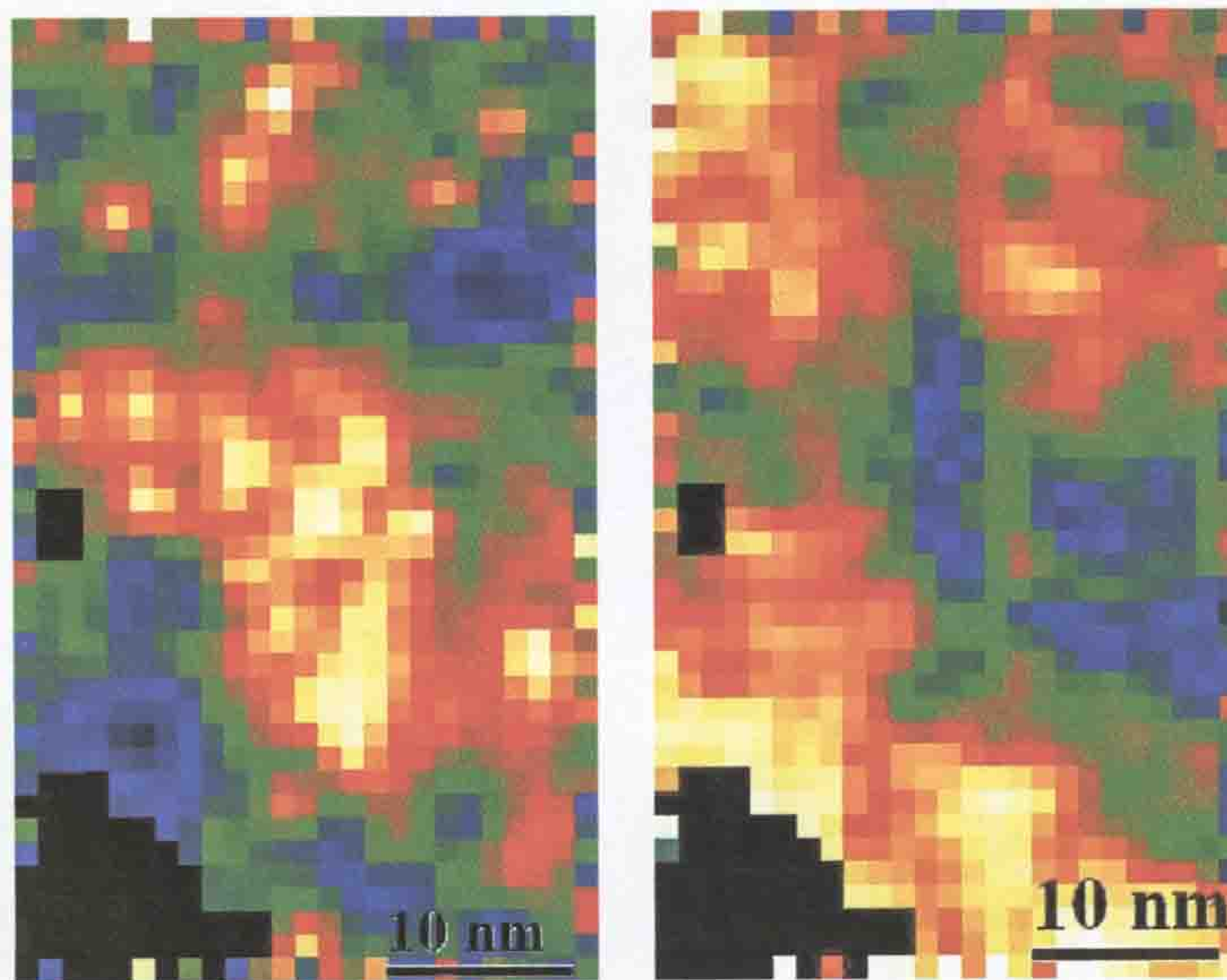

Figure 4-14. a) The N 2s signal and b) the As 3d signal are from the same data presented for the GaInNAs QW in Figure 4-9.

4.4 Discussion

The technique of using transitions in the first 50eV of the imaginary part of the dielectric function ε_2 to obtain elemental information from semiconductor specimens has been developed during this work. It has been shown that by using ε_2 instead of the SSD, the plasmon effect is removed, making the resulting data less complicated. Using ε_2 also allows for an improved background fit to the data and compositional results obtained are much clearer than those from the SSD. It has been shown that it is possible to quantify the compositional data from Ga, as the 3d transition that is

used is relatively large; this has produced very accurate results with a low standard deviation. Although it has only been possible to qualitatively investigate the other elements, it has been demonstrated that the N 2s transition can be mapped with N < 2at%. This technique allows for fast acquisition times compared with core-loss EELS reducing the possibilities of beam damage. The maps produced have a spatial resolution of ~0.8nm^2, slightly better than the resolution obtainable in EDX but have the advantage of allowing the lighter elements such as nitrogen to be analysed. The technique of using ε_2 to obtain compositional information proves to be very promising, and has been performed on a range of semiconductor materials. However, as a technique, it may be limited to specimens with only a few elements present as increasing the number of elements will increase the chances of transitions from different elements overlapping. For the same reasons it is also extremely important to minimise carbon contamination.

References

[1] R.F. Egerton, Electron Energy Loss Spectroscopy, Plenum Press, NY (1986)

[2] M.H. Gass, A.J. Papworth, T.J. Bullough, and P.R. Chalker, Ultramicroscopy, **101**, 257 (2004)

Chapter 5

Results: Plasmon energy and the effective electron mass

Section **Page**

5.1 Determination of the plasmon energy 115

5.2 Effective electron mass mapping 130

5.3 Discussion 138

5 Results: Plasmon energy and the effective electron mass

In the energy loss spectrum the plasmon peak is the most intense feature after the zero loss peak. It therefore requires minimal acquisition times to obtain spectra in this region, reducing the possibility of beam damage to the specimen or problems occurring from specimen drift. Due to the ease of acquiring the data, many researchers have studied the plasmon peak, looking at how the energy of its maximum (the plasmon energy), the full width half maximum, and its amplitude all change as various conditions are altered. It has been noted that these three parameters, especially the plasmon energy, change with the material. Simple equations using the plasmon energies of two binary alloys have been developed to calculate the plasmon energy of the ternary alloy. However, this technique has been limited to metal alloys. The development in the study of plasmon energies has been slow as the shift in plasmon energy is very small in comparison with the energy resolution, and research has traditionally concentrated on the use of core-loss edges. Until recently, EELS has also been limited to point analysis in the STEM, and although energy filtering TEM can produce an image of plasmon intensity, it cannot show the shift in position of the plasmon peak. With the increased energy resolution of energy-loss systems, combined with spectrum imaging, plasmon energy mapping is feasible and has become more routine. Another method of determining the plasmon energy, or frequency, is through determining the point at which the real part of the dielectric function, ε_1, crosses through zero with a positive gradient. In an electron gas, the condition for a plasma oscillation is that both ε_1 and ε_2 must equal zero and marks the transition from the reflecting to transmission region. When the plasma resonance occurs within a solid it is damped and the condition described can

no longer exist. As long as $\varepsilon_2 << 1$, the condition $\varepsilon_1=0$ can still be used to determine the plasmon energy, however it will generally by lower than the real value. In section 5.1 of this chapter, the two methods of determining the plasmon energy will be compared and discussed and the maps showing the effect of sample composition on plasmon energy will be presented.

The second half of this chapter, section 5.2 will investigate the plasmon energy and the *Kramers-Kronig* transformations to determine the number of electrons involved in the plasmon. This will then be used to calculate maps of the effective electron mass, m_e*. The effective electron mass is a very important parameter for semiconductor materials as it allows the electrons and holes to be treated as classically charged particles. A common method used to calculate m_e* is cyclotron resonance, producing a direct measurement. However, for GaNAs this has been limited to very low concentrations of N, and has not yet been possible for GaInNAs. Also, cyclotron resonance provides bulk analysis, which cannot show how the local composition variations affect m_e*. A reliable and direct method of determining m_e*, with the ability to map changes on a nanometre scale, could prove to be invaluable for advancing the understanding of many semiconductor materials, including dilute nitrides.

5.1 Determination of the plasmon energy

The following sections show how the plasmon energy varies with sample composition for GaInAs/GaAs QWs, GaInNAs/GaAs QWs, InAs/GaAs QDs, and AlGaN/GaN thin films. Both methods of determining the plasmon energy described in subsection 3.4.4.2 will be investigated; the measurement of the centre of the plasmon peak and the use of the condition $\varepsilon_1(E) = 0$.

5.1.1 Centre of plasmon peak

As defined in subsection 2.4.1, the free electron plasmon frequency (ω_p) is the plasmon energy divided by $\hbar$, so that:

$$E_p = \hbar\omega_p = \left(\frac{n_f \hbar^2}{m\varepsilon_0}\right)^{\frac{1}{2}} \qquad 5.1$$

and hence E_p is dependent on the number of free electrons, or valence electrons n_f. This relationship (5.1) is for free electrons and will be discussed again in subsection 5.1.3. Many of the plasmon energy values that are quoted in the literature are taken from the energy loss function, $Im[\varepsilon_2/(\varepsilon_1^2 + \varepsilon_2^2)]$, a reconstruction of the real and imaginary parts of the complex dielectric function calculated from the *Kramers-Kronig* relationships. The loss function can also be used to check that ε_1 and ε_2 have been accurately calculated, as it should be the same shape as the SSD. Examples of these two spectra are shown in Figure 5-1 for GaAs, where the loss function shows a very good fit to the SSD. For the loss function and the SSD to have a good

agreement, it is necessary that the ZLP be accurately removed from the EELS spectrum so that *Kramers-Kronig* transformations can be applied correctly. It is common that within a spectrum image there are several pixels that fail the KKA, often caused by an inadequate ZLP or poor signal-to-noise ratio. As the agreement between the loss function and SSD is good, and to avoid the failed pixels from the KKA, all plasmon peak energy values used in this study were taken from the SSD.

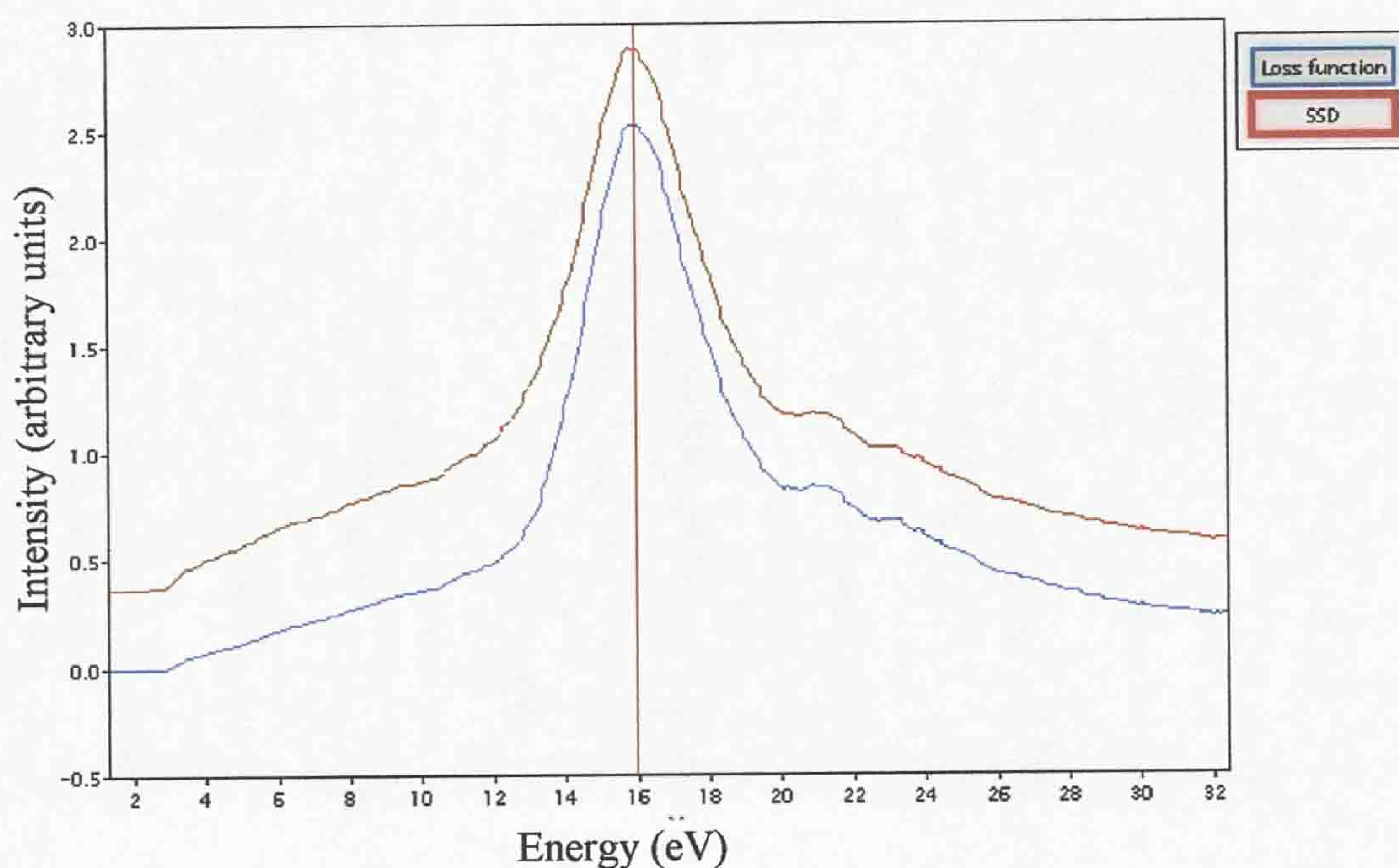

Figure 5-1 The reconstruction of ε_1 and ε_2 to give the loss function is demonstrated for GaAs (blue curve). It can be seen that there is no visible shift in plasmon peak energy from the SSD (red curve). Note that the SSD has been scaled in intensity to fit the loss function.

Firstly, the error in determining the plasmon energy has been calculated using maps of relatively large areas of GaAs from which typically 800 EELS spectra were recorded. From this large data set, the standard deviation of the fitted plasmon peak energy was observed to be 7meV. With such a small deviation in bulk material, it is feasible to measure the very small changes that are observed with sample composition. In order to show the sensitivity of the plasmon energy to different chemical environments Figure 5-2 shows the energy loss spectra from several III-V

semiconductor materials. The plasmon energy for GaAs is at 16.0 eV and that of GaN is 19.4 eV. It can be seen that the introduction of In to both GaAs and GaN reduces the plasmon energies, this is backed up by the accepted values for the plasmon energies of InAs and InN at 13.8 and 15.5 eV respectively.

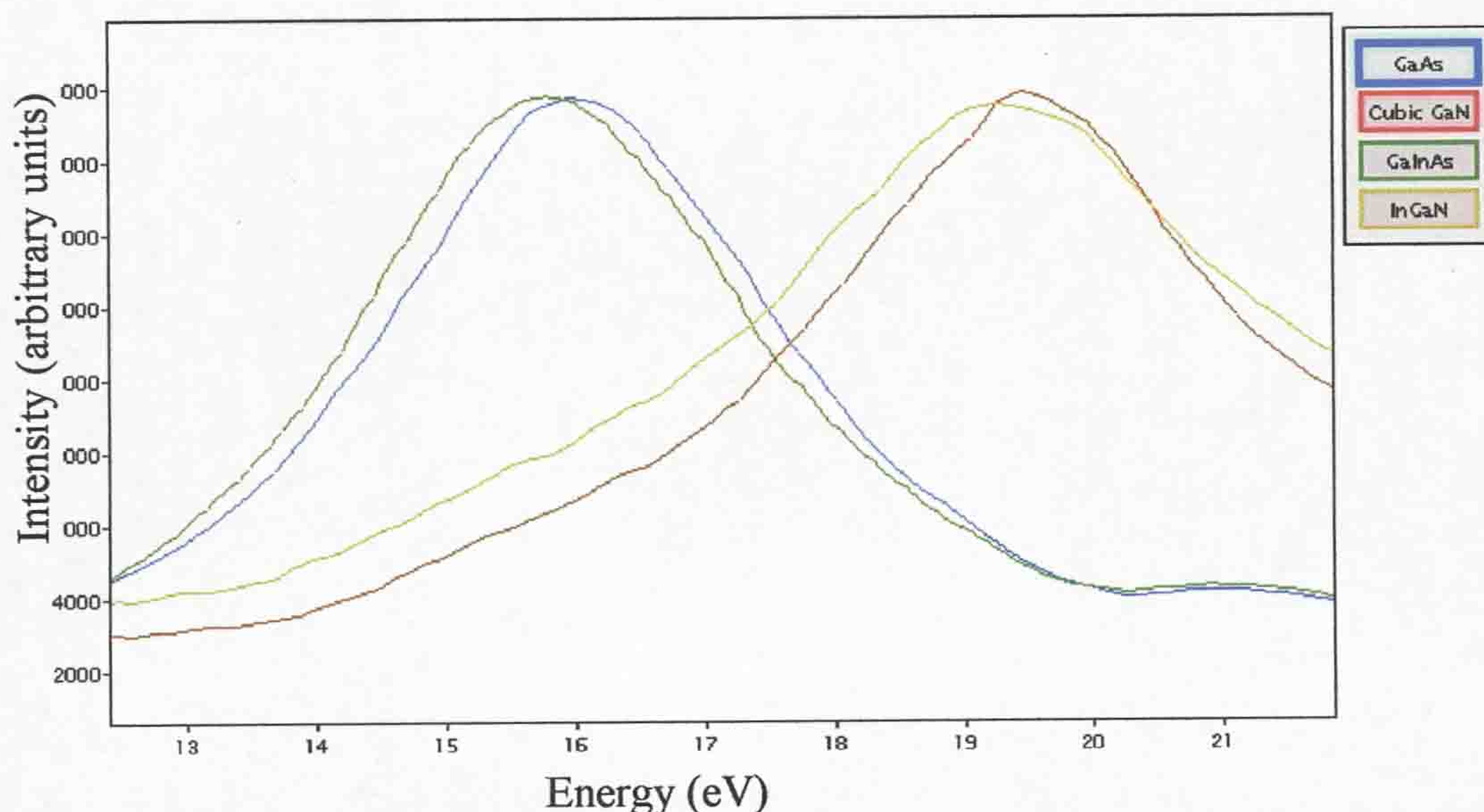

Figure 5-2 Plasmon energies from GaAs, cubic GaN and GaInAs (In fraction is 0.11 of the group III elements as estimated from PL data) and InGaN (In content not determined).

5.1.1.1 GaIn(N)As

Figure 5-3 shows the map of plasmon energy from sample FR1473, which contains a GaInAs QW and a GaInNAs QW. Nominally, both the quantum wells have the same In concentration, as shown in the elemental maps in Figure 4.7. Using PL data, the In group III fraction was determined to be 0.24 for the GaInAs QW. To calculate the N composition in the GaInNAs QW through PL it is assumed that the In concentration is the same as for the GaInNAs QW. It can be seen that on average the GaInAs QW has a lower plasmon energy (15.84eV) than the GaInNAs QW (15.88eV). This is expected, as the introduction of N is known to increase the plasmon energies of both GaAs and InAs (Table 5-1, section 5.1.3). Therefore with

a constant In composition, the introduction of N into GaInAs would be expected to increase the plasmon energy.

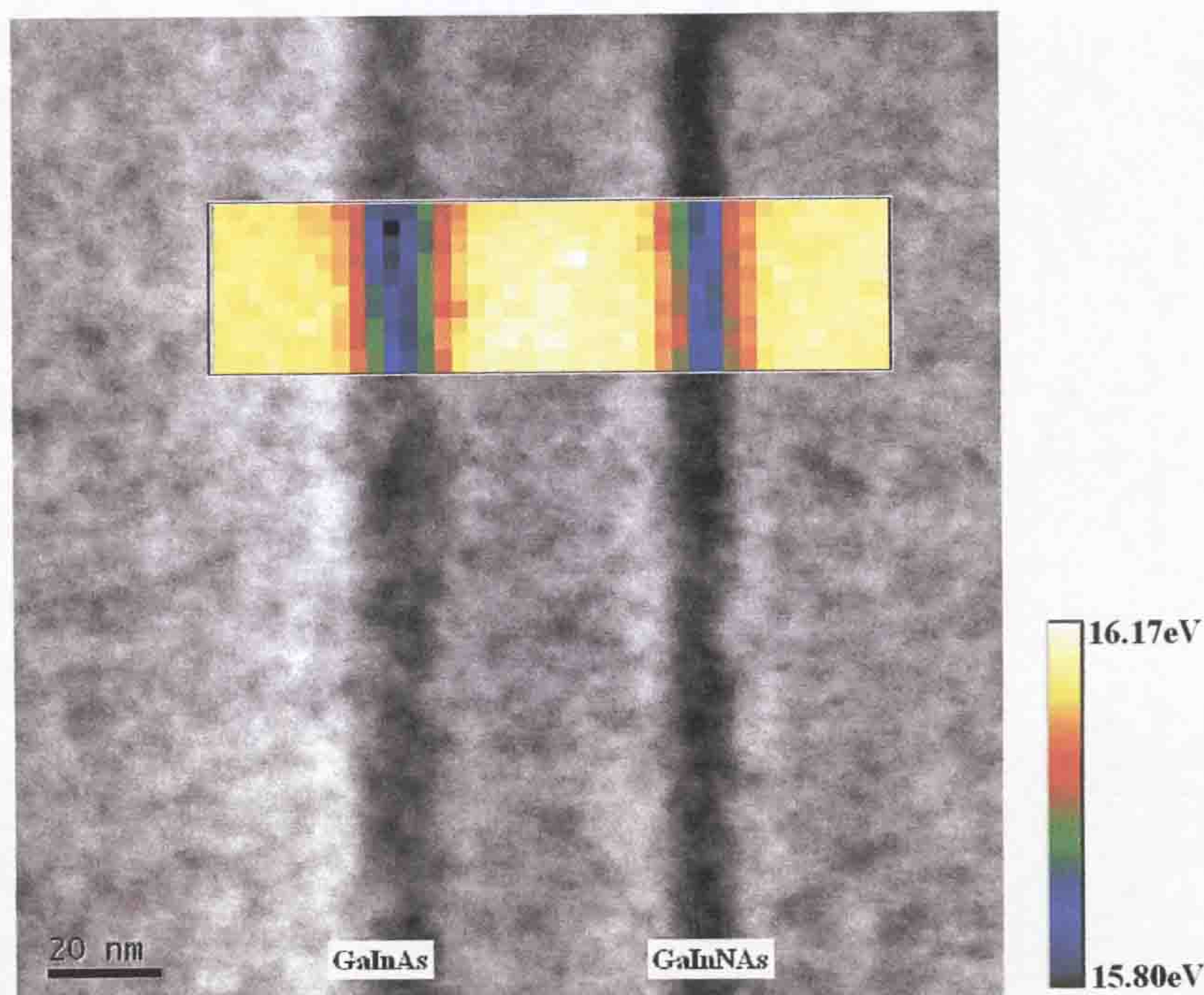

Figure 5-3. A STEM bright field image from sample Fr 1473 with a map of the plasmon peak centre superimposed onto the analysed area. The average value for GaAs plasmon energy is 16.13, for the 10nm GaInAs QW 15.84 and for the 6nm GaInNAs QW 15.88eV.

By contrast, examination of Figure 5-4 shows that for sample M1055 the GaInAs QW has a higher average plasmon energy (15.90eV) than the GaInNAs QW (15.79eV). The In fraction for both the QWs should have been 0.30 from the growth parameters used assuming In incorporation does not change with growth temperature or N flux. However, PL indicates the In fraction to be 0.18 for the GaInAs QW and there was no PL emission from the GaInNAs QW. It can be seen from the compositional analysis in Figure 4.9 that there is a significantly increased In concentration in the GaInNAs QW compared to the GaInAs QW. The reduced plasmon energy in the GaInNAs QW compared to the GaInAs QW is therefore probably due to this large increase in In concentration, where the opposing effect of

the addition of a comparatively small amount of N on the plasmon energy has been obscured.

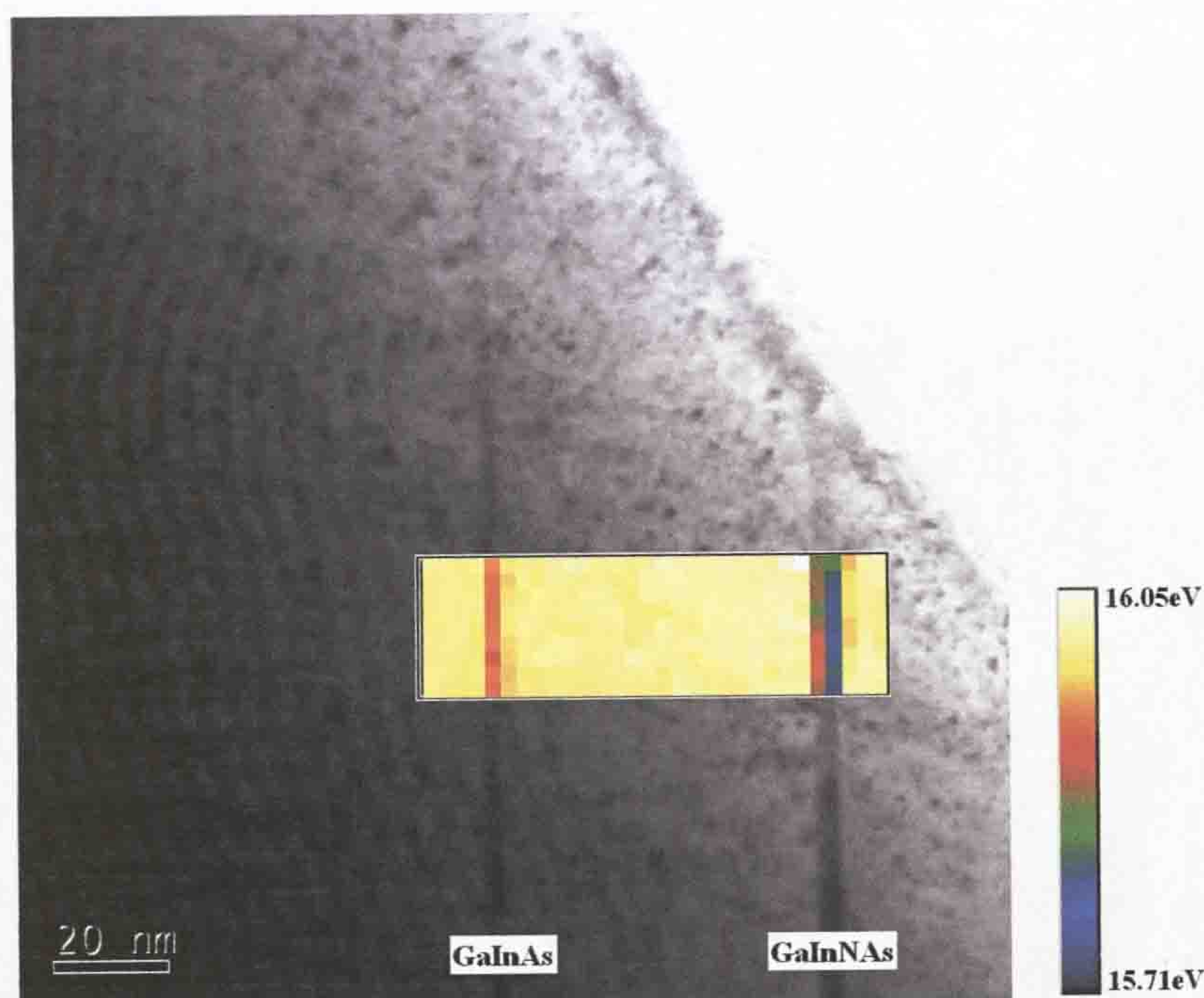

Figure 5-4. A STEM bright field image from sample M1055 with a map of the plasmon peak centre superimposed onto the analysed area. The average value for GaAs plasmon energy is 15.99, for the 3nm GaInAs QW 15.90eV and for the 7nm GaInNAs QW 15.79eV.

Figure 5-5 shows the variation in plasmon energy across a whole GaInNAs QW laser structure grown on GaAs with AlGaAs cladding layers (shown pictorially in Figure 4-4, with its structure detailed in Table 4-3). It shows the plasmon energy mapped at increasing magnifications. The QW shows a shift to lower energies but appears non-uniform, which was discussed previously in subsection 4.3.1. The reduction of plasmon energy in AlGaAs (16.01eV) compared to GaAs (16.08eV) agrees with results obtained from M1058, an undoped laser structure with a lower Al fraction in the AlGaAs. However, the value for E_p (AlAs) determined by *Ludeke et al*[1] is 16.1eV, higher than the 16.08eV value for GaAs found in this study, this discrepancy could be due the energy resolution available when *Ludeke et al* carried

out their research in 1975. No other values for the bulk plasmon energy of AlAs or AlGaAs have been found in the literature. The AlAs plasmon energy calculated using the free electron formula is the same as that for GaAs (to 1d.p.).

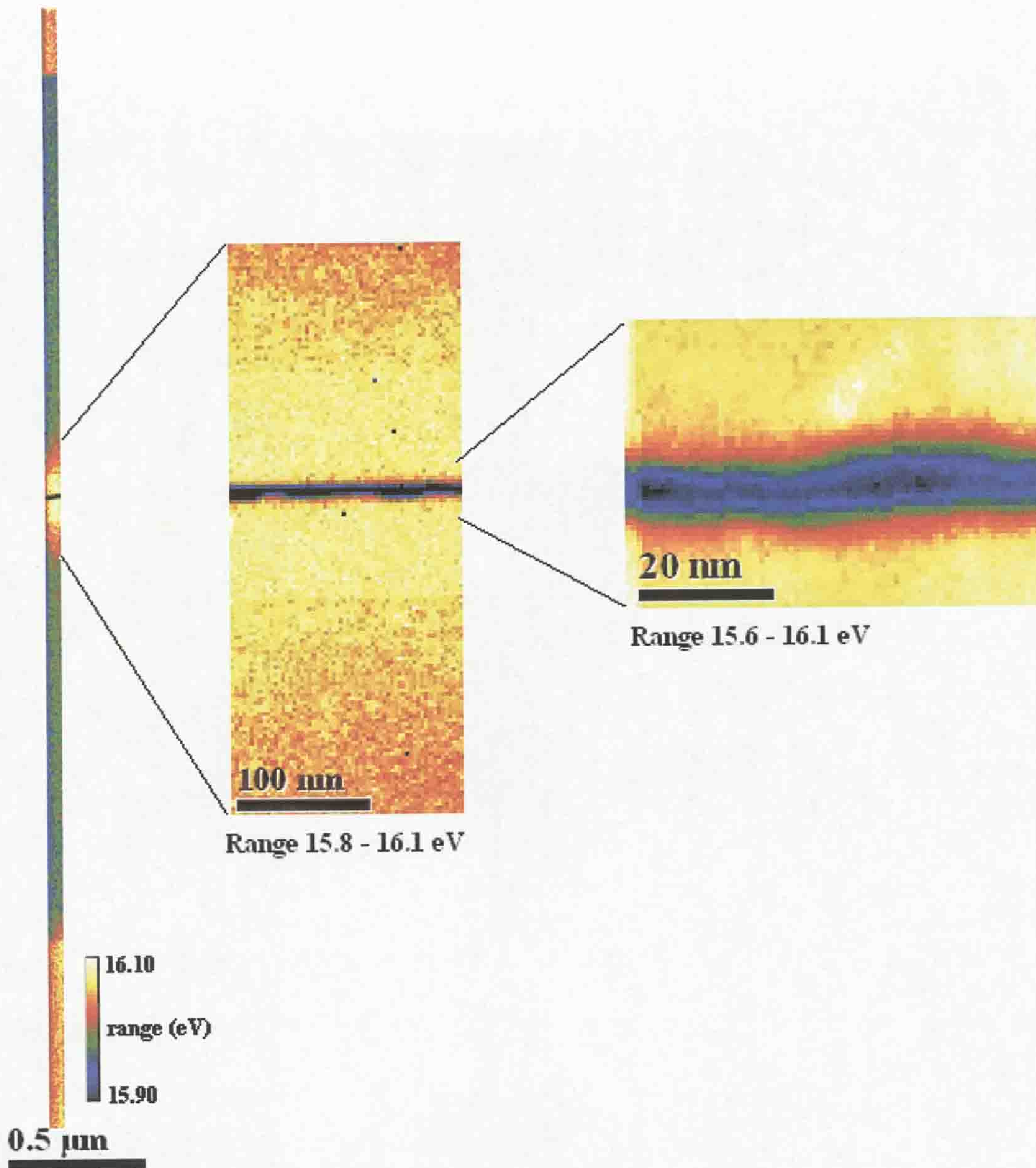

Figure 5-5 The mapped areas show at increasing magnifications the change in centre of the plasmon peak in eV for the Fr1485 laser structure The average values for the different layers are: GaAs 16.08 eV, AlGaAs 16.01 eV and GaInNAs QW 15.66 eV.

5.1.1.2 InAs QDs

The results presented in this section are based on the same InAs QD data analysed in subsection 4.3.2. The plasmon energy has been determined from the SSD, and is shown in Figure 5-6b. It shows the map of the plasmon energy over the region indicated in Figure 5-6a. The change in intensity across the GaAs region from top to bottom of the map is attributed to carbon contamination. This is also indicated in the higher than expected plasmon energy for GaAs of ~16.2eV as the carbon $\pi+\sigma$ plasmon lies at a higher energy than that of GaAs, resulting in an apparent upwards shift in energy of the centre of the GaAs plasmon. A decrease in energy to 15.80eV is clearly seen where the QDs are located. This decrease in energy is expected as the introduction of In to GaAs reduces the plasmon energy, as discussed in the previous subsection 5.1.1.1, but is not as large as expected for InAs. *Nakashima et al*[2] have suggested that the plasmon energy of CdS increases with the decrease in particle size, attributing it to quantum confinement. Although quantum confinement of the InAs QDs could also cause an increase in the expected plasmon energy, the small decrease in plasmon energy could be attributed to the thickness of the specimen. As the specimen is ~80nm thick (calculated from *Kramers-Kronig* analysis), and assuming that there is only one InAs QD in the analysed area with a diameter of 18nm, the average composition sampled will be $Ga_{0.8}In_{0.2}As$. It is also noted that the plasmon energy map, as with the elemental maps in subsection 4.3.2, does not show the QDs to be circular in their cross-section.

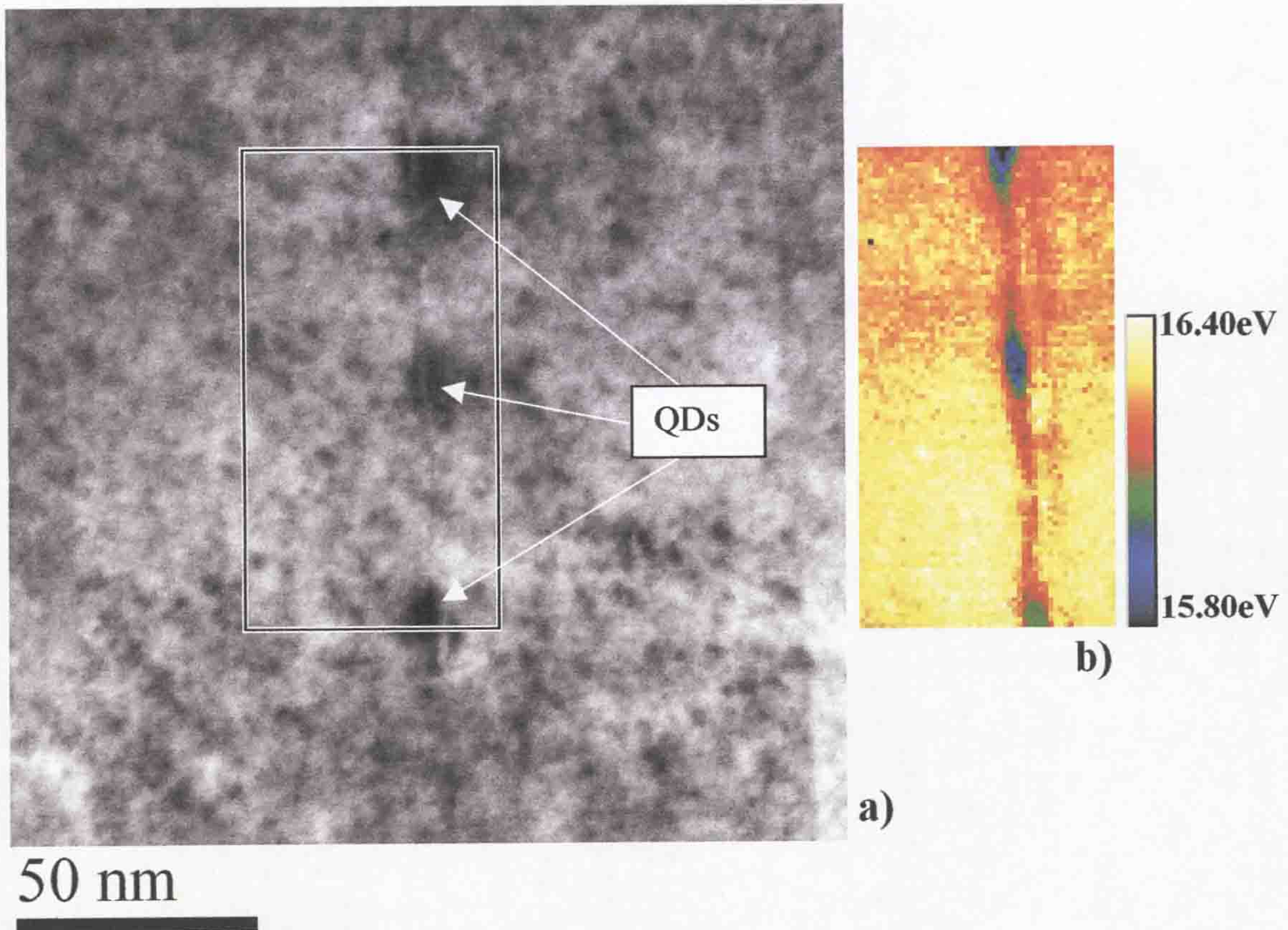

Figure 5-6. The bright field image of InAs QDs can be seen in a) and the plasmon energy taken from the boxed region is shown in b).

5.1.1.3 AlGaN/GaN

A bright field image of a wurzite AlGaN/GaN sample can be seen in Figure 5-7a. The cross-section shows the Si (111) substrate followed by an AlN buffer layer, then the GaN and AlGaN thin films. Arrows indicate the GaN / AlGaN interface. The sample is aligned along the [1100] direction and faults can be seen running vertically through the material. The plasmon energy map is shown in Figure 5-7b, where the interface is very clear and it can be seen that E_p for AlGaN is higher than that of GaN. The GaN has an average E_p value of 19.42eV, which is in agreement with measurements from other groups[3,4] and the AlGaN has a plasmon energy of 19.57eV, which is reasonable when compared with the higher AlN plasmon energy of ~21.2eV[4].

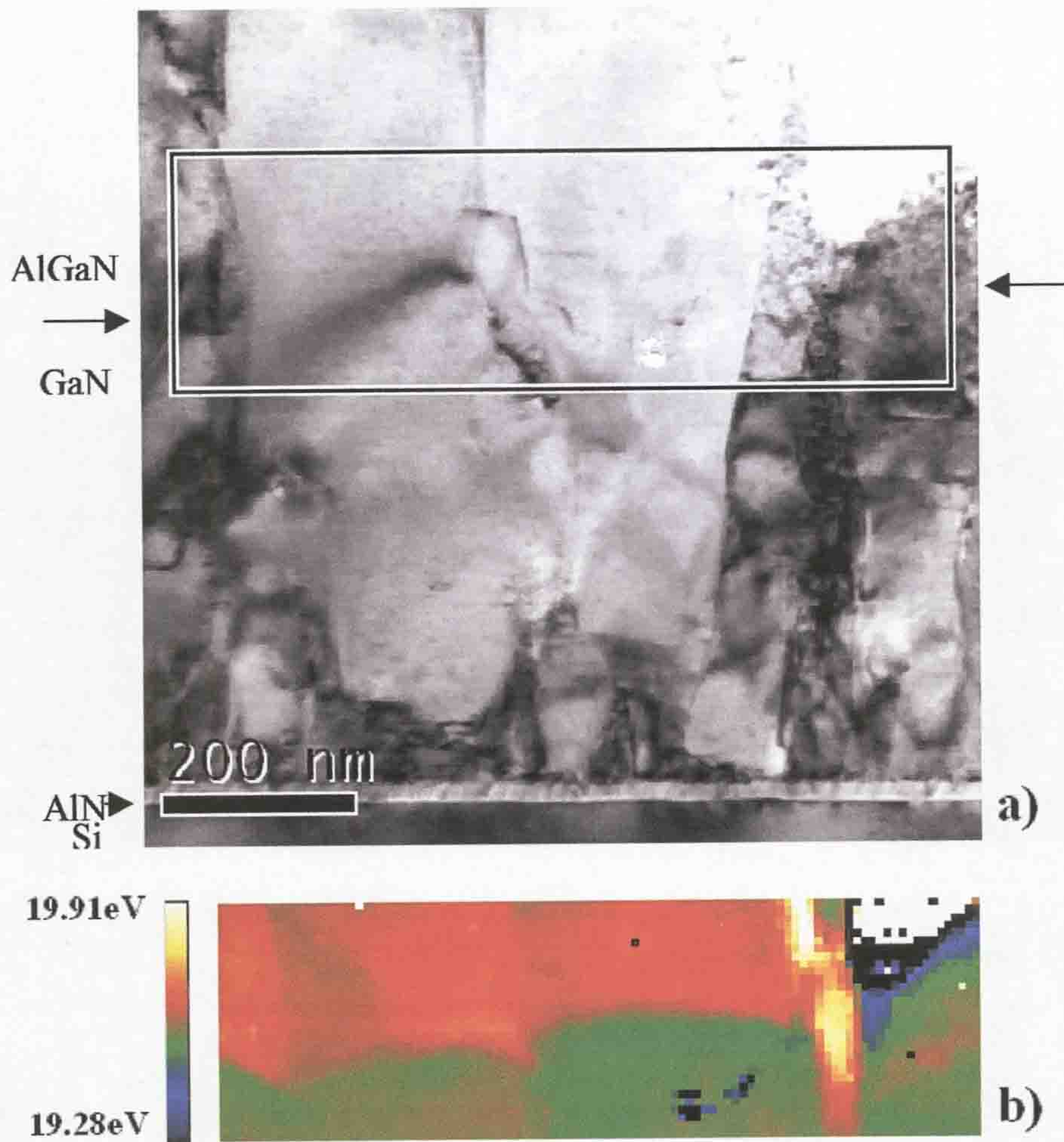

Figure 5-7. The bright field image of the GaN / AlGaN structure is shown in a) and the plasmon energy from the boxed region in b). The average plasmon energies are 19.42eV for GaN (green) and 19.57eV for AlGaN (red).

In subsection 4.3.3, the generation of a 2D electron gas resulting from the polarisation and strain in the GaN/AlGaN structure was discussed. In columnar structured GaN layers, mixed polarities have been observed by convergent beam electron diffraction[5], and this would tend to cancel out the formation of an extended 2DEG. The contrast in the plasmon frequency map shown in Figure 5-7 seems to reflect this model, which is apparent from the colour variations across the columnar boundaries.

5.1.2 Calculation of the plasmon energy from the condition $\varepsilon_1 = 0$

For semiconductors, the condition $\varepsilon_1 = 0$ occurs twice. A spectrum of $\varepsilon_1(E)$ is shown in Figure 5-8 for GaAs.

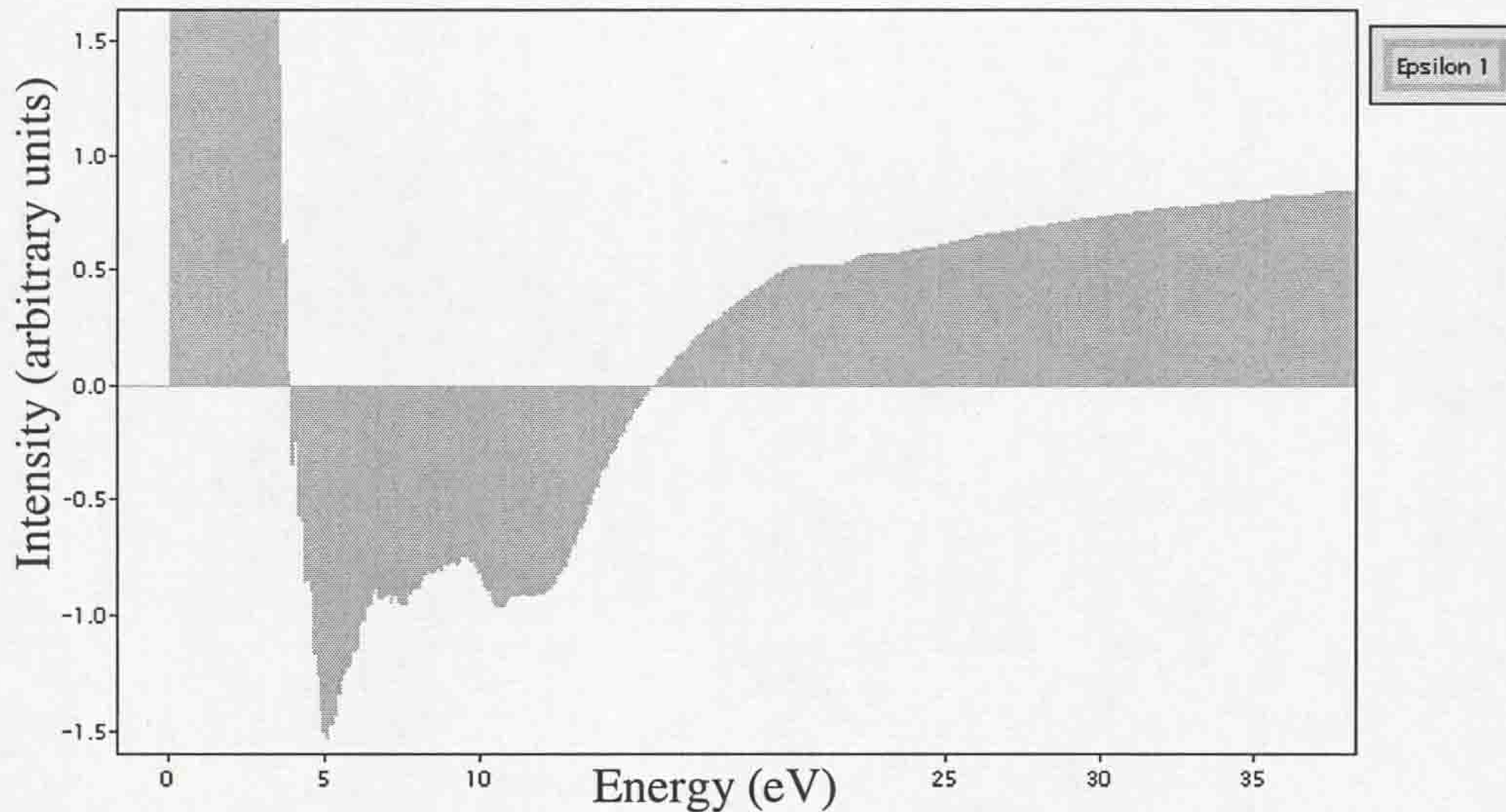

Figure 5-8. A spectrum of $\varepsilon_1(E)$ for GaAs, showing the two points at which $\varepsilon_1 = 0$.

The first crossing of zero occurs with a negative gradient and is equal to the band gap at the *X*-point in the Brillouin zone, E_2. The second crossing of zero at higher energies is at the plasmon energy, assuming there is no damping of the plasmon. When damping occurs, for example due to crystal boundaries or strain, the energy at which ε_1 passes through zero decreases. This may be useful, as following this argument, changes in strain could be observed by calculating the difference between the two plasmon energies (at the centre of the plasmon peak and at ε_1=0). A map of the energy at which ε_1 passes through zero is shown for a QW sample in Figure 5-9, using the same raw data as for the plasmon energy (SSD) maps for the QW in Figure 5-5c. The script used to calculate the energies (Appendix B1) only calculates to the same resolution as the energy dispersion chosen to acquire the data. As 0.1 eV per channel was used for this GaInNAs QW, the map of ε_1=0 will show the results to the

nearest 0.1 eV and is therefore not as detailed as that determined from the plasmon peak. However, it does show structure within the QW that is similar to E_p in Figure 5-5c, but at slightly lower energies. By subtracting the map of ε_1=0 from the map of the centre of the plasmon, the resulting map, shown in Figure 5-9b shows the difference between the two methods. The average difference over the GaAs regions is 0.22eV while within the QW the average difference is 0.24eV. As the energy resolution for ε_1=0 is poor a lot of the information lost.

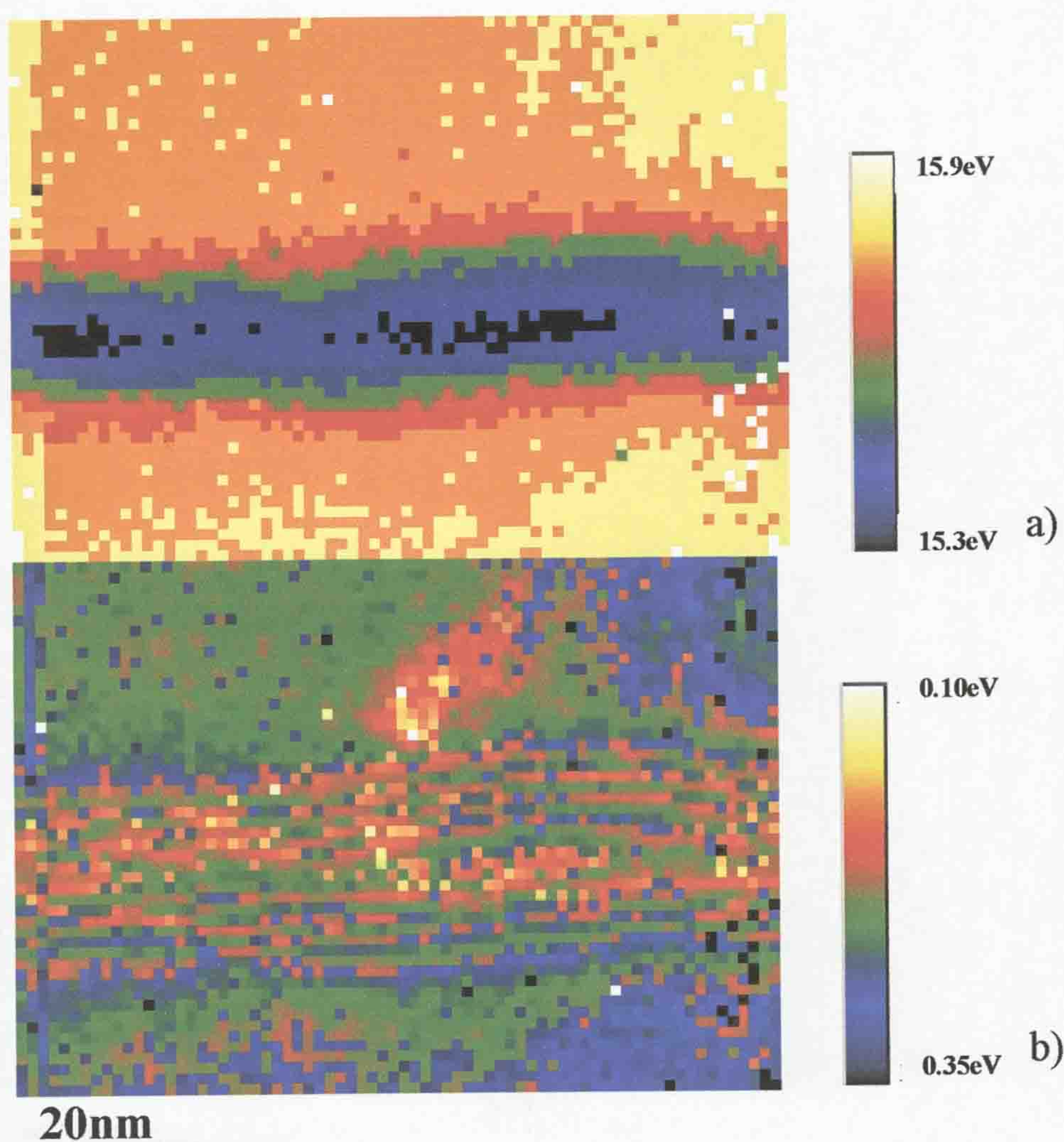

Figure 5-9.a) the plasmon energy of a GaInNAs QW measured by taking ε_1=0, the average value for GaAs is 15.8eV, and b) the difference in energy between the plasmon peak centre and ε_1=0. The maps are calculated from the same data as Figure 5-5c.

Figure 5-10a shows the condition $\varepsilon_1=0$ for the InAs QDs. For this data the energy dispersion was 0.05eV per channel, therefore the values in map $\varepsilon_1=0$ are calculated to the nearest 0.05eV, allowing for a greater energy resolution than for the GaInNAs QW previously. Again, an increase in energy difference between the two methods of calculating the plasmon energies can also be seen in the region of the InAs QDs in Figure 5-10b, with average differences of 0.37eV and 0.59eV for the GaAs bulk and InAs QD respectively. An increase in energy difference between the plasmon peak centre and $\varepsilon_1=0$ has also been observed within the QWs of GaN/GaInN multiple QWs[6].

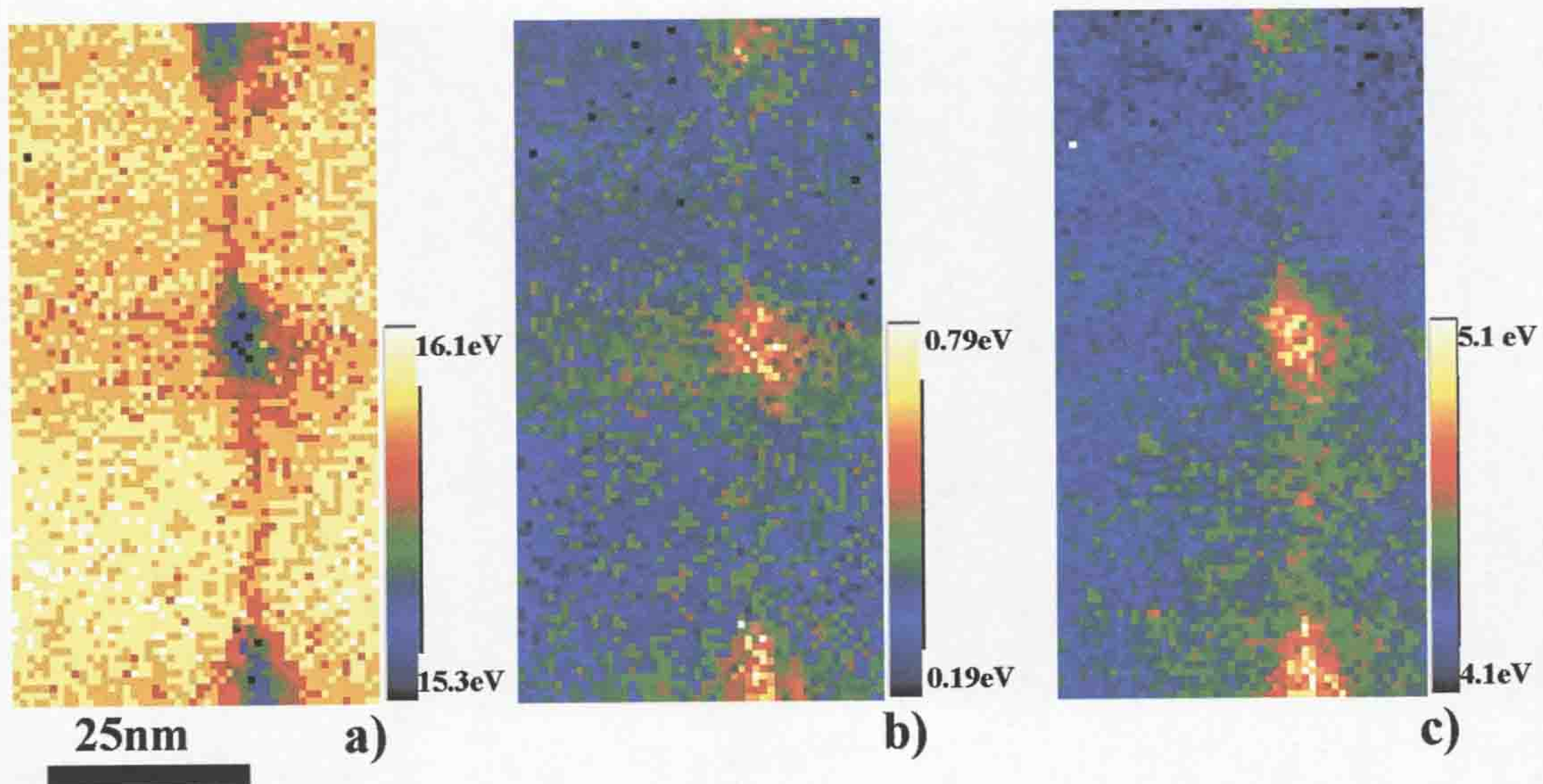

Figure 5-10 a) The plasmon energy from $\varepsilon_1=0$ and b) the difference in plasmon energies for InAs QDs, calculated from the same data as Figure 5-6b and c) the FWHM from the plasmon peak centre.

It is apparent that the difference between the two calculated plasmon energies within QWs and QDs always increases, independent of the elements present. It is also noted that the greatest difference was calculated within the QDs. This indicates that the observed effect may be due to strain, and the greater the strain, the greater the difference between the centre of the plasmon peak and the condition $\varepsilon_1=0$. This is in

agreement with the discussion in section 3.4.3, which states that the condition ε_1=0 is the plasmon energy assuming that the plasmon has not suffered any dampening.

It has previously been determined[7] that the full width half maximum (FWHM) of the plasmon peak in $Im(-1/\varepsilon)$ is equal to $\hbar/\tau$, where the relaxation time $\tau = 1/\Gamma$ and Γ is the damping constant. Therefore the FWHM of the plasmon contains information about the damping of the plasma oscillation. Γ is strongly influenced by the band structure of the solid and by the grain size[10]. The smaller the grains in a material, the greater the FWHM as plasma oscillations are dampened when crossing grain boundaries. Using this argument, it follows that strain within a material will also dampen the oscillations, widening the FWHM. The FWHM from the plasmon peak of the InAs QDs can be seen in Figure 5-10c and shows very similar contrast to the Figure 5-10b, increasing through the QDs, further evidence that strain can be observed through the difference between the plasmon peak centre and ε_1=0.

5.1.3 Free electron calculations

Table 5-1 shows the theoretical plasmon energies calculated from the free electron formula Equation 5-1, where n (the only variable) is the number of electrons participating in the plasmon per m^3. It assumes that all valence electrons (and no others) participate in determining the plasmon energy. Table 5-1 also shows experimental values taken from the SSD and ε_1 from this work and other studies. The free electron formula gives a good approximation for the non N-containing binary compounds. However, the formula breaks down when N is introduced, as the Ga 3d states with a free-atom local-density approximation (LDA) energy of -20.0eV are in near resonance with the N 2s states (part of the lower valence band for In-V

and Ga-V compounds) with a free-atom LDA energy of (-)18.37eV. The proximity of these energies can be seen in Figure 5-11, which shows the energies for several III-V compounds. Due to the proximity of the energies, a resonance of the Ga 3d orbitals with the N 2s states is expected to affect the valence band[8]. This can lead to several features of III-N compounds such as band structure, charge density and density of states resembling II-VI materials, whose d-states lie within the valence band. The effect of the Ga 3d orbitals is not a consideration when looking at the conventional III-V arsenides (i.e. non N-containing) as they lie below the valence band in the band structure calculations. This comparison is shown in the band structures for GaAs and GaN which include the Ga 3d bands in Figure 5-12.

Table 5-1 Experimental and calculated plasmon energies.

Material	Valence electrons (e^- /m^3)	E_p eV (SSD)	E_p eV (ε_1=0)	E_p eV (Equation 5.1)
GaAs	4 x 4.42 x 10^{28}	16.0	15.8	15.6
GaN	4 x 8.89 x 10^{28}	19.43	19.23	22.1
InAs	4 x 3.59 x 10^{28}	13.8*[1]		14.1
InN	4 x 6.4 x 10^{28}	15.5**		18.8
AlAs	4 x 4.41x 10^{28}	16.1***		15.6

* It is unclear whether this result has been taken from a plasmon peak or ε_1.
** Value taken from *Mkhoyan et al*[9]
*** Value taken from *Ludeke et al*[1]

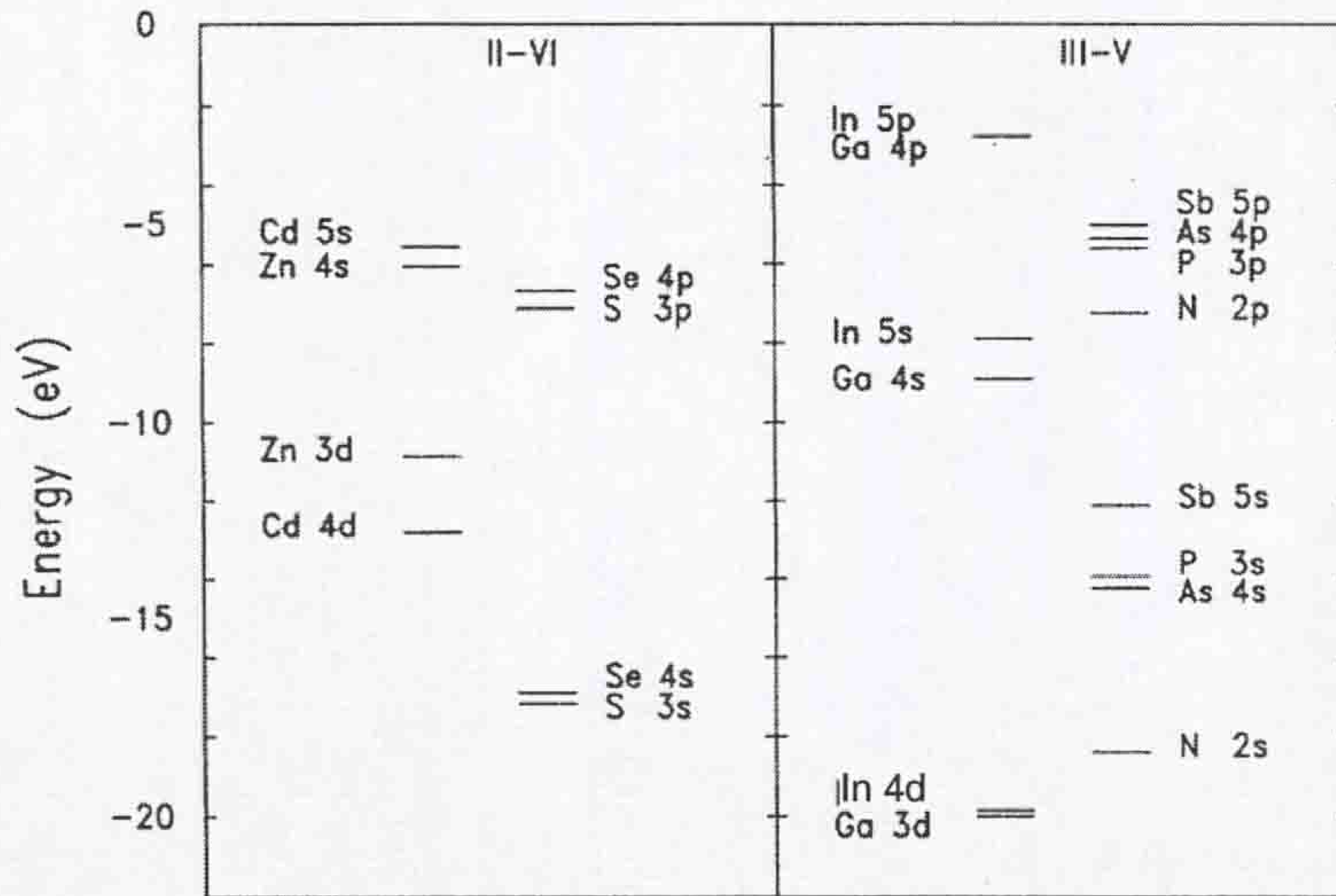

Figure 5-11. The non-relativistic free-atom LDA energies for some II-VI and III-V compounds. Taken from *Fiorentini et al*[8].

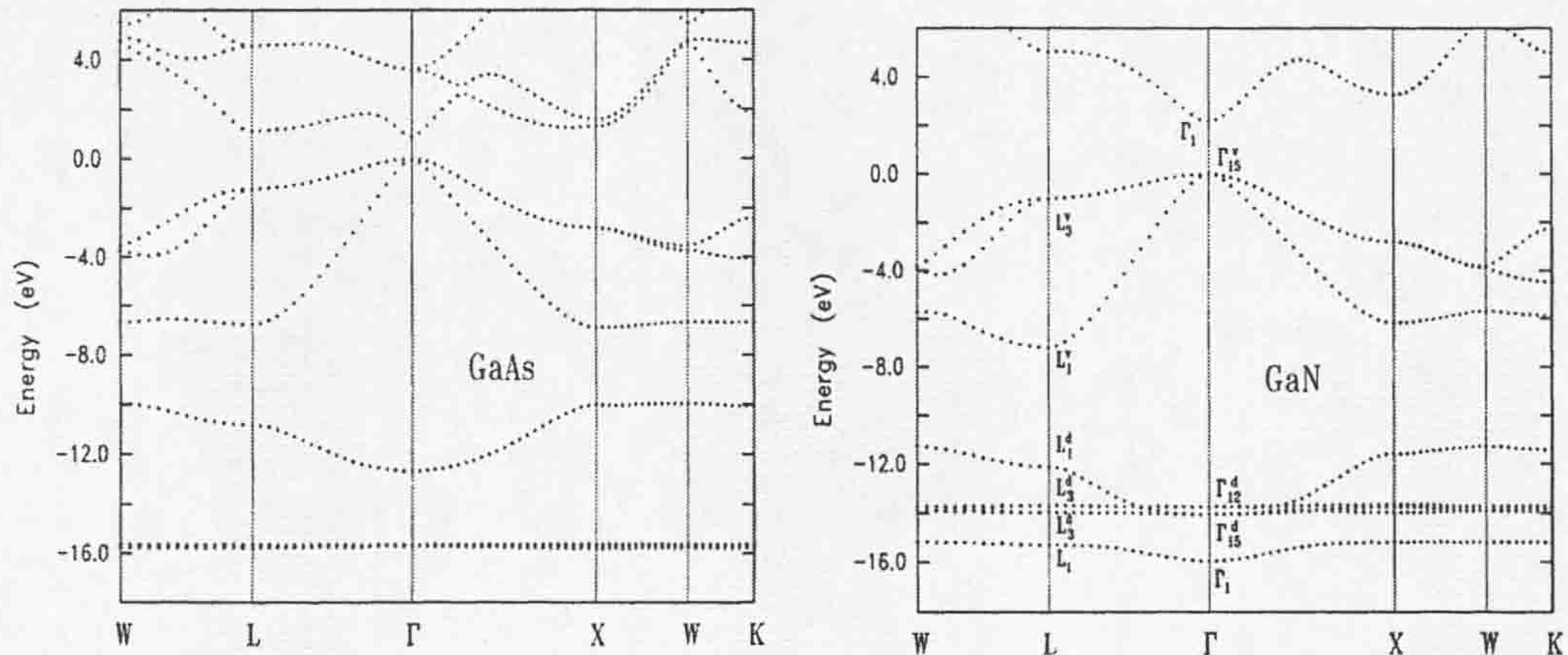

Figure 5-12 the band structure of a) GaAs with the d-bands well below the valence states, and b) GaN, where the d-bands are at the bottom of the valence band. The energy zero is the valence-band top. Taken from *Fiorentini et al*[8].

There are several equations that have been used to take into account the effect of bound electrons, or the damping effect on the plasmon such as

$$\varepsilon_1(0) = 1 + \left(\frac{E_p}{E_g}\right)^2 \tag{5.2}$$

where E_p is the free electron plasmon and E_g is the average optical gap (sometimes defined as E_2 , the band-gap at the *X*-point of the Brillouin zone)[10,11]. However it is generally the case that they work for one system and not others (e.g. those where the

core electrons interact with the valence electrons). Much more work must be carried out on the theory of plasmon excitations especially in cases when it no longer conforms to the free electron model in order that it is possible to calculate the plasmon energy of any semiconductor. To do this a greater understanding of plasmon excitations and the effect of semi-core electrons and band gaps on the system is needed. This understanding may be obtained through the practical study of plasmons. It is a technique that is coming back into interest, resulting from the increased energy resolution available and the ability to acquire low-loss spectrum images quickly.

5.2 Effective electron mass mapping

5.2.1 GaInNAs QWs

Figure 5-13b shows a map of the variation in effective electron mass over a GaInNAs QW laser structure (Fr1485). The effective electron mass (m_e*) has been calculated using the same data as in the plasmon energy map in Figure 5-5c, and the elemental composition maps in Figures 4-6 and 4-13. The bright field image of the cross-section sample has been presented again for clarity in Figure 5-13a. Figure 5-13b is a false colour map of m_e* using the plasmon energy shown in Figure 5-5c and the effective number of electrons calculated through *Kramers-Kronig* analysis. The method used to calculate m_e* is described in subsection 3.4.5.6. The incorporation of N into GaAs has the effect of increasing m_e*[12,13] and it can be seen that within the QW, m_e* increases more in certain areas. The variation of m_e* along and across the QW is attributed to the fluctuating elemental composition within this QW as observed in section 4.3.1 for this sample.

Referring back to Equation 3-9 ($m_e^* = \frac{n\,\hbar^2}{E_p^2 \varepsilon_0 \varepsilon_\infty}$), it should be noted that ε_∞ is assumed to be constant over all points in the map of Figure 5-13. However ε_∞ does increase slightly with the introduction of In to GaAs, and decreases when N is introduced into GaAs[14]. For a uniform GaInNAs QW, the opposing effects of In and N on ε_∞ experienced within the QW could make ε_∞ effectively a constant for this system. It can also be determined from Equation 5-1 that for GaInNAs, as E_p decreases within the QW and the increase in m_e* is due to the N, the number of electrons involved in the plasmon n must therefore increase in the N-containing regions. The increase in n can be explained by the effect of the N 2s electrons. The N 2s electrons are part of the lower valence band for In-V and Ga-V compounds with a free-atom LDA energy of (-)18.37eV, whilst the Ga 3d and In 4d states have a free-atom LDA energy of (-)20.0eV and (-)19.8eV respectively[8]. Due to the proximity of the energies, a resonance of the Ga 3d and In 4d orbitals with the N 2s states effects the valence band. This results in an overall increase of valence electrons, as has been determined here. An average effective electron mass of $0.078m_0$ from regions determined to be N-rich In the $Ga_{0.65}In_{0.35}N_{0.01}As_{0.99}$ well and $0.075m_0$ from the GaAs substrate have been calculated. The electron effective mass of a GaInAs alloy of comparable composition would be predicted to be $0.0527m_0$ according to the relationship, m_e*($Ga_xIn_{1-x}As$) = $0.026+(0.041x)m_0$[15,16]. A number of groups have investigated the influence of composition in dilute nitrides upon m_e*[17,18,19,20,21,22,23,24]. This observation is in agreement with these studies which generally indicate that the incorporation of nitrogen into GaAs or GaInAs increases m_e*. For GaInNAs, the magnitude of the reported increase varies significantly between studies. Most experimental values of m_e* have been obtained using indirect

methods such as through the analysis of the carrier confinement energies[17,18,20]. Direct measurements of m_e* using cyclotron resonance has been limited to GaNAs with very low nitrogen concentration[19]. The approach developed here enables variations in m_e* to be mapped in semiconductor device structures and provides a direct measurement of m_e* in GaInNAs.

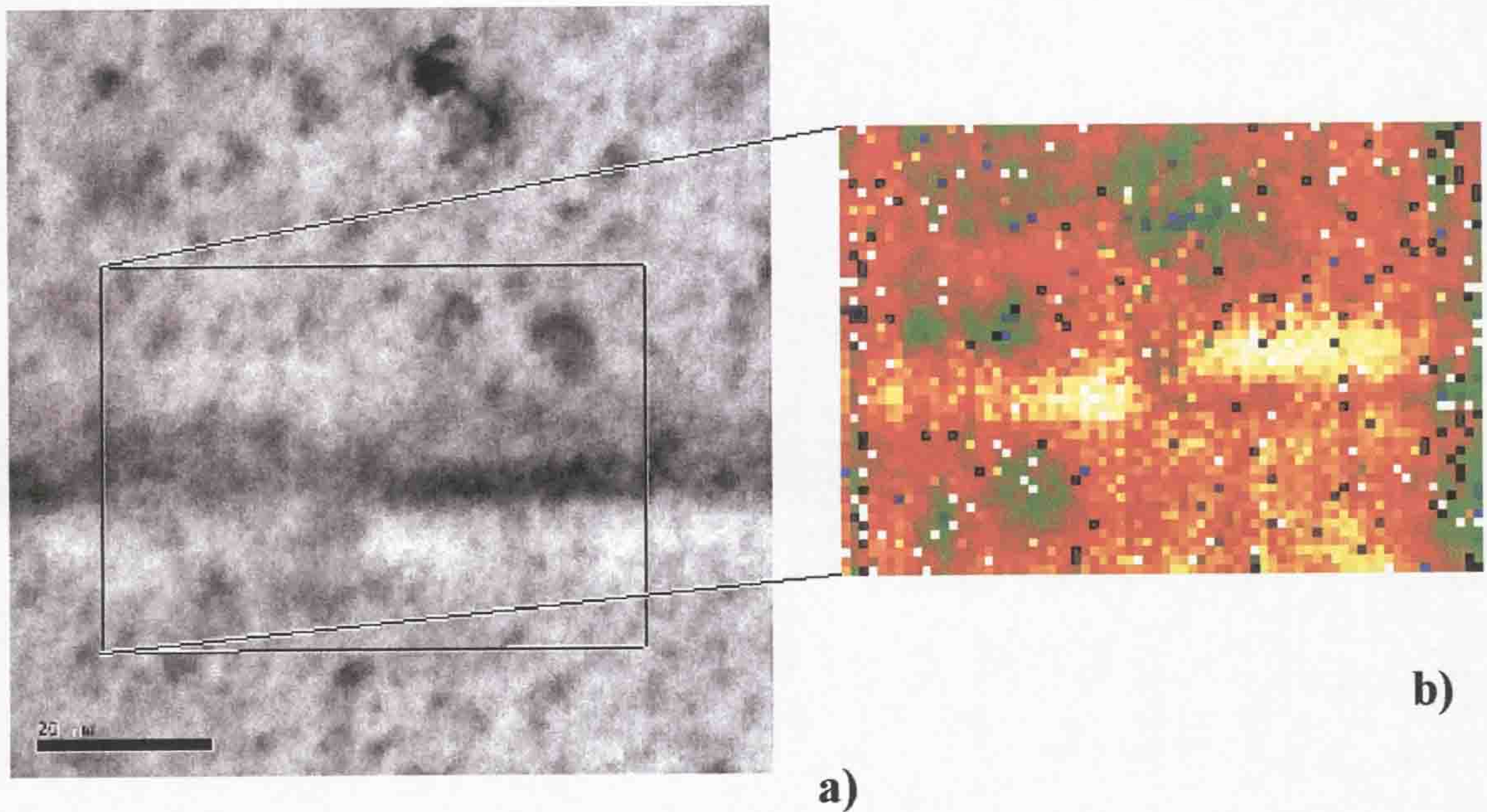

Figure 5-13 a) A bright field image of a GaInNAs QW flanked by GaAs, the EEL data was acquired from the boxed region and b) the map of the effective electron mass.

5.2.2 InAs QDs

The effective mass of InAs (and GaInAs) is lower than that of GaAs[25], thus using the EEL data obtained from the InAs QDs in a GaAs substrate, there should be a decrease in effective mass over the QDs. The effective mass was calculated using E_p, Figure 5-6b, and taking ε_∞ to be constant at 10.89. The resulting map is shown in Figure 5-14b. There is a reduction in m_e* which corresponds with the presence of each QD, giving average values for m_e* (GaAs)=0.078m_0 and m_e* (QD)= 0.074m_0,

hence a difference in effective mass, $\Delta m_e^* = 0.004$. By assuming that the InAs QD is approximately spherical i.e. the diameter of the QD seen in the bright field image (Figure 5-14a) of 15nm is the same in the direction normal to the image, and from thickness measurements of the specimen to be 79nm from the KK transformations, the composition of the sampled area that contains the QD is determined to be $Ga_{0.8}In_{0.2}As$ (also assuming that there is only one QD in the thickness). Using the relationship $m_e^*(Ga_xIn_{1-x}As) = 0.026+(0.041x)m_0$[25], m_e^* is calculated to be $0.0588m_0$ for $Ga_{0.8}In_{0.2}As$, this gives a shift from the accepted value of GaAs ($m_e^* = 0.064m_0$) of $\Delta m_e^* = 0.004$, in excellent agreement with the measured shift. For InAs, the value of ε_∞ is 12.3, higher than for GaAs (10.89), thus if it were possible to calculate a meaningful map of ε_∞, the expected value of m_e^* in the QDs would be slightly lower than that calculated from the map. By assuming a linear relationship between the InAs and GaAs values for ε_∞, and using the composition $Ga_{0.8}In_{0.2}As$, the revised ε_∞ (QD)= 11.17 and m_e^* (QD)=$0.072m_0$, giving a Δm_e^* of 0.006, remaining in good agreement with the calculated Δm_e^* for the same composition.

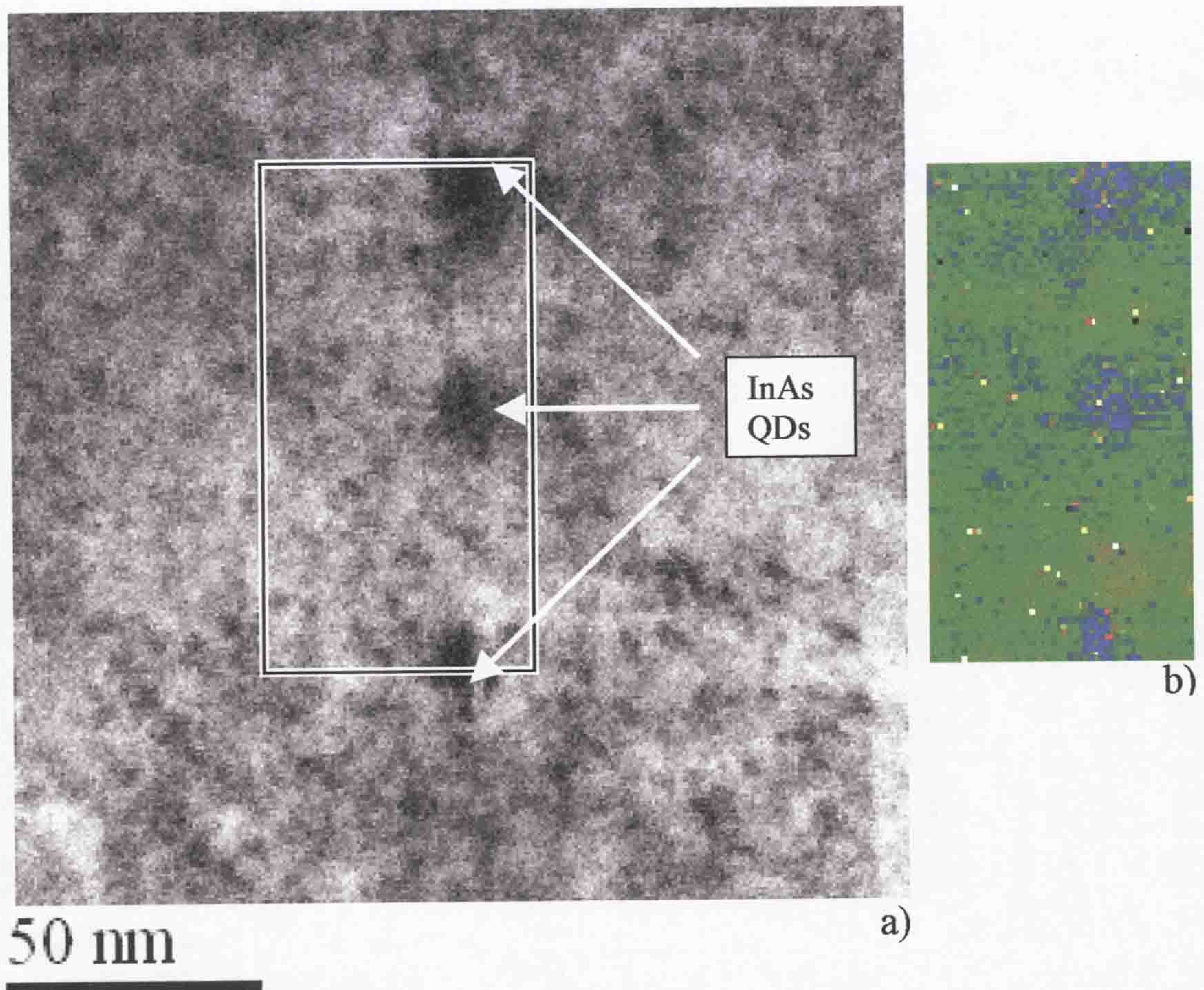

Figure 5-14. The bright field image of InAs QDs in a GaAs matrix is shown in a), the EELS data was acquired from the boxed region, and b) the map of the effective electron mass, where a slight decrease can be seen over the QDs.

5.2.3 GaN/AlGaN

To calculate m_e*, ε_∞ has been taken to be 5.35, the value for wurzite GaN. Figure 5-15 shows m_e* and although it is not very clear the averages of the two layers give effective masses of m_e*(GaN) = 0.183m_0 and m_e* AlGaN = 0.169m_0. The GaN results are again in reasonable agreement with accepted data, where m_e* (GaN) = 0.2m_0 from cyclotron resonance measurements[26], although recent measurements of m_e* have been as low as 0.18m_0[27]. There have not been many measurements of m_e* for AlGaN. *Jena et al*[28] determined an effective electron mass of m_e*=0.21m_0 for a

graded $Al_xGa_{1-x}N$ structure where x=0.11, following the general relationship between the parent binary compounds as AlN has an m_e* of $0.32m_0$, higher than GaN. The value of m_e* (AlGaN) obtained during this work is at variance with *Jena et al*, and the expected increase, this may be explained by the use of the constant value of ε_∞. The value of ε_∞(AlN) = 4.6[29], lower than that of GaN, by including ε_∞ as a variable, the value of m_e* (AlGaN) would increase. This is however, not possible with the current data as the signal-to-noise ratio is too high.

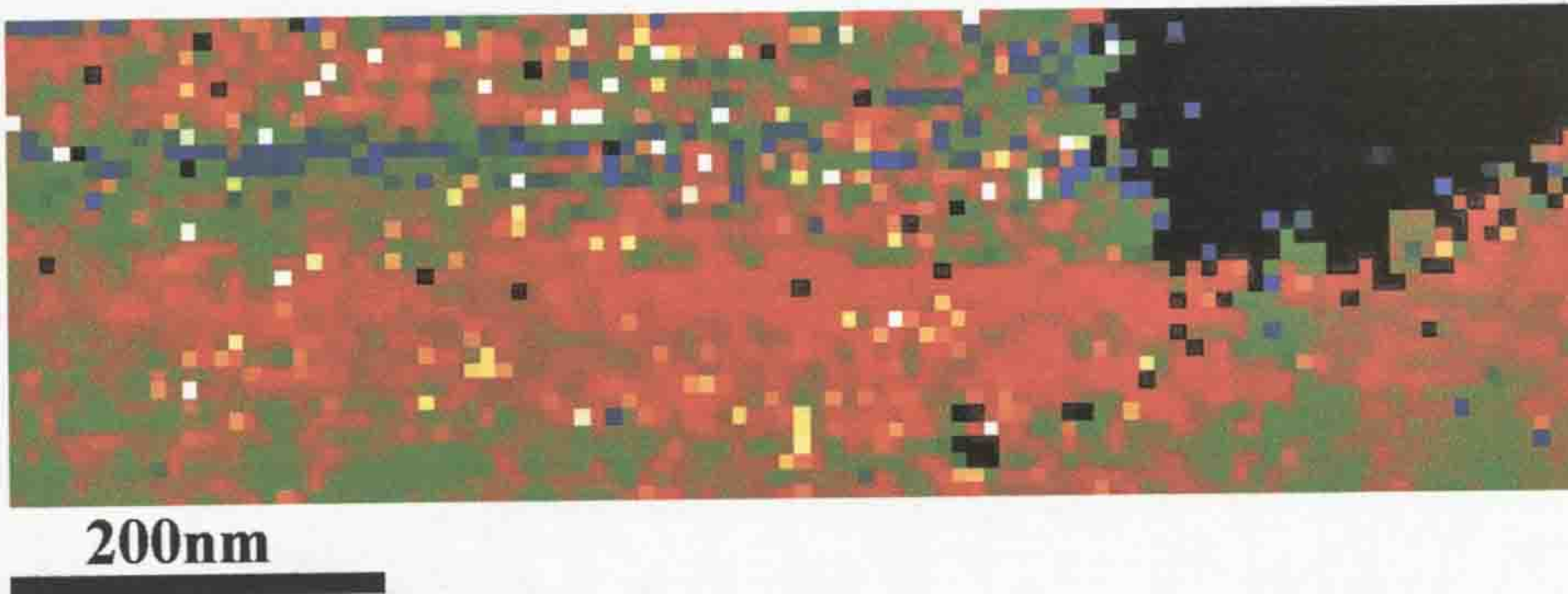

200nm

Figure 5-15. The effective mass map of GaN/AlGaN taken from the same data as the Ga 3d (Chapter 4) and Ep, Figure 5-7.

5.2.4 Modification of m_e*

The effective dielectric constant ε_{0eff} can be calculated as a function of energy by using the equation[10,30]

$$\varepsilon_{0,eff}(E) = 1 + \frac{2}{\pi}\int_0^{E_0} \frac{\varepsilon_2(E)}{E} dE \qquad 5.3$$

This has been written as a script (Appendix B4) that allows it to be applied to an ε_2 SI, producing a further SI for ε_{0eff}. An example of the spectrum is shown in Figure 5-16 where it can be seen that the onset of the effective dielectric constant is at the band-gap energy, and at higher energies $\varepsilon_{0,eff}$ becomes constant, this value is the high

frequency dielectric constant (ε_∞). It is thus possible to obtain a map of ε_∞ by taking the values of $\varepsilon_{0,eff}$ from a SI at a high energy (above 20eV).

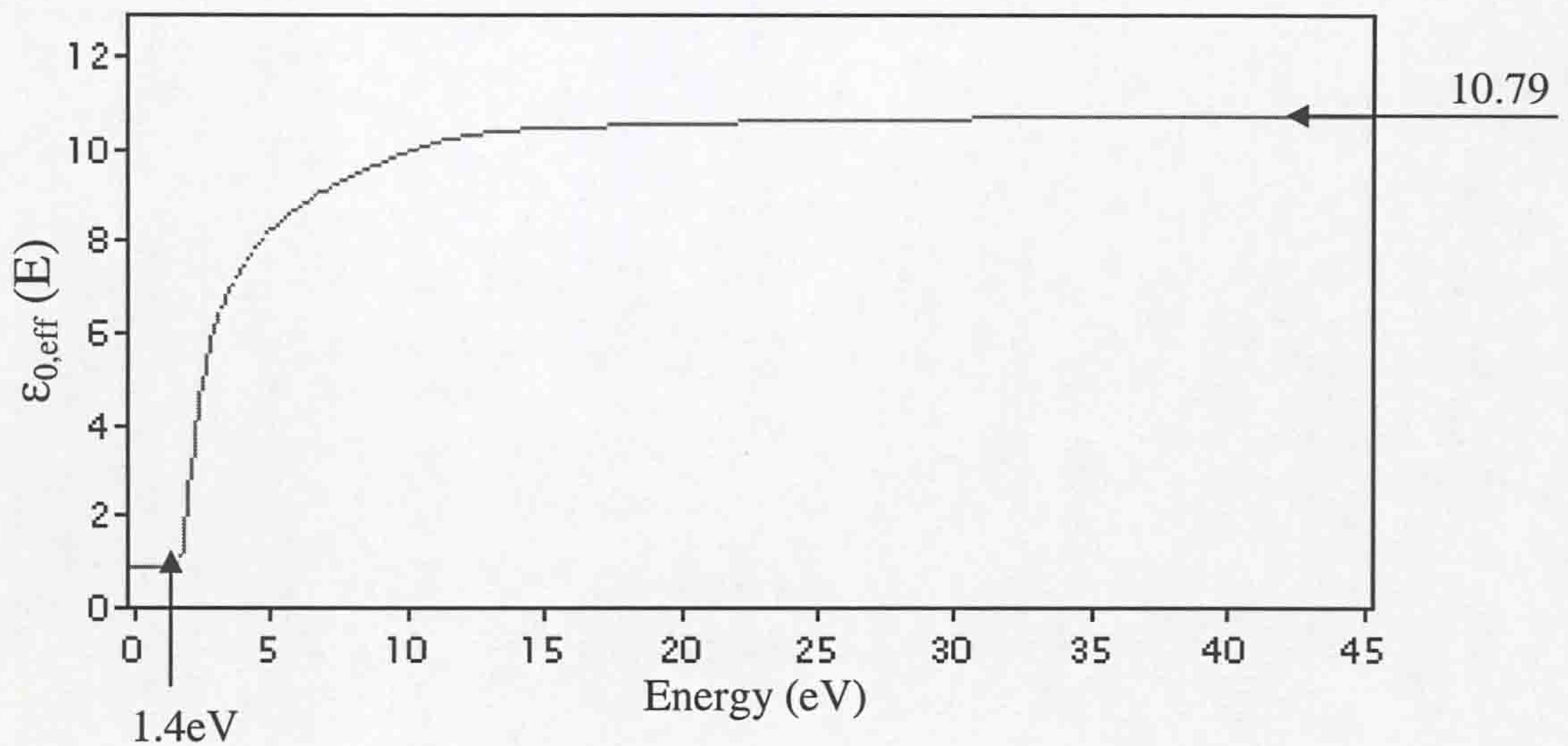

Figure 5-16 The dielectric constant relative to energy is shown above for GaAs. The curve can be seen to start at 1.4eV (the band-gap energy) and levels out after ~20eV, giving a high frequency dielectric constant of 10.79.

In Figure 5-17a a map of ε_∞ can be seen, this was obtained by taking the effective dielectric constant at 70eV for every pixel using a script detailed in Appendix B5. The average value for ε_∞ (GaAs) in the map is 8.80, this is lower than the accepted value of 10.89, there is also a large fluctuation of values, this is due to poor statistics in the acquired data, upon which errors have been added at each step; deconvolution to obtain SSD and further KK analysis. These problems are currently being investigated and are likely to be improved in the future. Withstanding the assumptions and errors, it is clear that there is a decrease in ε_∞ in parts of the QW. This is expected in N-rich regions as both InN and GaN have lower values of ε_∞ than GaAs and InAs. By using the map of ε_∞, the electron effective mass can be re-calculated, the script is in Appendix B6. The map of m_e* using the ε_∞ map can be

seen in Figure 5-17b. The errors have been carried over from the previous calculations; therefore the values are inaccurate. However, as a relative change it can be seen that m_e* increases within the QW, but the position of the higher m_e* has changed slightly from those shown in Figure 5-13. The new values of m_e* also correspond with the contrast of the bright field image in Figure 5-13. The change of position for the higher m_e* values indicates the importance of including ε_∞ in the calculations. However, as the fluctuations in ε_∞ are so significant with the current data, it is often impossible to obtain any information from the maps.

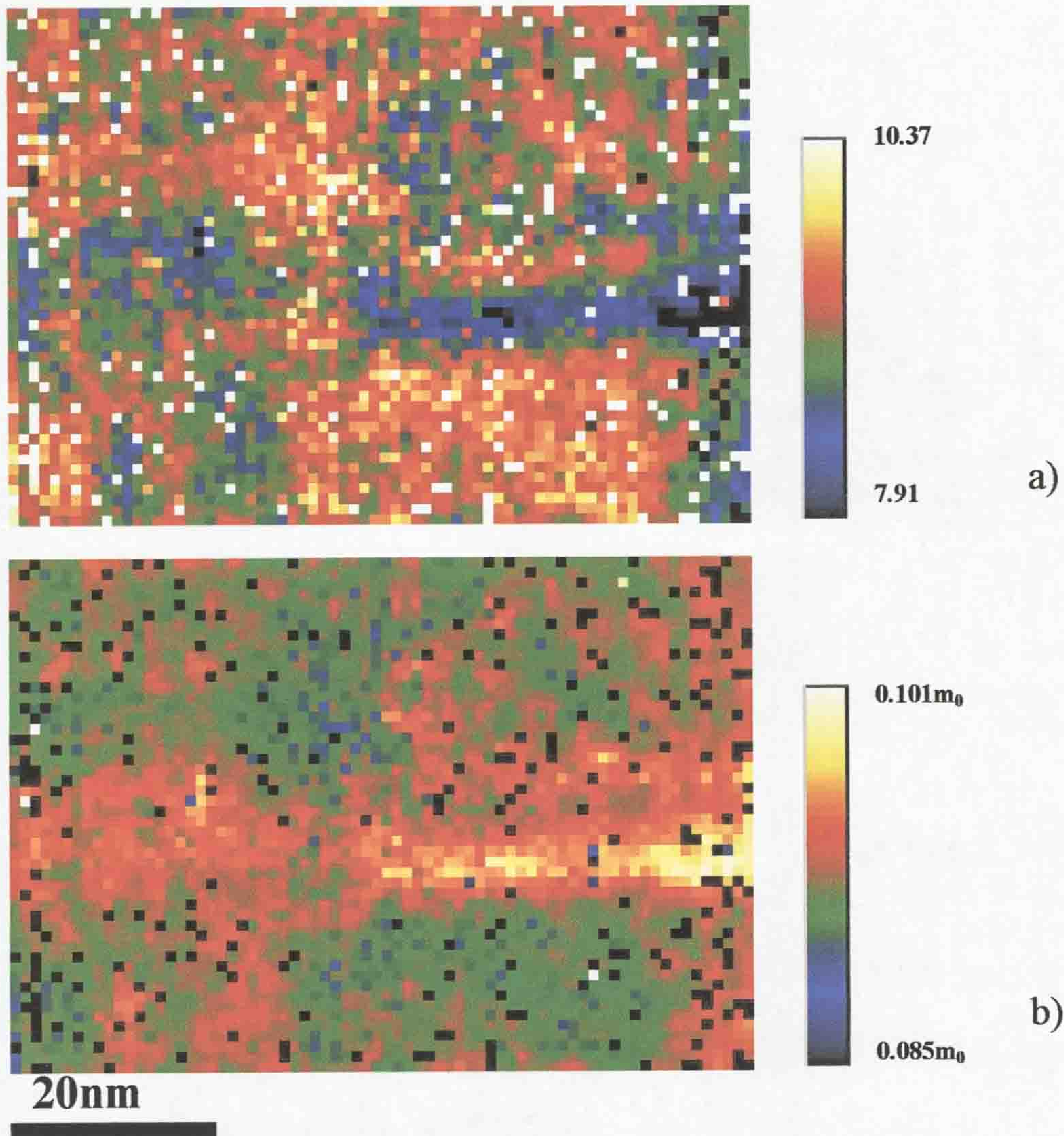

Figure 5-17. The high frequency dielectric constant (ε_∞) can be seen to decrease through the QW in a), and m_e* calculated with the varying ε_∞ is shown in b).

5.3 Discussion

It has been shown that by exploiting the improvements in energy resolution in combination with the mapping abilities in a STEM, high energy-resolution low-loss EEL spectrum images can be obtained at very high acquisition rates. Using the high energy resolution available, maps have been produced showing the change of plasmon energy through GaInNAs/GaAs QWs, GaInAs/GaAs QWs, InAs/GaAs QDs and AlGaN/GaN structures by measuring the centre point of the plasmon peak. With the standard deviation of a plasmon from bulk material calculated to be 7meV, detail has been seen in this study that has not previously been achieved. These values of plasmon energy have also been compared to the condition ε_1=0, the real part of the dielectric function calculated from the *Kramers-Kronig* relationship. As long as ε_2<<1, ε_1=0 represents the plasmon energy assuming that the plasmon has not suffered any damping. The difference between the centre of the plasmon peak and the condition ε_1=0 increases through QWs and QDs and is independent of the material, suggesting that the strain associated with the QWs and QDs increases the damping of the plasmon.

Through *Kramers-Kronig* analysis and the plasmon energy, the effective electron mass has been determined for a range of direct-gap semiconductors which, for the first time, can show the fluctuation of m_e* on a nanometre scale. The same method for calculating m_e* has previously been used with techniques such as infrared spectroscopic ellipsometry, micro-Raman scattering and synchrotron-excited ultraviolet photoemission spectroscopy. They have shown that m_e* can be

determined from the surface plasmon of TiN[31] and plasma-LO phonon modes of doped zinc-blende semiconductors[32] and hexagonal InN[33]. However, these techniques have all been for single point analysis of binary compounds and have not shown fluctuations of m_e* on a nanometre scale.

The results obtained in this study are in close agreement with values quoted in the literature for both GaAs and GaN and show that the introduction of N into GaAs increases m_e*. A further step has been taken by determining ε_∞ from the experimental data and adding it into the calculations for m_e*. The values for m_e* using the experimental values of ε_∞ at present contain a lot of noise. However, with further developments in hardware, for example, spectrometers, the fluctuations seen in the results presented in this study will decrease. The technique of determining m_e* will improve giving more accurate results, and could become a standard calculation for direct-gap semiconductors when analysed using EELS.

References

[1] R. Ludeke and L. Esaki, Surface Science, **47**, 132 (1975)

[2] P.N.H. Nakashima, T. Tsuzuki, and A.W.S. Johnson, J. Appl. Phys., **85**, 1556 (1999)

[3] V.J. Keast, A.J. Scott, M.J. Kappers, C.T. Foxon and C.J. Humphreys, Phys. Rev. B, **66**, 125319 (2002)

[4] G. Brocket and H. Lakner, Micron, **31**, 435 (1999)

[5] B. Daudin, J. L. Rouvierre, and M. Arley, Appl. Phys. Lett. **69**, 2480 (1996).

[6] A.M. Sánchez, M. Gass, A.J. Papworth and P.J. Goodhew, Microscopy and Microanalysis (2004)

[7] H. Raether, Excitation of Plasmons and Interband Transitions by Electrons, Springer Tracts in Modern Physics, 88, Springer-Verlag, Chapter 1 (1980)

[8] V. Fiorentini, M. Methfessel and M. Scheffler, Phys. Rev. B., **47**, 13353 (1993)

[9] K.A. Mkhoyan, J. Silcox, E.S. Alldredge, N.W. Ashcroft, H. Lu, W.J. Schaff, L.F. Eastman, Appl. Phys. Lett., **82**, 1407 (2003)

[10] D. Pines, Elementary Excitations in Solids, W. A. Benjamin, Inc. (1963)

[11] M.L. Cohen and J.R. Chelikowsky, Electronic Structure and Optical Properties of Semiconductors, Springer Series in Solid-State Sciences, **75** (1988)

[12] Z. Pan, L. H. Li, Y. W. Lin, B. Q. Sun, D. S. Jiang, and W. K. Ge, Appl. Phys. Lett. **78**, 2217 (2001).

[13] M. Hetterich, M. D. Dawson, A. Yu. Egorov, D. Bernklau, and H. Riechert, Appl. Phys. Lett. **76**, 1030 (2000).

[14] M. Levinstein, S. Rumyantsev and M. Shur, Handbook Series on Semiconductor Parameters vol. 2 World Scientific, London (1999)

[15] I. Vurgaftman, J. R. Meyer, and L. R. Ram-Mohan, J. Appl. Phys. **89**, 5815 (2001)

[16] S. Mazzucato, N. Balkan, A. Teke, A. Erol, R.J. Potter, M.C. Arikan, X. Marie, C. Fontaine, H. Carrere, E. Bedel and G. Lacoste, J. Appl. Phys., **93**, 2440 (2003)

[17] Z. Pan, L. H. Li, Y. W. Lin, B. Q. Sun, D. S. Jiang, and W. K. Ge, Appl. Phys. Lett. **78**, 2217 (2001)

[18] M. Hetterich, M. D. Dawson, A. Yu. Egorov, D. Bernklau, and H. Riechert, Appl. Phys. Lett. **76**, 1030 (2000).

[19] P. N. Hai, W. M. Chen, I. A. Buyanova, H. P. Xin, and C. W. Tu, Appl. Phys. Lett. **77**, 1843 (2000).

[20] Y. Zhang, A. Mascarenhas, H. P. Xin, and C. W. Tu, Phys. Rev. B **61**, 7479 (2000).

[21] S. Mazzucato and N. Balkan, A. Teke, A. Erol, R. J. Potter, M. C. Arikan, X. Marie, C. Fontaine, H. Carrère, E. Bedel, and G. Lacoste, J. Appl. Phys. **93** (5) 2440 (2003)

[22] C. Skierbiszewski, P. Perlin, P. Wisniewski, W. Knap, T. Suski, W. Walukiewicz, W. Shan, K. M. Yu, J. W. Ager, E. E. Haller, J. F. Geisz and J. M. Olson, Appl. Phys. Lett. **76**, 2409 (2000).

[23] A. Lindsay and E. P. O'Reilly, Solid State Commun. **122**, 443 (1999).

[24] D.L. Young, J.F. Geisz and T.J. Coutts, Appl. Phys. Lett. **82**, 1236 (2003)

[25] I. Vurgaftman, J. R. Meyer, and L. R. Ram-Mohan, J. Appl. Phys. **89**, 5815 (2001)

[26] M. Drechsler, D. M. Hoffman, B. K. Meyer, T. Detchprohm, H. Amano, and I. Akasaki, Jpn. J. Appl. Phys., Part 2, **34**, L1178 (1995)

[27] T. Wang, J. Bai, S. Sakai, Y. Ohno, and H. Ohno, Appl. Phys. Lett. **76**, 2737 (2000)

[28] D. Jena, S. Heikman, J.S. Speck, A. Gossard, U.K. Mishra, A. Link and O. Ambacher, Phys. Rev. B, **67**, 153306 (2003)

[29] Goldberg Yu. Properties of Advanced Semiconductor Materials GaN, AlN, InN, BN, SiC, SiGe . Eds. Levinshtein M.E., Rumyantsev S.L., Shur M.S., John Wiley & Sons, Inc., New York (2001)

[30] H.R. Philipp and H. Ehrenreich, Phys. Rev. **129**, 1550 (1963)

[31] C.G.H. Walker, J.A.D. Matthew, C.A. Anderson and N.M.B. Brown, Surface Science, **412**, 405 (1998)

[32] W.K. Metzger, M.W. Wanlass, L.M. Gedvilas, J.C. Verley, J.J. Carapella and R.K. Ahrenkiel, J. Appl. Phys., **92**, 3524 (2002)

[33] A. Kasic, M. Schubert, Y. Saito, Y. Nanishi and G. Wagner, Phys. Rev. B, **65**, 115206 (2002)

Chapter 6

Conclusions

Section		Page
6.1	Conclusions	144
6.2	Suggestions for future work	147

6. Conclusions

6.1 Conclusions

The main aim of this thesis was to investigate the elemental distribution in dilute nitride quantum wells using electron energy loss spectroscopy in a scanning transmission electron microscope. Understanding the distribution of elements and their effect on a material's properties on a nanometre scale can lead to a greater understanding of the overall performance of the structure, ultimately allowing better devices to be grown.

The combination of rapid acquisition times for low-loss EELS, high energy resolution and the spectrum imaging capabilities in the STEM led to the exploitation of the low-loss EELS technique during this research. The low-loss analysis has in the past often been overlooked, with the preference for core-loss EELS analysis. However, core-loss analysis requires long acquisition times, often leading to specimen damage or contamination. This hinders the advancement of high spatial resolution spectrum imaging, and in the future, discounting it as a technique for tomography.

It has been shown that transitions from semi-core states such as Ga $M_{4,5}$ and In $N_{4,5}$ to the conduction band occur in the low-loss region (<50eV) of EEL spectra. For materials such as GaAs based semiconductors, the Ga $M_{4,5}$ edge can be quantified. Further it has been shown that by applying the *Kramers-Kronig* transformations to the low-loss data, the same transitions (Ga 3d and In 4d) can be observed in ε_2, the

imaginary part of the dielectric function. As ε_2 can be related to absorption, the plasmon peak, which is apparent in the low-loss data, does not appear in ε_2. This allows for a better removal of the background signal, hence more accurate elemental information can be obtained. This process of determining the elemental distribution from ε_2 has been applied to spectrum images for several semiconductor systems in this study. The non-uniformity of In and Ga distribution within GaInNAs QWs has been shown, as has the distribution of In in InAs QDs and an AlGaN/GaN interface. This technique has also been used to show elemental distribution in InGaN MQWs[1], although the results are not presented in this thesis.

Quantifiable data for the Ga 3d edge has been obtained showing excellent agreement with compositions previously defined through either growth parameters or photoluminescence data. The data obtained from the In transition is in agreement with that from the Ga, i.e. where there is a reduction in Ga, there is an increase in In concentration. By using the same technique, N, which has a 2s edge at around 16eV can be seen in ε_2. The N L_2 edge is not usually visible in the low loss spectrum as it is very weak, and for GaAs based materials it occurs in the same region as the plasmon peak, thus is totally obscured. In this study it has been possible to produce maps of the N 2s transition over a GaInNAs QW, where the N concentration is nominally 1 at% of the group V elements. If the signal to noise ratio is not too low, maps of the As 3d edge which occurs at ~41eV can be produced showing the depletion of As in a GaInNAs QW. These maps have shown qualitatively the non-uniformity of group V elemental distribution within GaInNAs QWs.

The effect of composition on plasmon energy was investigated during this thesis, as was the difference between the two values of plasmon energy that can be determined; the plasmon peak centre and the condition $\varepsilon_1(E)=0$ (from the real part of the dielectric function). The difference between the two calculated energies appears to be in good agreement with the full width half maximum of the plasmon peak, which suggests that it could be a measure of strain. However, more work must be carried out in this area to confirm the relationship.

The final section of this thesis has taken low-loss EELS one step further, using it to calculate the effective electron mass in direct gap semiconductors and produce maps of nanometre scale resolution. This has been achieved by using an equation, which takes into account the high frequency dielectric constant (10.89 for GaAs). It allows the effective electron mass to be calculated from the plasmon energy and the number of electrons that are involved in the plasmon, calculated through the *Kramers-Kronig* analysis. This technique has produced results that are in good agreement with the accepted values, with the effective electron mass for GaAs calculated at ~$0.074m_0$, and verifies that the introduction of N into GaInAs increases m_e^* with respect to GaAs. It has also been shown that m_e^* for InAs QDs decreases with respect to GaAs and a value of $0.18m_0$ has been calculated for GaN (using ε_∞=5.35 the high frequency dielectric constant for GaN), in excellent agreement with the accepted value of $0.2m_0$. An improvement to this technique was introduced by using a variable ε_∞ rather than a constant for an entire map. ε_∞ was determined through the effective dielectric constant (an integration of ε_2) and added into the original calculation as another map of values. The results obtained from these improved calculations are slightly different to the previous calculations showing a shift in the

areas of increased m_e* for the quaternary material. However, due to the noise added with the extra step it is currently not possible to obtain these maps for all data and the values obtained are less accurate. Effective electron mass mapping in a STEM is a technique, which with the improvements in spectrometers, energy resolution and signal to noise ratio, could prove to be a valuable technique in the characterisation of direct gap semiconductor materials. This technique provides nanometre scale resolution maps detailing the change in m_e*, which can be directly compared to elemental distributions determined from the same data.

6.2 Suggestions for future work

The work carried out during this thesis has developed the technique of low-loss spectrum imaging in the STEM. However, there are several problems that arose, which obscured the quantification or processing of the data, the problems are

- Carbon contamination of the specimen
- Poor signal to noise ratio
- Possibility of the In 4d signal affecting the Ga 3d quantification
- Inadequate removal of the zero loss peak
- The possibility of interface plasmons

Apart from taking care during sample preparation, there is very little that can be done to reduce specimen carbon contamination, however, the signal to noise ratio could be improved if multiple spectra could be aligned and summed at every pixel in a spectrum image. This is an issue that has been brought to the attention of Gatan, who are currently working with the idea. With further work on the In 4d signal, the edge shape can be defined and removed from the ε_2 spectrum before quantification of the Ga 3d edge. The removal of the zero loss peak can be improved by obtaining

a better fit. An easy way to improve the fit is by using higher energy dispersion, so that more energy channels are involved in the peak. An energy dispersion of 0.05eV per channel (instead of 0.1eV per channel normally used during this study) allows a better zero loss peak removal. However, currently the data acquired at such an energy resolution is noisy with very low intensity. The aligning and summing of multiple spectra at every pixel would again reduce the noise observed in the spectra at 0.05eV per channel. Interface plasmons may occur at the boundary between two different materials; further work must be carried out on the study of interface plasmons to confirm whether they occur in semiconductor systems of similar materials.

A database of transitions occurring in the low-loss region could be compiled, which would be complimentary to the *EELS atlas* for core loss transitions. This would allow for more general work to be carried out in the low-loss region, allowing the mapping of specimens that are sensitive to the electron beam and cannot support long acquisition times. It would be interesting to obtain further understanding of the edge structure from the low-loss transitions. For example, Ga 3d has two apparent edges. These are related to transitions from the different spin-orbit splitting of the 3d electrons. Their separation and position changes with the composition of the material, for example, the edges for Ga 3d in GaAs appear close together and at a lower energy than for GaN, where the two edges are more separated and appear at a higher energy loss.

To determine the relationship of composition and strain on the plasmon peak for III-V semiconductors, a thorough study of the plasmon peak properties must be carried

out. The properties of a plasmon are affected by composition, strain and confinement. This study should start with well-characterised thin film binary and ternary materials, which are unstrained. The plasmon's energy and its amplitude and full width half maximum should be investigated to obtain a comprehensive understanding of plasmon behaviour. These results can then be compared with strained material or quantum wells of the same compositions.

A further area for future work is to reduce the noise in the *Kramers-Kronig* outputs to a level where more quantifiable data can be obtained for the effective electron mass when using the maps for the high frequency dielectric constant. The greatest improvements should be achieved by improving the signal to noise ratio and by obtaining a better zero loss peak removal as discussed previously, as these are the areas which are currently adding the greatest errors. If quantifiable data can be achieved which is in good agreement with the accepted values when the high frequency dielectric constant is a calculated value, this technique could prove to be extremely useful for increasing the understanding of direct gap semiconductor materials.

References

[1] AM Sánchez, M Gass, AJ Papworth, PJ Goodhew and P Ruterana, Phys. Rev. B, **70**, 035324 (2004)

Appendices

Section	**Page**
Appendix A	151
Appendix B	152

Appendix A

This table details the transitions from the semi-core states to different levels above the valence band. The first two columns show the transitions from the different spin orbits to conduction band minima L and X. The following four columns show the transitions from the different spin orbits to the top of the valence band and to vacuum level respectively. The final two columns show the transitions where the spin orbit splitting has not been resolved to the valence band and conduction band respectively.

		J=5/2		J=3/2		J=5/2	J=3/2	J=5/2	J=3/2	3d (Ga) 4d (In)	3d (Ga) 4d (In)
		L	X	L	X	Top of VB	Top of VB	Vacuum	Vacuum	Top of VB	CB Minimum
Cation	GaAs	20.23[1] 20.266[4]	20.44[1] 20.463[4]	20.71[1] 20.695[4]	20.92[1] 20.909[4]	18.7[3] 18.63[7]	19.1[3] 19.06[7]	24.2[3]	24.6[3]	18.82[5] 18.75[6]	20[2]
	GaN wurzite									17.74[9] 17.02 ± 0.09[10]	21.24[9]
	InAs	18.34[1]	18.63[1]	19.20[1]	19.50[1]	16.9[3]	17.72[3]	22.2[3]	23.02[3]	17.09[5] 17.36[6]	
	InN									15.5 ± 0.5[8] 15.74 ± 0.11[10]	16.3 ± 0.5[8]
										3d (As) 1s (N)	
Anion	GaAs					40.47[7]	41.18[7]			40.76[5]	
	GaN									395.25 ± 0.16[10]	
	InAs									40.30[5]	
	InN									395.35 ± 0.18[10]	

[1] D.E. Aspnes, M. Cardona, V. Saile, M. Skibowski and G. Sprüssel, Solid State Comm., 31, 99 (1979)
[2] M. Krawczyk, A. Jablonski, S. Tougaard, J. Toth, D. Varga, G. Gergely, Surface Science, 402-404, 491 (1998)
[3] N.J. Shevchik, J. Tejeda and M. Cardona, Phys. Rev. B., 9, 2627 (1974)
[4] O. Günther, C. Janowitz, G. Jungk, B. Jenichen, R. Hey, L. Däweritz and K. Ploog, Phys, Rev. B, 52, 2599 (1995)
[5] L. Ley, R.A. Pollak, F.R. McFeely, S.P. Kowalczyk and D.A. Shirley, Phys. Rev. B, 9, 600 (1974)
[6] K. Hirakawa, Y. Hashimoto, K. Harada and T. Ikoma, Phys. Rev. B, 44, 1734 (1991)
[7] E.A. Kraut, R.W. Grant, J.W. Waldrop and S.P. Kowalczyk, Phys. Rev. B, 28, 1965 (1983)
[8] K.A. Mkhoyan, J. Silcox, E.S. Alldredge, N.W. Ashcroft, H. Lu, W.J. Schaff and L.F. Eastman, App. Phys. Lett., 82, 1407 (2003)
[9] C.G. Olson and D.W. Lynch, Phys. Rev. B, 24, 4629 (1981)
[10] G. Martin, A. Botchkarev, A. Rockett and H. Morkoç, Appl. Phys. Lett., 68, 2541 (1996)

Appendix B

Digital Micrograph scripts were written for this study to allow further processing of the acquired data. Gatan has written some of the scripts on request.

1. Determine the point at which $\varepsilon_1(E)$ crosses zero

This script was written by Gatan on request. After taking a minimum energy value to start from e.g. 10eV (to avoid finding another point at which the spectrum crosses zero), the script finds the first point at which the spectrum crosses zero for every pixel in a spectrum image. The output is a map where each pixel has an energy value. It only calculates the value to the corresponding energy channel, i.e. its energy resolution is dependant on the energy dispersion chosen by the user.

```
image src:=getfrontimage()
// Establish which is dispersion dimension
number numdims = src.imagegetnumdimensions()
number n
for (n = numdims; n!= 0; n--)
        if (src.ImageGetDimensionSize(n)) break;
number dispDim = numdims == 3 ? 2 : 0;
// Establish cut-off point
number numChans = src.ImageGetDimensionSize(dispDim);
number scale = src.ImageGetDimensionScale(dispDim);
number origin = src.ImageGetDimensionOrigin(dispDim)
string units = src.ImageGetDimensionUnitString(dispdim)
number starteV
number min = origin;
number max = origin + scale*numChans
string prompt = "Enter low-cutoff in " + units + " (" + min + "-"+max+" "+units+")"
while(1)
{
        if (!GetNumber(prompt, origin, starteV)) throw(-128)
        if (starteV <= max && starteV>=min) break
        beep()
}
// Convert starteV to startchannel
number startCh = nearest(starteV-origin)/scale;
// Create destination image
image out
if (dispDim == 2)
```

```
        out:=realimage("Zero-cross point", 4, src.imagegetdimensionsize(0),
src.imagegetdimensionsize(1))
else
        out:=realimage("Zero-cross point", 4, src.imagegetdimensionsize(1))

// Now find first +ve channel after low-cutoff point.
Image temp = src.imageclone();
if (dispDim == 2)
{
        temp = (src > 0)/(iplane+1)
        temp = (iplane<startCh) ? 0 : temp;
        out[icol, irow] = temp > out[icol, irow] ? temp : out[icol, irow];
}
else
{
        temp = (src > 0)/(icol+1)
        temp = (icol<startCh) ? 0 : temp;
        out[icol, irow] = temp > out[icol, irow] ? temp : out[icol, irow];
}
out = 1/out*scale+origin;
out.imagesetintensityunitstring(units)
if (out.imagegetdimensionsize(0) == 1) OKdialog(sum(out)+units)
else showimage(out);
```

2. Remove all negative points from a map

Negative values in a map of plasmon energy can occur if the sampled area contains a hole. These negative values prevent further scripts from working. The script below finds any negative values in a map and allocates a nominal value of 1. The output is a map of values unchanged from the input except from removing the negative values.

```
//Declare Constants
String prompt = "select one input image gaussian fit map"
String title = "plasmon energy"
//Declare variables
Image img_gasfit_map
GetOneImageWithPrompt( prompt, title, img_gasfit_map);
Number width
Number height
GetSize ( img_gasfit_map, width, height)
//This should be a real image, not a complex image
Image img_CentreNoNegative_map := RealImage("centre no negative", 4, width,
height);
img_centreNoNegative_map = 0;
Number x, y
For ( y = 0; y < height; y++)
{
	for ( x = 0; x < width; x++)
	{
		// Get Ep value from EP map
		number Ep = GetPixel( img_gasfit_map, x, y );

		//take ep <0 to equal 1
		if (Ep < 0)
		(Ep = 1)

		SetPixel( img_CentreNoNegative_map, x, y, Ep );
	}
}
ShowImage(img_centreNoNegative_map)
```

3. Calculate the effective electron mass

This script was written by Gatan on request and has been modified. The inputs are a map of the plasmon energy (with no negative values) and the spectrum image of the effective number of electrons. At each pixel the script takes the plasmon energy and determines the intensity of the effective number of electrons at this energy value. This value is taken to be the number of electrons involved in the plasmon and is used with the plasmon energy and declared constants to calculate the effective electron mass.

```
//Declare Constants
String prompt = "select two input images gaussian fit map must be first"
String title = "Effective mass"
// Define constants
number h_bar = 1.05457267e-34
Number h_bar_sq = h_bar*h_bar
Number e0 = 8.854187817e-12
Number me = 9.1093897e-31
number e = 1.60217733e-19
number e1 = 10.89
number atoms_per_unit_vol = 1e27
//Declare variables
Image img_gasfit_map
Image img_kk_map
//display dialog
GetTwoImagesWithPrompt( prompt, title, img_gasfit_map, img_kk_map );
Number width
Number height
GetSize ( img_kk_map, width, height)
//This should be a real image, not a complex image
Image img_em_map := RealImage("em map", 4, width, height);
img_em_map = 0;
Number x, y
// There is an extra step required here.
// Want to read off the n value at the plasmon energy Ep
// First characterise the neff kk map; this should be a 3d dataset
if (img_kk_map.ImageGetNumDimensions() != 3)
	Throw("Neff map should be a 3Ds pectrum image for this routine to work!")
number escale = img_kk_map.ImageGetDimensionScale(2)
number eorigin = img_kk_map.ImageGetDimensionOrigin(2)
For ( y = 0; y < height; y++)
```

```
{
	for ( x = 0; x < width; x++)
	{
		// Get Ep value from EP map
		number Ep = GetPixel( img_gasfit_map, x, y );
		// Transform from calibrated units to pixels
		number Ep_ch = (Ep-eorigin)/escale
		// Read the corresponding neff value from the 3D map
		number neff = sum(img_kk_map[x, y, Ep_ch, x+1, y+1, Ep_ch+1])
		number ndens = atoms_per_unit_vol*neff
		// Check this equation is correct - I think it should be the following
equation
		//number m_eff = ((pixel_kk_map * h_bar) / ( sqrt(pixel_gasfit_map)
* epsilon)) / me;
		number meff = h_bar_sq*ndens/(Ep*Ep*e0*e1*me)

		SetPixel( img_em_map, x, y, meff );
	}
}
ShowImage(img_em_map)
```

Note: e1 is the high frequency dielectric constant and can be changed to suit the material.

4. Calculate the effective dielectric constant

This script was written by Gatan on request. The script integrates the spectrum image of epsilon 2 using equation 5.3 to calculate the effective dielectric constant. The output is a spectrum image of the effective dielectric constant.

```
// Run script with espilon 2 SI front-most.
// Works on 3D SIs only - needs modification to work on line-scans.
// Get front image and check it is OK
image eps2:=getfrontimage();
if (eps2.ImageGetNumDimensions() != 3)
        Throw("Operation halted: routine works on 3D datasets only");
// Create an energy array
number eDim = 2;
number nChans = eps2.ImageGetDimensionSize(eDim);
number origin = eps2.ImageGetDimensionOrigin(eDim);
number scale = eps2.ImageGetDimensionScale(eDim);
image energyLoss = RealImage("Energy loss", 4, nChans, 1);
energyLoss = icol*scale+origin;
// Perform the math
// Divide by energy
image temp1:=eps2.imageclone()
temp1 /= energyLoss[iplane, icol, irow];
// Remove information up to 0eV
number ch0eV = ceil(-origin/scale);
number xsize = eps2.ImageGetDimensionSize(0);
number ysize = eps2.ImageGetDimensionSize(1);
temp1[0, 0, 0, xsize, ysize, ch0eV + 1] = 0;
// Integrate over all energy
image integral := temp1.ImageClone();
integral.SetName("Integral");
integral = integral[icol, irow, iplane] + integral[icol, irow, iplane-1];
image effDC := integral.ImageClone();
effDC = 0;
effDC.SetName("Effective dielectric constant");
effDC = 1+2/pi()*integral*scale;
showimage(effDC);
```

5. Extract the high frequency dielectric constant from the effective dielectric constant

This script uses the spectrum image of the effective dielectric constant to determine the high frequency dielectric constant. At each pixel the intensity value of the effective dielectric constant is taken from a high energy region (after the plateau). The output is a map of values representing the high frequency dielectric constant.

```
//This script calculates the high frequency dielectric constant assuming
//70eV to be plateau, to change energy used, change number energy.
//Declare Constants
String prompt = "select one input image effective dielectric constant"
String title = "dielectric constant"
number energy = 70
//Declare variables
Image img_effd_map
GetOneImageWithPrompt( prompt, title, img_effd_map);
Number width
Number height
GetSize ( img_effd_map, width, height)
//This should be a real image, not a complex image
Image img_HFDC_map := RealImage("high frequency dielectric constant", 4,
width, height);
img_HFDC_map = 0;
Number x, y
number escale = img_effd_map.ImageGetDimensionScale(2)
number eorigin = img_effd_map.ImageGetDimensionOrigin(2)
For ( y = 0; y < height; y++)
{
	for ( x = 0; x < width; x++)
	{
		// Get energy value from effd map
		number energy_ch = (energy-eorigin)/escale
		// Read the corresponding effd value from the 3D map
		number HF = sum(img_effd_map[x, y, energy_ch, x+1, y+1,
energy_ch+1])
		SetPixel( img_HFDC_map, x, y, HF );
	}
}
ShowImage(img_HFDC_map)
```

6. Calculate the effective electron mass with high frequency dielectric constant map

This script is based on script 3 but has been modified to use a map for the high frequency dielectric constant rather than a constant. The output is a map which represents the effective electron mass.

```
//Declare Constants
String prompt = "select three input images gaussian fit map must be first"
String title = "Effective mass"
// Define constants
number h_bar = 1.05457267e-34
Number h_bar_sq = h_bar*h_bar
Number e0 = 8.854187817e-12
Number me = 9.1093897e-31
number e = 1.60217733e-19
number e1 = 10.89
number atoms_per_unit_vol = 1e27
//Declare variables
Image img_gasfit_map
Image img_neff_map
Image img_HFDC_map
//display dialog
GetThreeImagesWithPrompt( prompt, title, img_gasfit_map, img_neff_map,
img_HFDC_map );
Number width
Number height
GetSize ( img_neff_map, width, height)
//This should be a real image, not a complex image
Image img_em_map := RealImage("em map", 4, width, height);
img_em_map = 0;
Number x, y
// There is an extra step required here.
// Want to read off the n value at the plasmon energy Ep
// First characterise the neff kk map; this should be a 3d dataset
if (img_neff_map.ImageGetNumDimensions() != 3)
	Throw("Neff map should be a 3Ds pectrum image for this routine to work!")
number escale = img_neff_map.ImageGetDimensionScale(2)
number eorigin = img_neff_map.ImageGetDimensionOrigin(2)
For ( y = 0; y < height; y++)
{
	for ( x = 0; x < width; x++)
	{
		// Get Ep value from EP map
		number Ep = GetPixel( img_gasfit_map, x, y );
```

```
			// Transform from calibrated units to pixels
			number Ep_ch = (Ep-eorigin)/escale
			// Read the corresponding neff value from the 3D map
			number neff = sum(img_neff_map[x, y, Ep_ch, x+1, y+1, Ep_ch+1])
			number ndens = atoms_per_unit_vol*neff
			// Get HFDC value from HFDC map
			number HFDC = GetPixel( img_HFDC_map, x, y );
			// Check this equation is correct - I think it should be the following
equation
			//number m_eff = ((pixel_neff_map * h_bar) / (
sqrt(pixel_gasfit_map) * epsilon)) / me;
			number meff = h_bar_sq*ndens/(Ep*Ep*e0*HFDC*me)
			SetPixel( img_em_map, x, y, meff );
		}
}
ShowImage(img_em_map)
```